

MODULAR MULTILEVEL CONVERTERS FOR SOLAR PHOTOVOLTAIC - BATTERY
ENERGY STORAGE SYSTEM INTEGRATION

By

Farog Ismail Fadlelmoula Mohamed

Vahid R. Disfani
Assistant Professor of Engineering
(Chair)

Ahmed H. Eltom
Professor of Engineering
(Committee Member)

Abdelrahman A. Karrar
Associate Professor of Engineering
(Committee Member)

Abdul R. Ofoli
UC Foundation Associate Professor of
Engineering
(Committee Member)

MODULAR MULTILEVEL CONVERTERS FOR SOLAR PHOTOVOLTAIC - BATTERY
ENERGY STORAGE SYSTEM INTEGRATION

By

Farog Ismail Fadlelmoula Mohamed

A Thesis Submitted to the Faculty of the University of
Tennessee at Chattanooga in Partial
Fulfillment of the Requirements of the Degree
of Master of Science: Engineering

The University of Tennessee at Chattanooga
Chattanooga, Tennessee

August 2020

Copyright © 2020

By Farog Ismail Fadlemoula Mohamed

All Rights Reserved

ABSTRACT

PV systems have intermittency and partial shading challenges which endanger the stability and reliability of electric grids. Due to their scalable and modular structure, modular multi-level converters (MMC) are suitable for grid integration of PV and battery energy storage system (BESS). This thesis proposes a novel half-bridge submodule MMC (HBMMC) solution to connect distributed PV systems using distributed maximum power point tracking across the MMC submodules (SM) hence, addressing the partial shading challenge. To address PV power fluctuation due to intermittency, a novel solution to interconnect PV-BESS to the power grid through full-bridge submodule MMC (FBMMC) is proposed. In this solution, PV modules are distributed across the FBMMC SMs and a fully controllable large BESS is connected to the FBMMC DC-link to support the grid ancillary services. Full control over BESS is achieved by the full control over the MMC DC-link voltage as a result of the proposed MMC solution.

TABLE OF CONTENTS

ABSTRACT.....	iv
LIST OF TABLES	viii
LIST OF FIGURES	ix
CHAPTER	
1. INTRODUCTION	1
1.1 Background.....	1
1.2 Problem Statement.....	2
1.3 Objectives	3
1.4 Thesis Outline.....	5
2. LITERATURE REVIEW.....	6
2.1 Power Electronics Converters.....	6
2.2 Modular Multilevel Converters	7
2.3 MMC for Grid Integration of Solar Photovoltaic (PV)	8
2.4 MMC for Grid Integration of PV-BESS	9
3. MODULAR MULTILEVEL CONVERTER PRINCIPLES	12
3.1 MMC Structure.....	12
3.1.1 Half-bridge and Full-bridge submodules.....	13
3.1.2 MMC operating principles.....	15
3.2 MMC Modelling.....	18
3.2.1 MMC Circuit Analysis	18
3.2.2 MMC Discrete Model	21
3.3 MMC Control and Modulation.....	22
3.3.1 MMC Control Background.....	22
3.3.2 Model Predictive Control	23
3.3.2.1 MPC Multi-objective Optimization Problem	23

3.3.3	MPC switching algorithm.....	26
3.3.3.1	Submodule Sorting	26
3.3.3.2	Submodule selection.....	27
4.	HBMMC BASED DISTRIBUTED MAXIMUM POWER POINT TRACKING FOR PV SYSTEMS.....	29
4.1	Modular Multilevel Converters for Solar PV Integration.....	29
4.1.1	Grid-Connected PV System Configurations.....	29
4.1.1.1	Central Configuration	30
4.1.1.2	String Configuration	31
4.1.1.3	Multi-string Configuration.....	32
4.1.1.4	Micro-inverter configuration	33
4.1.1.5	Module Level power Electronics Configuration	34
4.1.2	Maximum Power Point Tracking.....	35
4.1.3	MMC Based Grid-Connected PV System Configurations	37
4.2	HBMMC based Distributed Maximum Power Point Tracking	38
4.2.1	Topology Design.....	38
4.2.2	Distributed MPPT Control Design	39
4.2.2.1	Distributed PV Modules	39
4.2.2.2	HBMMC AC output Current Control.....	40
4.3	Case Study	41
4.3.1	Simulation Setup.....	41
4.3.2	MMC Control Performance Under Partial Shading Condition	43
4.3.3	MMC Modulation Performance	44
4.4	Model Predictive Control Computation Requirements	47
4.4.1	MPC Computation Background	47
4.4.2	MPC Computation Expenses.....	48
5.	FBMMC FOR SOLAR PHOTOVOLTAIC-BATTERY ENERGY STORAGE SYSTEM INTEGRATION	50
5.1	MMC-Based PV-BESS systems	50
5.1.1	Background.....	50
5.1.2	Applications of BESS for Power Grid Support.....	51
5.1.3	Advantages of FBMMC over HBMMC for DER Integration.....	52
5.2	System Topology and Modulation Design.....	53
5.2.1	System Configuration	53
5.2.2	FBMMC Mathematical Model	54
5.2.3	FBMMC Modulation Design.....	57
5.2.3.1	Model Predictive Control (MPC) Based Modulation.....	57
5.2.3.2	SM Sorting.....	59
5.2.3.3	SM selection	59

5.2.4	Control Systems Design for PV-BESS Integration.....	60
5.2.4.1	MPPT for Distributed PV Modules	60
5.2.4.2	FBMM AC output Current Control	61
5.2.4.3	Circulating Current Control.....	61
5.2.4.4	BESS Control for Load Following and Frequency Control	65
5.2.4.5	BESS State of Charge Management	68
5.2.4.6	BESS current control	69
5.3	Case Study	69
5.3.1	Simulation Setup.....	69
5.3.2	Case 1: PV-BESS for Grid Demand Load Following Support.....	71
5.3.2.1	FBMMC Power Control	71
5.3.2.2	MMC Performance With Circulating Current Control.....	74
5.3.2.3	MMC Performance Without Circulating Current Control.....	76
5.3.2.4	BESS SOC Control.....	77
5.3.3	Case 2: PV-BESS for Load Following and Frequency support.....	79
5.3.3.1	FBMMC Power Control	80
5.3.3.2	MMC Performance With Circulating Current Control.....	83
6.	CONCLUSIONS AND FUTURE WORKS.....	87
6.1	Conclusions.....	87
6.2	Future Works.....	88
	REFERENCES	89
	APPENDIX	
A.	PV Module Characteristic.....	96
B.	BESS Model Characteristic	99
	VITA	102

LIST OF TABLES

3.1	HBSM different switching states	14
3.2	FBSM different switching states	15
4.1	Solar PV Array Data	42
4.2	HBMMC Parameters	43
5.1	Switching states of a FBSM.....	59
5.2	Different Cases of i_z^{ref} for all operating region	64
5.3	BESS Parameters	70
5.4	FBMMC Parameters	71
A.1	Solar PV module data and parameters	97
B.1	BESS model Parameters	100

LIST OF FIGURES

3.1	Structure of a half-bridge submodule	14
3.2	Structure of a full-bridge submodule	15
3.3	Modular multilevel converter schematic diagram	17
3.4	Modular multilevel converter circuit diagram	18
3.5	MMC switching control block diagram.....	28
4.1	Centralized PV configuration	31
4.2	String PV configuration	32
4.3	Multi-string PV configuration	33
4.4	Micro-inverter PV configuration	34
4.5	Module-level power electronics PV configuration.....	35
4.6	PV module IV characteristics curve	36
4.7	Flowchart of <i>P&O</i> MPPT algorithm.....	37
4.8	Topology of the proposed HBMMC-PV system	39
4.9	Half-bridge SM and PV module connection.....	40
4.10	HBMMC AC output current control.....	41
4.11	Phase A upper arm submodules irradiance and power. The figure is shown in double-axis format where irradiance and power are shown in different colors (red and blue) on the left and right axes, respectively	44

4.12	(a) Phase A upper and lower arms SMs voltage for the whole simulation time $3s$, (b) a zoom on phase A upper and lower arms SMs voltage for $0.1s$	45
4.13	(a) Phase A AC output current tracking for the whole simulation time $3s$, (b) a zoom on Phase A AC output current tracking for $0.1s$ showing the actual current i_a and the reference current i_b	46
4.14	(a) Phase A circulating current for the whole simulation time $3s$, (b) a zoom on Phase A circulating current for $0.1s$	47
4.15	MPC computation time Statistics in Computer 1	48
4.16	MPC computation time Statistics in Computer 2	49
5.1	Configuration and operating region of (a)(c) HBSM (b)(d) FBSM	53
5.2	The FBMMC-based PV-BESS configuration.....	54
5.3	Full-bridge SM and PV module connection	55
5.4	FBMMC AC output Current Control.....	61
5.5	Circulating current control.....	63
5.6	Upper arm v_{up} and lower arm v_{low} Operating region	63
5.7	MMC Power Control for power grid support	66
5.8	BESS Power Control for power grid support	67
5.9	BESS SOC Control Flowchart.....	68
5.10	BESS current control	69
5.11	(a) Grid power demand and the MMC output power to the grid and (b) the distributed PV system output power and the BESS power for grid demand following support	72
5.12	BESS Parameters when it is used for grid demand following support, (a) BESS state of charge (SOC), (b) BESS charging/discharging current and (c) the instantaneous voltage across the BESS	73

5.13	(a) Phase A upper and lower arms SMs voltage with i_z control and (b) a zoom on phase A upper and lower arms SMs voltage for 0.1s	74
5.14	(a) Phase A AC output current tracking for the whole simulation time 3s and (b) a zoom on Phase A AC output current tracking for 0.1s showing the actual current i_a and the reference current i_b	75
5.15	(a) Phase A circulating Current for the whole simulation time 3s and (b) a zoom on Phase A circulating Current for 0.1s	76
5.16	(a) Phase A upper and lower arms SMs voltage without i_z control and (b) a zoom on phase A upper and lower arms SMs voltage for 0.1s	77
5.17	BESS parameters when it is SOC reached 90%, (a) BESS state of charge (SOC), (b) BESS charging/discharging current and (c) the BESS charging/discharging power	78
5.18	BESS parameters when it is SOC reached 10%, (a) BESS state of charge (SOC), (b) BESS charging/discharging current and (c) the BESS charging/discharging power	79
5.19	Grid frequency under a 40% step-up load change and reference frequency	80
5.20	(a) Grid total power demand, grid power for demand following (case1) and the MMC output power to the grid and (b) the distributed PV system output power and the BESS power for grid demand following support.....	81
5.21	BESS power contribution to grid demand following and frequency control	82
5.22	BESS Parameters when it is used for grid demand following and frequency control support, (a) BESS state of charge (SOC) with and without frequency support and (b) BESS charging/discharging current with and without frequency support	83
5.23	(a) Phase A upper and lower arms SMs voltage for the whole simulation time 3s and (b) a zoom on phase A upper and lower arms SMs voltage for 0.1s	84
5.24	(a) Phase A AC output current tracking for the whole simulation time 3s and (b) a zoom on Phase A AC output current tracking for 0.1s showing the actual current i_a and the reference current i_b	85
5.25	(a) Phase A circulating current for the whole simulation time 3s and (b) a zoom on Phase A circulating Current for 0.1s	86

A.1 (a) The I-V characteristics of SunPower SPR-305E-WHT-D PV module and (b) The P-V characteristics of SunPower SPR-305E-WHT-D PV module 98

B.1 (a) Nominal current discharge Characteristic curve of Lithium-Ion BESS and (b) Current discharge curve at the rated voltage with different discharge current levels 101

CHAPTER 1

INTRODUCTION

1.1 Background

To meet the tremendous increase in energy demand and to reduce the dependence on fossil fuels for electricity generation due to its harmful environmental impacts, the global trend is to adopt a sustainable energy portfolio and increase the penetration of distributed energy resources (DER). In 2016, the electricity generated from renewable energy resources represents 15.6% of the total electricity generation in the United States [1]. In particular, solar photovoltaic (PV) energy experienced significant growth over the past decade, where 47% of the newly installed renewable power capacity globally in 2016 is coming from Solar PV energy [2]. Despite the great economic and environmental outcomes of this high increase in solar PV penetration, the adoption of PV energy has some prominent challenges, such as intermittency, uncertainty, performance losses due to partial shading which necessitate advanced power electronics solutions to capture maximum solar energy at any time. Moreover, their power output fluctuations may cause substantial voltage flicker, frequency issues, and power quality issues. All these concerns will eventually endanger the stability and reliability of the grid [3]. Among several solutions proposed in the literature to address intermittency challenges of PV systems, integrating battery energy storage system (BESS) with PV systems turns out to be the most effective approach [3]. BESS are coupled to PV systems to avoid the transient that could happen when PV systems have a fluctuated power output since it

can be used to level the PV output during cloud transients. There are numerous power electronic solutions to integrate both solar PV systems and BESS. However, most of these configurations lead to performance loss and require multiple power electronics level to integrate these systems.

PV and BESS control systems need to be coordinated very well hence a fully integrated power electronics solution to control both PV and BESS together is needed. One of these solutions is to utilize Modular multilevel converters (MMC). MMC is one of the recently-proposed configurations for grid connection of utility-scale PV systems [4–9]. Compared to other power electronic solutions for PV systems—including central and multi-string inverters—MMC has lower energy losses, and eliminates the need for a step-up transformer, thus reducing costs and improving the overall system efficiency [10]. These features have motivated researchers to develop new MMC configurations for DER integration and design efficient control systems and switching techniques.

1.2 Problem Statement

This thesis will address two major challenges of solar PV energy conversion systems, partial shading and intermittency. These problems are discussed as follows.

- i. Partial shading: one of the popular PV system integration topologies which has been practiced so far for utility-scale PV power systems is the centralized topology. In this topology, PV modules are connected in series and parallel to form an array of strings. The power from the array is fed to a single-string inverter controlled by an MPPT algorithm to capture the maximum solar energy available [11]. However, this topology leads to power losses due to the centralized MPPT topology, mismatch losses between solar PV modules and reliability issues due to lack of modularity. There are several proposed MMC-based Module-level power

electronics (MLPE) solutions as in [4–6] where each submodule (SM) is connected to one PV module. However, these solutions are very complicated for implementation, some of them lack circulating current control which is one of the main objectives in MMC control design, and others suffer from SM voltage balancing perspective. Therefore, there is a need for a new MMC topology and control design to address these issues.

- ii. Intermittency: the fluctuated power output of PV plants poses huge challenges to power grid stability and reliability. These power oscillations especially in utility-scale PV plants can lead to power quality degradation and cause power system transients that require significant variations in the gas turbines output to keep the load and generation the balance [12]. This could also lead to frequency regulation issues and voltage fluctuations challenges that may require more operation on transformers load tap changers [13, 14]. BESS integration to the PV system is one of the promising solutions to address this challenge. PV and BESS controls need to be coordinated efficiently, thus a fully integrated power electronics solution to control both PV and BESS together is needed. However, the research on the applications of PV-BESS integration based on MMC is very limited due to their design/control complexities and cost. Such integration necessities the need for new MMC topology, switching techniques, and control blocks to achieve this integration since these systems require a variable DC-link voltage.

1.3 Objectives

The major contributions of this thesis are two-folds:

- i. The first contribution of this thesis is to tackle the partial shading challenges and its effects on the PV systems power output. This thesis proposes a novel integrated power electronics

system which utilizes half-bridge MMC (HBMMC) to connect distributed PV systems using distributed maximum power point tracking (DMPPT) across the MMC SMs, given the benefits of DMPPT in solving the partial shading performance issues. An average SM capacitor voltage control algorithm is proposed in this thesis to ensure all the captured solar energy is transferred to the AC grid. The proposed solution is scalable from residential systems up to utility-scale systems, by adjusting power and voltage ratings of MMC components or by increasing the number of SMs on each arm. The model predictive control (MPC) strategy proposed in [15] is implemented to get the best switching sequences of SMs to control ac-side current, capacitor voltage, and circulating current simultaneously.

- ii. The second key contribution of the thesis is addressing PV systems intermittent nature. Where a novel full-bridge MMC (FBMMC) based solution is proposed to interconnect PV-BESS to the power grid. The proposed FBMMC topology utilizes the fact that full-bridge SM (FBSM) provides flexibility control over the DC-link and hence this topology is suitable for PV-BESS grid integration. In this topology, the PV arrays are interfaced with SMs through a DC-DC converter with an independent MPPT controller to extract the maximum power under partial shading conditions and provide independent voltage regulation for each SM capacitor. In the proposed topology, the BESS is connected to DC-link of the FBMMC without the need for any extra power electronics converter to control the BESS charging or discharging operation. This work also proposes an AC output Current Control design to ensure that all the PV and BESS powers are sent to the grid and no extra energy is stored in the FBMMC SM capacitors. Since the interconnected BESS has a fast response, a novel BESS power control design is

introduced to support the power grid by following the variable grid power demand-supply the mismatch between the grid demand load and the distributed PV system power output. Also, the proposed solution includes power grid frequency control to support the power grid in the event of frequency deviation by utilizing the BESS to emulate inertia and damping. The proposed solution improves power grid reliability and flexibility.

1.4 Thesis Outline

The Thesis is organized into six chapters as follows:

1. Chapter 2 provides an overview of the literature on MMC applications for PV and BESS grid connection.
2. Chapter 3 reviews the fundamental operation of MMC, MMC mathematical model, the main control design and its modulations techniques.
3. Chapter 4 proposes a novel MMC-Based distributed maximum power point tracking for photovoltaic (PV) systems.
4. Chapter 5 proposes a novel MMC solution for solar PV-battery energy storage system integration.
5. Finally, the conclusions and future work suggestions are reported in chapter 6.

CHAPTER 2

LITERATURE REVIEW

2.1 Power Electronics Converters

Power electronics converters are an integral part of today's world industries. With the recent research efforts on developing high efficiency switching devices, power electronics converters are getting more popular with a wide range of applications. They are used in the transportation industry on the motor drives of electric vehicles, trains and e-bikes, and in the power conversion system of electric vehicles charging stations [16–19]. In the power system industry, they are used in flexible AC transmission systems (FACTS) devices and high voltage direct current (HVDC) systems [20–22] as well as DER grid integration like solar PV systems [4, 5, 23], and battery energy storage systems integration [24, 25]. There are different types of power electronics converters but they can be categorized into two main types: current source converters (CSC) and voltage source converters (VSC). The latter is more popular in the applications of DER integration and is divided into two subcategories of two-level and multilevel converters. Two-level converters have prominent challenges in grid-connected PV systems applications, as they require large DC-link capacitors, have power quality issues, and need high switching frequency. They also have voltage sharing issues when they are connected in series to achieve high power ratings [26, 27]. Due to the limited power rating of this type of VSC, a large number of them are needed for large scale PV systems, which will make the aforementioned issues even worse.

2.2 Modular Multilevel Converters

To address these shortcomings of two-level VSC, power electronics researchers came up with the other subcategory of VSC which is the multilevel converters. Multilevel converters are built from a low or medium voltage switching devices to achieve higher voltage and power ratings, where multiple high level output voltage waveforms to mimics the AC sinusoidal waveform can be obtained. The main characteristics that make these types of converters stand out include less filter requirements, higher power quality output, increased efficiency, and the elimination of bulky connection transformers [28, 29]. The concept of multilevel converters dates back to the early 80's [30, 31]. There are different topologies and structures including the widely-known neutral point clamped pulsewidth modulation inverter [31] which was followed by the development of the flying capacitor [32, 33]. These topologies have seen a tremendous improvement which led to the introduction of active neutral point clamped (ANPC) multilevel converters [34]. These multilevel converter solutions had voltage scalability issues which were later solved by the development of cascaded converters like the cascaded h-bridge (CHB) converter [35].

One of the recently proposed multilevel converter topologies is modular multilevel converter (MMC), which was firstly introduced in [36]. The main features which make MMC outlined and very popular are its modularity and scalability, which reduce the cost of bulk components and allow for higher power ratings. Besides, MMC requires a lower switching frequency which translates to less switching losses and has higher efficiency and reliability [37, 38]. MMC has a wide range of applications in the medium and high-power applications, but the major application is in

the high-voltage direct current (HVDC) [22, 36, 39–41]. Recently, there have been extensive research works that employ MMC for integration DER to the AC system grid, such as photovoltaic systems [4–9, 23, 42–45].

2.3 MMC for Grid Integration of Solar Photovoltaic (PV)

Some researchers have investigated the connection of the PV system to the DC-link of the MMC as in [7–9]. An MMC solution is proposed to integrate series-connected PV arrays to the power grid, where the PV system is connected to the DC-link of MMC through a DC-DC converter. This solution does not address the partial shading problem, hence the system is not able to extract all the received solar PV power. An MMC based HVDC system is proposed in [42] where the PV system is connected to the MMC DC-link through a two-stage DC-DC converter. In [43], a single phase MMC solution connected to a DC-DC converter with MPPT control is proposed to interface the PV system, but the partial shading problems persist using this solution.

New MMC topologies for PV systems connection have been developed for large scale PV systems to solve the partial shading issues. An MMC-based module-level power electronics (MLPE) solution is proposed in [4, 23] where each submodule (SM) is connected to one or multiple PV modules. However, in [4] and [23], the control system and the switching algorithm were not efficient and lead to power quality issues and relatively high total harmonic distortion (THD) in the output voltage and current waveforms under partial shading conditions. The proposed solution in [5] uses an extra SM in each arm to compensate for other SM voltage fluctuation in that arm and achieve voltage balancing between phases but it increases the cost and the switching losses.

Moreover, it does not have a circulating current control while it is one of the primary objectives in the MMC control design.

To address the circulating current issue, [6] proposes a similar MMC-based MLPE solution with circulating current control. The solution, however, suffers from SM voltage balancing perspective. In PV interconnection to power grid where no energy storage systems are available, it is required that there should be no mismatch between the energy captured from PV modules and the energy transferred to the grid. Any power mismatch is stored in or provided by the MMC SM capacitors that can cause long-term deviation in SM capacitor voltages. Thus, it is physically impossible to capture maximum solar power and perform demand response at the same time unless energy stored in capacitors is compromised. [6] also fails to provide any SM capacitor voltage results to prove otherwise.

2.4 MMC for Grid Integration of PV-BESS

MMC is also used to couple BESS energy systems to the grid as reported in [24, 25, 46–50]. A simplified model of modular multilevel converters (MMC) and modular multilevel cascade converter(MMCC) for BESS integration applications are introduced and compared in [46]. In [24], three BESS integration topologies, MMCC, MMC with centralized BESS, and MMC with distributed BESS are reviewed and compared based on their efficiency, cost, module redundancy, and reliability. A simple modular integration topology for various BESS types within a grid-tie converter to provide additional system flexibilities is proposed in [47].

Applications of MMC in utility-scale PV systems and BESS are investigated in [25,48,49]. Also, a three-phase MMC-based BESS is proposed in [25]—where BESS is interfaced with half-bridge SMs of MMC through non-isolated DC-DC converters—and a real scaled 500 kW full-bridge MMCC is developed and investigated in [48]. However, both systems suffer from power losses and high cost due to the considerable number of semiconductor devices and have complicated BESS SOC control systems. An MMC-based BESS integration system which operates without a DC-link capacitor is introduced in [49], where battery cells are distributed in SMs. The paper is focused on MMC component design and selection of the manufacturers through cost comparison. In [50], a hybrid modular multilevel converter (HMMC) solution is proposed, in which the integrated BESS is based on a quasi-full bridge with integrated battery (QFBIB) SM that offers a DC fault ride-through capability. Different MMC-based solutions have been reported in the literature to interconnect PV-BESS to the power grid. In all these topologies, PV modules and battery cells are distributed and connected to SMs of MMC [51–54]. For instance, in the utility-scale PV-BESS integration studies, a single-stage power conversion re-configurable solar converter with Lithium-Ion battery structure is proposed in [51]. This solution uses fewer power electronics stages and a simple control strategy, leading to lower system cost, volume, and weight. [52] proposed a PV-BESS MMC system, where each arm consists of one BESS, and the rest of SMs are connected to PV modules, and the MMC utilizes the power exchange between its internal power flow control and the embedded BESS to develop power mismatch elimination strategy. An MMC-based multi-string PV system with integrated BESS is introduced in [53], which interfaces PV modules and BESS through a separate DC-DC converter connected to SMs. However, the solution increases the cost, volume, and weight of the system. To mitigate this issue, a hybrid PV-BESS conversion system is proposed in [54],

where each SM is interfaced to a PV module and BESS through a dual active bridge converter to allow bidirectional power flow, and its system performance is compared to the conventional two-level system without any focus on control system design. While MMC with full-bridge SMs—Also known as full-bridge MMC (FBMMC)—provides the required voltage flexibility on DC-link voltage to interconnect PV systems or BESS [55–58], all the aforementioned studies just utilized SMs to interconnect these resources and none have considered DC-link as a possible point of connection. This thesis employs this voltage flexibility to design MMC-based solutions to interconnect these DERs to the power grid.

CHAPTER 3

MODULAR MULTILEVEL CONVERTER PRINCIPLES

This chapter covers the fundamentals of modular multilevel converter (MMC) including both half-bridge submodules and full-bridge submodules. It also presents the MMC operating principle and the mathematical model of the MMC. It finally reviews model predictive control modulation as an advanced switching technique.

3.1 MMC Structure

Due to their salient characteristics, Modular multilevel converters are becoming one of the most recently studied types of voltage source converters (VSC) for medium and high voltage applications, the main features that made them outline are summarized below:

- i. MMC is modular as it offers a modular design based on identical converter cells [59].
- ii. It is scalable as any voltage level can be met by connecting the converter cells in series [59].
- iii. MMC is redundant because it can produce different output voltage levels with a different combination of switched converter cells, hence redundancy can be realized simply [59].
- iv. MMC features low switching power losses and high energy efficiency since it has much lower switching frequency compared to conventional converters [26].

- v. MMC has lower filtering requirements because of the multilevel output voltage waveform that has less total harmonic distortion (THD) content [60].
- vi. MMC offers fault tolerant operation, where converter cells can be isolated by having switching states that will isolate the cell during startups or fault conditions. also, in the case of a faulty cell, it can be bypassed with an appropriated control system, without stopping the load [29,61].
- vii. MMC eliminates the need for the bulky DC-link capacitor since the capacitor is distributed within the converter cells [37].
- viii. MMC eliminates the need for transformers since it can reach high voltage levels by scaling the system and connect more converter cells in series [62].

3.1.1 Half-bridge and Full-bridge submodules

MMC consists of small switching devices to obtain higher voltages with a smaller step size in the output voltage, which improves the output power quality and reduce filtering requirements. The basic structure of MMC consists of series connected submodules (SMs). The most popular types of SMs are half-bridge (HB) SM—also known as chopper cell—and full-bridge (FB) SM—also known as bridge cell—both are built from a set of semiconductor switches and a capacitor.

The structure of half-bridge submodule (HBSM) is shown in Figure 3.1. The two switches are switched inversely, when ($S_1= \text{ON}$ and $S_2= \text{OFF}$) the SM is switched ON and its voltage v_{SM} equals the capacitor voltage v_C . On the contrary, when ($S_1= \text{OFF}$ and $S_2= \text{ON}$), the capacitor is bypassed, SM is switched OFF and its voltage equals zero. HBSM different switching states are summarized in Table 3.1. The two switches can not be switched ON together at the same time as

it will cause a short circuit across the capacitor. HBSM is the most common topology of SMs, due to its structure simplicity, it requires simple control design and it has high efficiency.

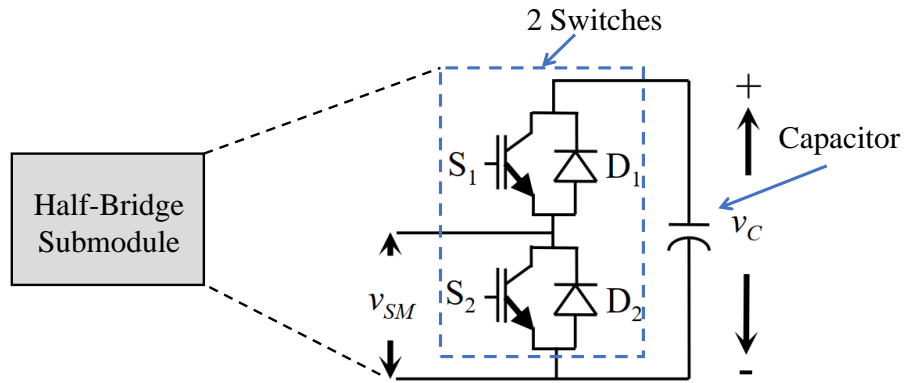


Figure 3.1 Structure of a half-bridge submodule

Table 3.1 HBSM different switching states

S_1	S_2	v_{SM}
ON	OFF	v_C
OFF	ON	0

Full-bridge submodule (FBSM) demands twice the number of switches for the same voltage rating in comparison to HBSMs, it consists of four switches (S_1 , S_2 , S_3 and S_4) and a capacitor as illustrated in Figure 3.2. FBSM can offer bipolar voltages: it is switched ON with a voltage equal to the voltage on the capacitor v_C when ($S_1= ON$, $S_2= OFF$, $S_3= OFF$ and $S_4= ON$) and is switched ON with a voltage equal to negative the capacitor voltage $-v_C$ when ($S_1= OFF$, $S_2= ON$, $S_3= ON$ and $S_4= OFF$). Also, FBSM is switched OFF or bypassed in two cases when ($S_1= ON$,

$S_2= \text{OFF}, S_3= \text{ON}$ and $S_4= \text{OFF}$) or ($S_1= \text{OFF}, S_2= \text{ON}, S_3= \text{OFF}$ and $S_4= \text{ON}$). These switching states are summarized in Table 3.2.

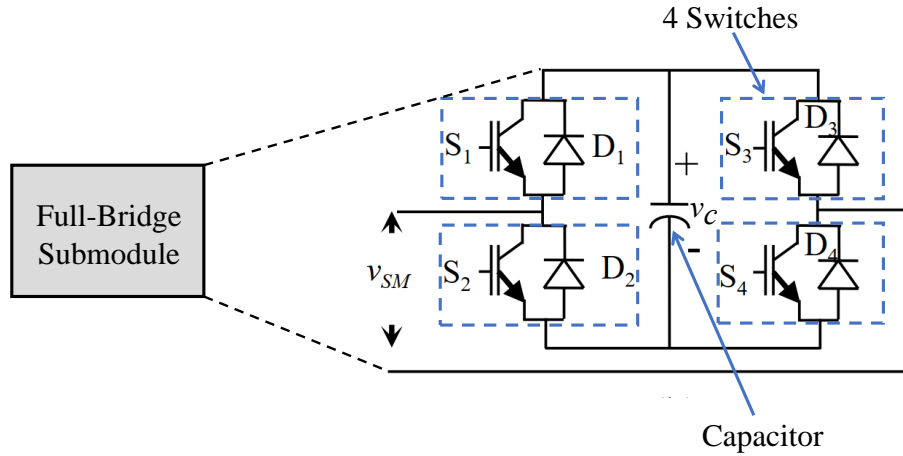


Figure 3.2 Structure of a full-bridge submodule

Table 3.2 FBSM different switching states

S_1	S_2	S_3	S_4	v_{SM}
ON	OFF	OFF	ON	v_C
OFF	ON	ON	OFF	$-v_C$
ON	OFF	ON	OFF	0
OFF	ON	OFF	ON	0

3.1.2 MMC operating principles

To obtain a staircase output voltage, SMs are connected in series. Figure 3.3 shows the schematic diagram of the MMC, which is modelled as a three-phase DC-AC converter connected to the power grid. In this structure, each converter's phase is called leg and every leg consists of

two arms; upper arm and a lower arm. As shown in the schematic, each arm made up of n SMs, and arm inductors all connected in series. The arm inductor is used to control the arm current, limit the circulating current, attenuate the high frequency components of the arm current, and limit fault current.

Figure 3.4 illustrates the circuit diagram of a half-bridge MMC—also known as HBMMC—it is based on HBSMs that act as a controllable voltage source. Each leg has $2n$ SMs, but to get the desired output voltage during normal operation only n switches in each leg are switched ON. The nominal voltage of each SM is equal to V_{dc}/n , where V_{dc} is the DC-link nominal voltage. The MMC can produce $n + 1$ level voltage at the AC grid side. Therefore, the power quality output of the MMC can be improved by increasing the number of SMs. The AC side grid is modelled by three sets of inductors (L), resistors (R), and a voltage source ($V_{s,j}$) connected in series, where j stands for the three phases (a,b and c).

Assuming that the arm inductors voltage drop is neglected in an ideal case, and applying KVL to each phase loops in the diagram between the DC-link and the AC side we get the following:

$$v_j = \frac{v_{dc}}{2} - v_{up} \quad j = a, b, c \quad (3.1)$$

$$v_j = -\frac{v_{dc}}{2} + v_{low} \quad j = a, b, c \quad (3.2)$$

By adding (3.1) and (3.2), the phase voltage can be written as:

$$v_j = \frac{v_{low} - v_{up}}{2} \quad j = a, b, c \quad (3.3)$$

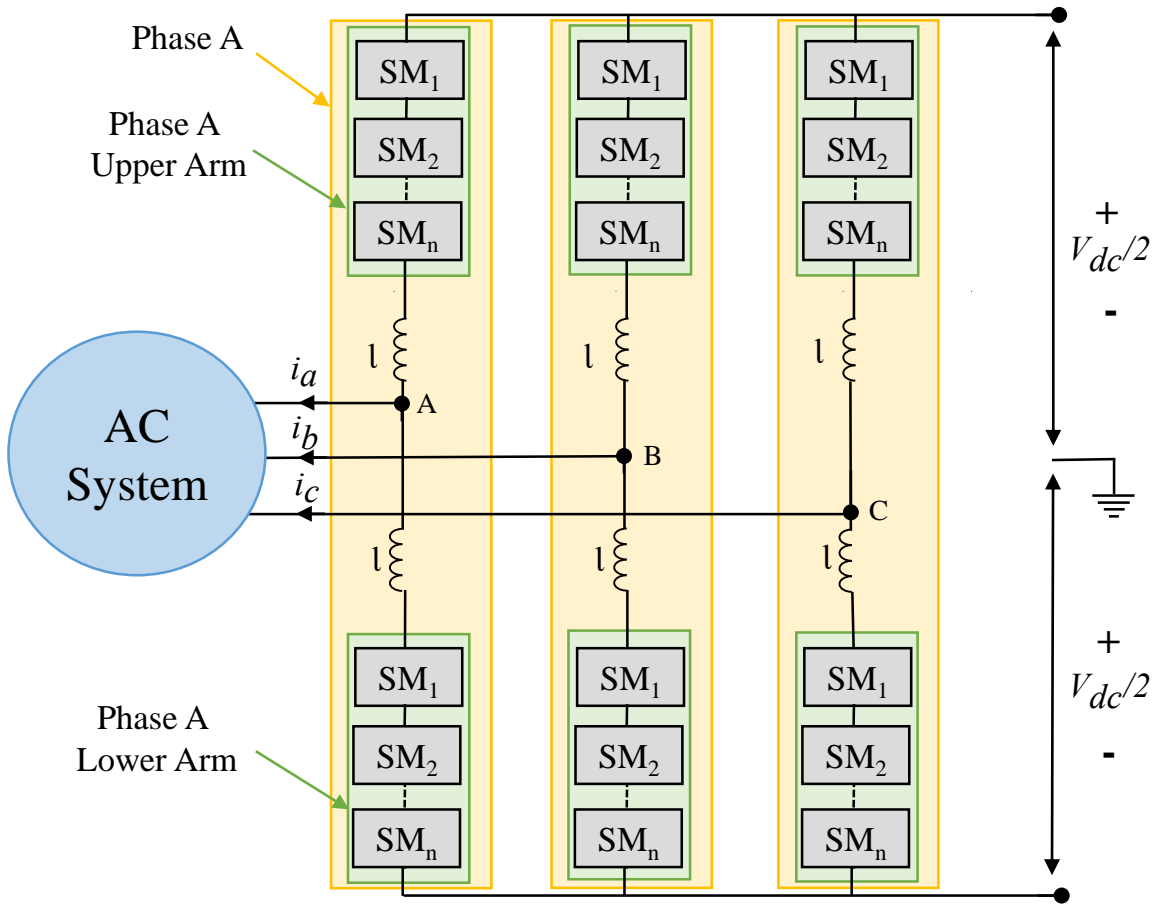


Figure 3.3 Modular multilevel converter schematic diagram

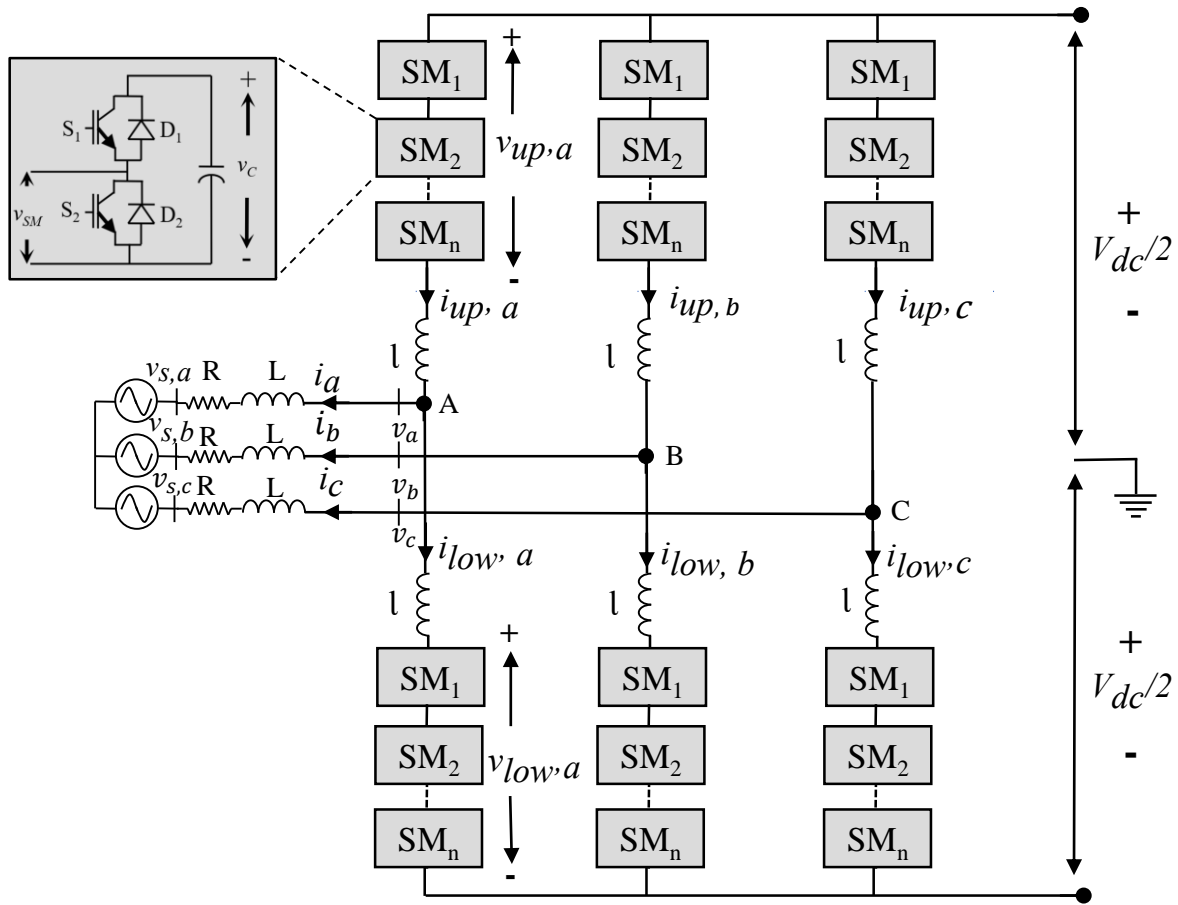


Figure 3.4 Modular multilevel converter circuit diagram

3.2 MMC Modelling

3.2.1 MMC Circuit Analysis

The MMC circuit analysis here is based on the circuit diagram in Figure 3.4. The AC current of each phase can be described by the corresponding upper-arm (i_{up}) and lower-arm (i_{low}) currents

as:

$$i_j = i_{up,j} - i_{low,j} \quad j = a, b, c \quad (3.4)$$

The three phases subscripts a, b and c are removed for simplicity. The total current in the upper arm and the lower arm consist of three components as expressed below:

$$i_{up} = \frac{i}{2} + \frac{i_{dc}}{3} + i_z \quad (3.5)$$

$$i_{low} = -\frac{i}{2} + \frac{i_{dc}}{3} + i_z \quad (3.6)$$

where the DC, the AC and the circulating currents are denoted by i_{dc} , i , and i_z respectively.

The circulating current i_z circulates between the converter legs and does not influence the AC side current, but it has negative effects on the SM capacitor voltage ripples, converter losses and hence the efficiency, and the rating of MMC components. Thus, the circulating current must be minimized or eliminated.

Based on equations (3.5) and (3.6), the circulating current flowing through each phase leg can be defined in terms of its corresponding upper arm, lower arm currents and Dc current as:

$$i_z = \frac{i_{up} + i_{low}}{2} - \frac{i_{dc}}{3} \quad (3.7)$$

Referring to Figure 3.3, the dynamic behavior of the each phase upper and lower arms can be described as follows:

$$v_{up} = \frac{V_{dc}}{2} - l \frac{di_{up}}{dt} - Ri - L \frac{di}{dt} - v_s \quad (3.8)$$

$$v_{low} = \frac{V_{dc}}{2} - l \frac{di_{low}}{dt} + Ri + L \frac{di}{dt} + v_s \quad (3.9)$$

where v_s is the grid voltage.

By adding equation (3.8) to (3.9) we get the following:

$$v_{low} + v_{up} = V_{dc} - 2l \frac{di_z}{dt} \quad (3.10)$$

while subtracting the two equations leads to:

$$v_{low} - v_{up} = l \frac{di}{dt} + 2Ri + 2L \frac{di}{dt} + 2v_s \quad (3.11)$$

The dynamic of submodule j capacitor voltage v_{Cj} is given by:

$$C \frac{dv_{Cj}}{dt} = i_{up} u_j \quad \forall j \in [1, n] \quad (3.12)$$

$$C \frac{dv_{Cj}}{dt} = i_{low} u_j \quad \forall j \in [n + 1, 2n] \quad (3.13)$$

where $u_j = 1$ if submodule j is active, and $u_j = 0$ otherwise.

3.2.2 MMC Discrete Model

The discrete model of MMC used in this thesis was proposed in [15], where Euler's approximation of the current derivative that represents the next step value for the AC-side current can be expressed as:

$$i(t + T_s) = \frac{1}{K'} \left(\frac{v_{low}(t+T_s) - v_{up}(t+T_s)}{2} - v_s(t + T_s) + \frac{L'}{T_s} i(t) \right) \quad (3.14)$$

where the time step T_s is small sampling time, $L' = L + l/2$ and $K' = R + L'/T_s$. The measured values at the current time are denoted by time indices (t) and the predicted values for the next time step are denoted by ($t + T_s$). The sampling frequency is assumed to be significantly higher compared to the grid frequency, the predicted value of grid voltage $v_s(t + T_s)$ can be replaced by its measured value $v_s(t)$. The predicted capacitor voltage of individual SMs on upper-level and lower-level arms are equal to:

$$v_{C_j}(t + T_s) = v_{C_j}(t) + \left(\frac{T_s i_{up}(t)}{C} \right) u_j(t + T_s) \quad \forall_{j \in [1, n]} \quad (3.15)$$

$$v_{C_j}(t + T_s) = v_{C_j}(t) + \left(\frac{T_s i_{low}(t)}{C} \right) u_j(t + T_s) \quad \forall_{j \in [n+1, 2n]} \quad (3.16)$$

Where $u_j(t + T_s)$ is the status of j -th SM.

Thus, the predicted voltages across upper-level and lower-level arms for the next step are defined as:

$$v_{up}(t + T_s) = \sum_{j=1}^n v_{C_j}(t + T_s)u_j(t + T_s) \quad (3.17)$$

$$v_{low}(t + T_s) = \sum_{j=n+1}^{2n} v_{C_j}(t + T_s)u_j(t + T_s) \quad (3.18)$$

and the expected circulating current is expressed as:

$$i_z(t + T_s) = \frac{T_s}{2l} (V_{dc} - v_{low}(t + T_s) - v_{up}(t + T_s)) + i_z(t) \quad (3.19)$$

3.3 MMC Control and Modulation

3.3.1 MMC Control Background

MMC successful control is very critical to achieve a high efficiency power conversion with high power quality output waveforms. There are multiple control objectives in the MMC control but the main goals are, controlling the SM capacitor voltage and regulate it, which is vital for a proper MMC operation, controlling the MMC arm currents to govern the MMC output voltage and current waveforms and finally eliminating the circulating current, which is coming from the instant voltage difference between each phase upper and lower arms.

The most common MMC control techniques are mostly based on linear controllers, whose control parameters are complicated to design and tune. Therefore, the control system response and performance could be affected if these parameters are not optimal. Moreover, the conventional modulation schemes such as pulse width modulation are utilized to determine the number of SMs

to be switched ON in each time step. Along with other control blocks are needed to achieve the MMC control objectives. However, these controllers mostly utilize a PI control which has a limited dynamic response based on their gains, the used switching frequency, and the type of PWM modulation scheme [63, 64]. Model predictive control (MPC) is suitable for multi-input-multi-output (MIMO) systems such as power electronics converter and it is one of the newly researched modulation techniques, which seems like a promising solution to overcome the overshoot issues of PI controllers, complex control structures and the PWM modulation shortcomings. MPC will be discussed in detail in the following section.

3.3.2 Model Predictive Control

Model predictive control (MPC) is a discrete model-based control scheme, which uses the model of the system along with an optimization model to obtain the predicted values of the control system variables [63]. MPC has salient features that make it stand out such as simplicity of control design, it can handle multiple objectives control requirements, and high dynamic performance. The MPC model here is based on the discrete-time model of MMC, its main control objectives are: to regulate the SM voltages, to control the output AC current, and to suppress the circulating current.

3.3.2.1 MPC Multi-objective Optimization Problem

To effectively control the MMC, the optimal switching sequence is obtained by using the model predictive control (MPC) strategy from [15, 58, 65], which seeks the following objectives:

- i. tracking the ac-side current (i) of all phases to their reference values (i_{ref}),
- ii. regulating all the submodules capacitor voltages to their nominal value (V_{DC}/n), and

iii. eliminating the circulating current (i_z) between the converter phase legs.

The MPC multi-objective optimization problem can be expressed as follows:

$$\begin{aligned}
& \min && \left| v_{C_j}(t + T_s) - \frac{V_{dc}}{n} \right| \\
& \min && |i_{ref} - i(t + T_s)| \\
& \min && |i_z(t + T_s)| \\
& \text{over:} && \{u_1, u_2, \dots, u_n\} \\
& \text{subject to:} && (3.14) - (3.19) \\
& && \sum_{j=1}^{2n} u_j(t + T_s) = n \tag{3.20}
\end{aligned}$$

Assuming that the ideal value of corresponding variable for the next time step is denoted by $(\cdot)^*(t + T_s)$, the ideal values implying exact AC current tracking can be represented by:

$$i^*(t + T_s) = i_{ref} \tag{3.21}$$

which is can be rewritten based on (3.14) as the following expression:

$$i^*(t + T_s) = i_{ref} = \frac{1}{K'} \left(\frac{v_{low}^*(t + T_s) - v_{up}^*(t + T_s)}{2} - v_s(t + T_s) + \frac{L'}{T_s} i(t) \right) \tag{3.22}$$

From (3.22), the relation between v_{up}^* and v_{low}^* can be expressed as:

$$v_{low}^*(t + T_s) - v_{up}^*(t + T_s) = 2K' i_{ref}(t + T_s) + 2v_s(t) - \frac{2L'}{T_s} i(t) \tag{3.23}$$

If the predicted circulating current is set to the ideal value zero $i_z^*(t + T_s) = 0$, then from (3.19) when the variables are replaced by their ideal values, we get the following:

$$i_z^*(t + T_s) = 0 = \frac{T_s}{2l} (V_{dc} - v_{low}^*(t + T_s) - v_{up}^*(t + T_s)) + i_z(t) \quad (3.24)$$

$$v_{low}^*(t + T_s) + v_{up}^*(t + T_s) = V_{dc} + \frac{2l}{T_s} i_z(t) \quad (3.25)$$

The anticipated values of upper and lower level voltages of MMC are calculated as:

$$v_{up}^*(t + T_s) = \left(\frac{V_{dc}}{2} + \frac{l}{T_s} i_z(t) \right) - \left(K' i_{ref} + v_s(t) - \frac{L'}{T_s} i(t) \right) \quad (3.26)$$

$$v_{low}^*(t + T_s) = \left(\frac{V_{dc}}{2} + \frac{l}{T_s} i_z(t) \right) + \left(K' i_{ref} + v_s(t) - \frac{L'}{T_s} i(t) \right) \quad (3.27)$$

Let $\Delta i = i - i_{ref}(t + T_s)$, $\Delta v_{low} = v_{low}^* - v_{low}$, and $\Delta v_{up} = v_{up}^* - v_{up}$ donates the deviation of the corresponding variables from their ideal values. The deviation of the AC current and the circulating current from their ideal values are derived as:

$$\Delta i = \frac{1}{2K'} (\Delta v_{low}(t + T_s) - \Delta v_{up}(t + T_s)) \quad (3.28)$$

$$i_z(t + T_s) = \frac{T_s}{2l} (\Delta v_{low}(t + T_s) + \Delta v_{up}(t + T_s)) \quad (3.29)$$

Applying a weighted sum method to the optimization problem, the AC current tracking and circulating current mitigation objectives with weights w and w_z respectively. The following

multi-objective optimization problem describes the switching algorithm:

$$\min_U \sum_{j=1}^{2n} \left| v_{C_j}(t + T_s) - \frac{V_{dc}}{n} \right| \quad (3.30)$$

$$\min_U f = \left\{ \begin{array}{l} \frac{w}{2K'} |\Delta v_{low}(t + T_s) - \Delta v_{up}(t + T_s)| + \\ \frac{w_z T_s}{2l} |\Delta v_{low}(t + T_s) + \Delta v_{up}(t + T_s)| \end{array} \right\} \quad (3.31)$$

subject to: (3.14) – (3.19)

$$U = [u_1, u_2, \dots, u_{2n}] : u_j \in \{0, 1\} \quad \forall_{j \in [1, 2n]} \quad (3.32)$$

Where the first objective (3.30) regulates SM capacitor voltages and the second objective (3.31) follows the reference values of AC current and circulating currents.

3.3.3 MPC switching algorithm

Based on [15], the optimization problem is solved in two separate steps; submodule sorting first and then submodule selection.

3.3.3.1 Submodule Sorting

In this step, the SM capacitor voltage regulation objective function (3.30) is solved by sorting SMs effectively where the highest priority is given to the SMs contributing the most in voltage balancing. It starts by sorting the upper and lower arms SMs based on their expected capacitor voltages. Based on (3.15) the upper arm SMs voltages increase or decrease based on the direction of i_{up} . For instance, if $i_{up} > 0$, the capacitor of a switched ON SM will be charged, hence the algorithm

will select the SM with least capacitor voltages. Hence, the SMs are sorted based on their capacitor voltages in the descending order if $i_{up} < 0$ or in the ascending order if $i_{up} \geq 0$. After sorting, the algorithm define the SMs voltages on the upper arm after sorting as $V_{C_{up}}^{sort} = [V_{C_1}^{sort}, \dots, V_{C_n}^{sort}]$ and the SMs voltages on the lower arm after sorting as $V_{C_{low}}^{sort} = [V_{C_{n+1}}^{sort}, \dots, V_{C_{2n}}^{sort}]$.

3.3.3.2 Submodule selection

After the SMs are sorted based according to their capacitor voltages in the previous step, this step first calculates the cumulative sum vectors of the components of $V_{C_{up}}^{sort}$ and $V_{C_{low}}^{sort}$ to get $V_{C_{up}}^{sum}$ and $V_{C_{low}}^{sum}$ as defined as below.

$$V_{C_{up}}^{sum} = \{\alpha_k : k = 0, 1, \dots, n\} \quad (3.33)$$

$$V_{C_{low}}^{sum} = \{\beta_k : k = 0, 1, \dots, n\} \quad (3.34)$$

where

$$\alpha_0 = \beta_0 = 0$$

$$\alpha_k = \sum_{i=1}^k V_{C_i}^{sort} \quad \forall_{k \in [1, n]}$$

$$\beta_k = \sum_{i=n+1}^{n+k} V_{C_i}^{sort} \quad \forall_{k \in [1, n]}$$

To minimize the objective function (3.31), the required combination of (α, β) is defines by th switching algorithm. In [15], it is proven that the optimal solution is a member of the set $\{(\alpha_i, \beta_j), (\alpha_{i+1}, \beta_j), (\alpha_i, \beta_{j+1}), (\alpha_{i+1}, \beta_{j+1})\}$ if $v_{up}^* \in [\alpha_i, \alpha_{i+1})$ and $v_{low}^* \in [\beta_j, \beta_{j+1})$. That is, to

select the best combination of SMs to switch on, it is sufficient to check the objective function for these 4 points only instead of for n^2 solutions and select the solution outputting the minimum objective function.

The whole MMC switching control based on MPC can be summarized in a block diagram similar to the one in [40] as depicted in Figure 3.5 below.

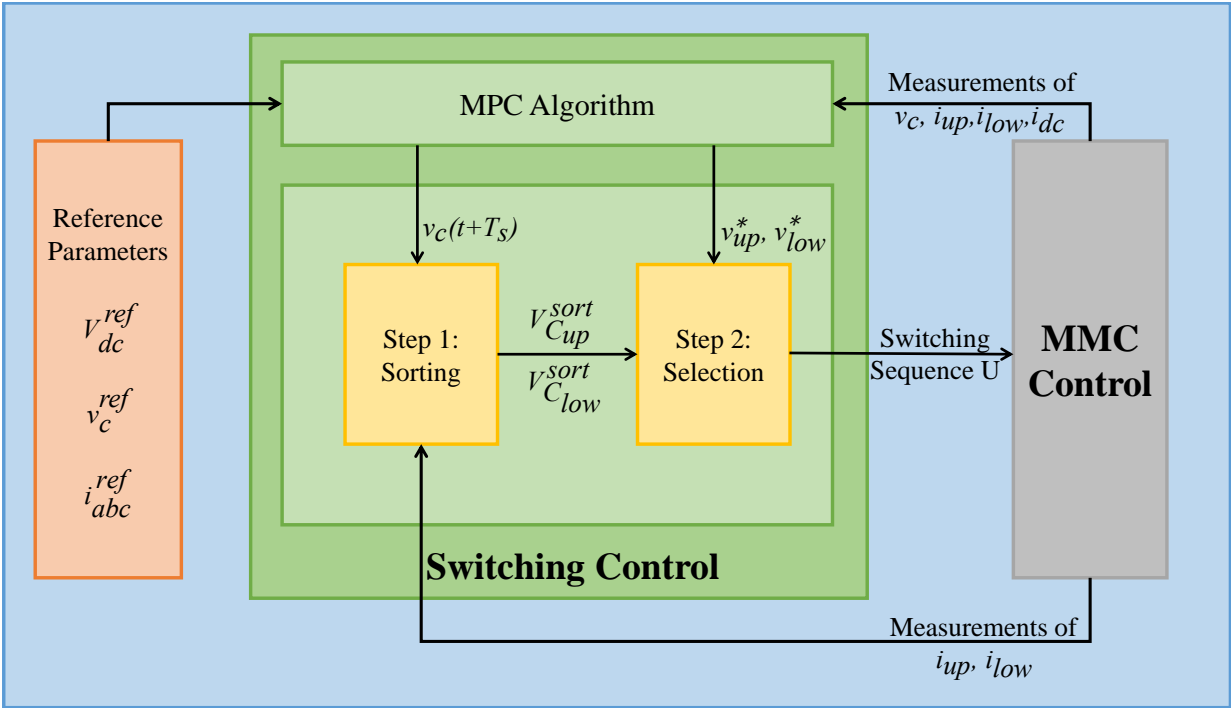


Figure 3.5 MMC switching control block diagram

CHAPTER 4

HBMMC BASED DISTRIBUTED MAXIMUM POWER POINT TRACKING FOR PV SYSTEMS

This chapter covers different grid-connected PV system configurations and then it reviews MMC-based PV system topologies. In this work, a HFMMC based PV system is proposed to improve the system performance under partial shading conditions. Then, the proposed topology is tested for a 7-level HBMMC under different irradiance conditions to validate the effectiveness of the developed control system. Finally, it reviews the computational expenses of the utilized model predictive control and presents its computation requirements in several computers with different processor properties.

4.1 Modular Multilevel Converters for Solar PV Integration

4.1.1 Grid-Connected PV System Configurations

Most of grid-connected PV systems configurations utilize the conventional two-level voltage source converters (VSC) for both residential-scale and utility-scale PV systems. However, they

This chapter has been accepted to IEEE PESGM as a conference paper and is to appear on IEEE Xplore, a pre-print version of the accepted paper is published on <https://arxiv.org/> in Feb 2020 [66, 67].

can be classified into five groups, centralized PV configuration, string PV configuration, multi-string PV configuration, micro-inverter PV configuration and module-level power electronics configuration.

4.1.1.1 Central Configuration

This configuration is the most practiced topology so far. As shown in Figure 4.1, PV modules are connected in series and parallel to form an array of strings. The power from the array is fed to single central DC-AC inverter, and subjected to maximum power point tracking (MPPT) control, which is then inverted and injected to the power grid [11]. This configuration features simplicity and low cost. However, it has several performance issues since all the PV array rely only on one MPPT possible voltage, in the events of partial shading it has low conversion efficiency due to power mismatch losses. Moreover, its based on conventional VSC which has power quality issues and lack of scalability.

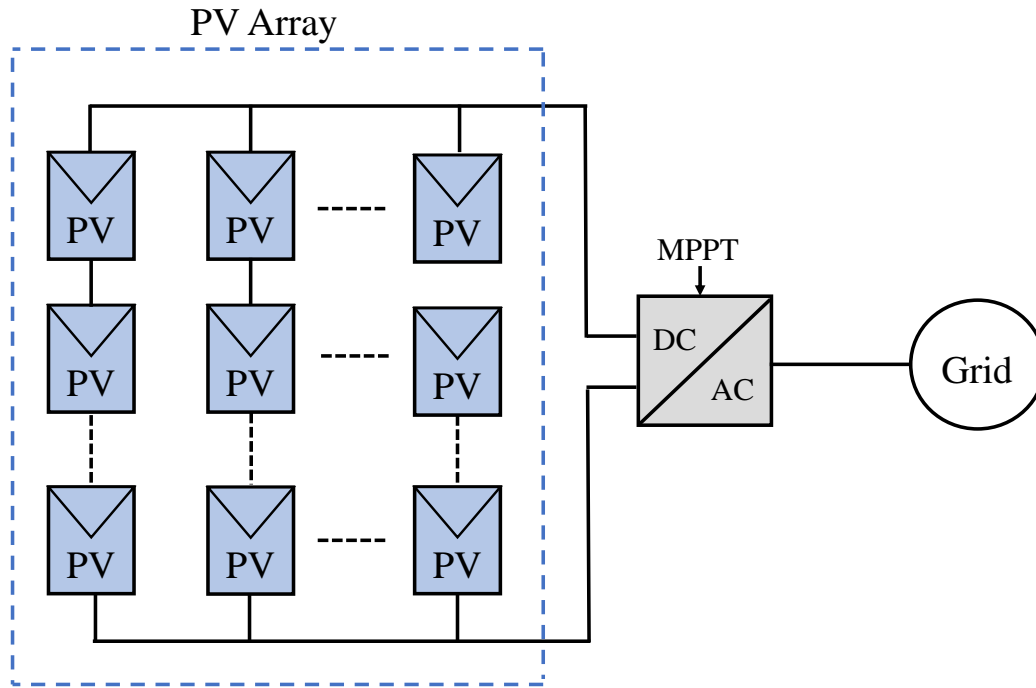


Figure 4.1 Centralized PV configuration

4.1.1.2 String Configuration

In this configuration each PV string is interfaced to the power grid through a separate assigned DC-AC inverter as illustrate in Figure 4.2. Even though this configuration has a better power conversion performance compared to the centralized configuration still, it has power quality issues and needs a transformer for grid integration [68].

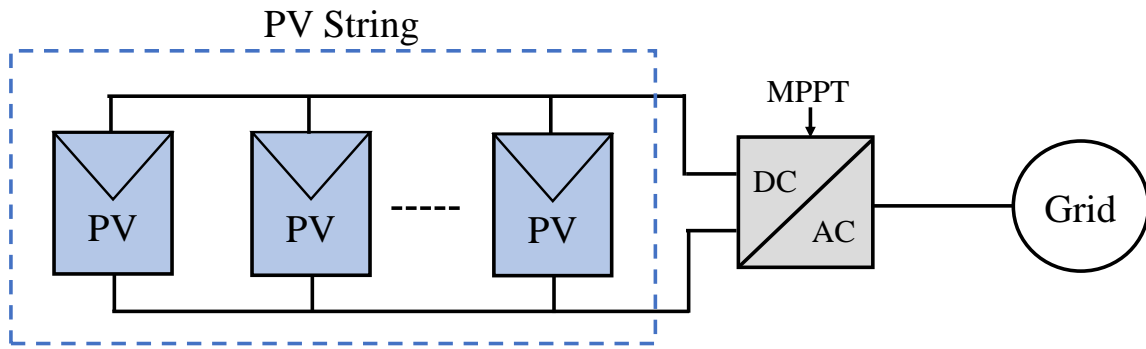


Figure 4.2 String PV configuration

4.1.1.3 Multi-string Configuration

As depicted in Figure 4.3, in this topology each PV string is connected to a dedicated DC-DC converter that has an MPPT algorithm to improve the system performance. Then the total DC power is injected to the power grid through a central DC-AC inverter. This configuration has improved performance, however, the MPPT is not fully distributed and the power mismatch issues persist.

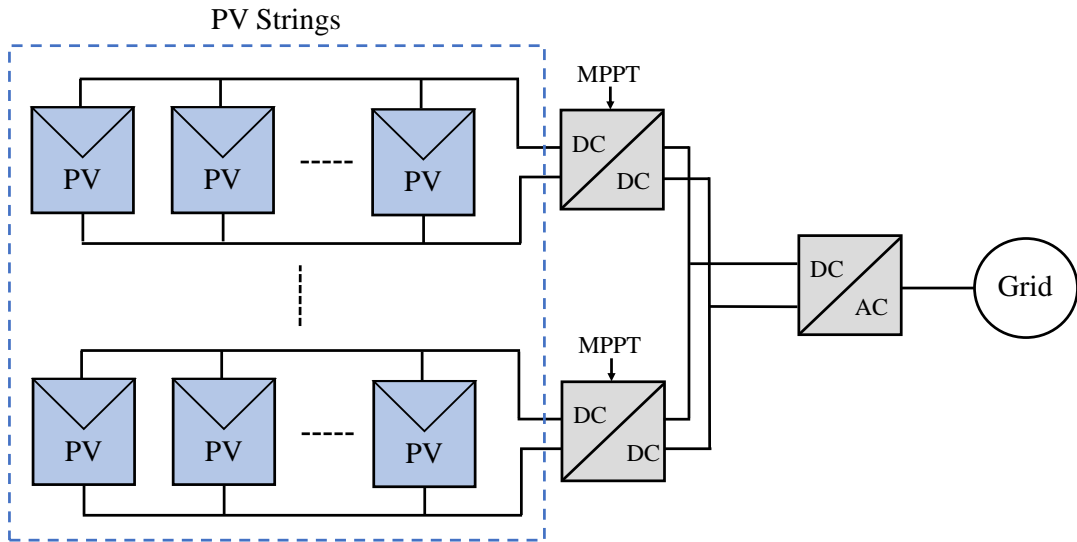


Figure 4.3 Multi-string PV configuration

4.1.1.4 Micro-inverter configuration

Figure 4.4, where each PV module is connected to the power grid through a dedicated DC/AC converter with MPPT control, hence an independent MPPT can be achieved [68]. Each PV module output is effectively in parallel, which eliminates the module mismatch power losses. But the high cost of this system prevent its widespread adoption.

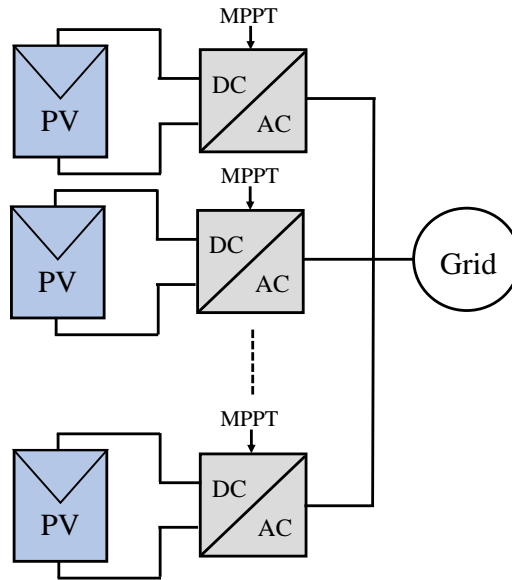


Figure 4.4 Micro-inverter PV configuration

4.1.1.5 Module Level power Electronics Configuration

This topology was developed to overcome the shortcomings of other PV grid-connected configurations. As shown in Figure 4.5, it decouples the maximum power point of the individual modules from the overall MPP of the system by introducing DC-DC converters in each PV module before inverting, hence it allows for fully independent MPPT.

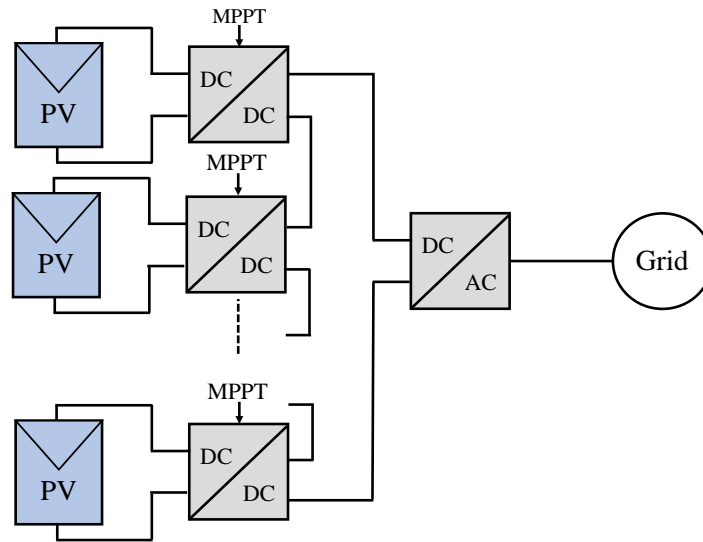


Figure 4.5 Module-level power electronics PV configuration

4.1.2 Maximum Power Point Tracking

PV system generated power varies with the surrounding environmental conditions such as irradiation, temperature and shading conditions. All these factors affect the fluctuations in the open-circuit voltage and the short circuit current. Moreover, the PV module model has nonlinear characteristics as shown in Figure 4.6, thus a maximum power point tracking (MPPT) control is needed to control the voltage to the point where the maximum available power can be extracted. [69].

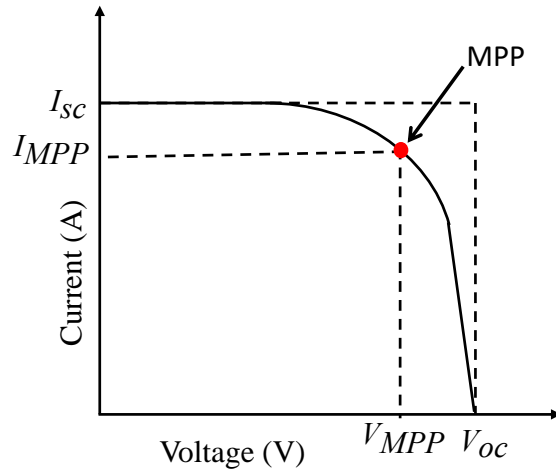


Figure 4.6 PV module IV characteristics curve

Different MPPT algorithms have been developed and reviewed as in [70] such as constant voltage (*CV*), perturb and observe (*P&O*), current sweep, and incremental conductance (*IC*). However, perturb and observe (*P&O*) is one of the most common algorithms due to its simplicity and good performance.

The *P&O* algorithm takes the measurement of both PV voltage V and current I to calculate the power P_1 . Then it applies a small perturbation on the voltage in one direction and calculates the corresponding power P_2 . It compares the calculated power with the old power, if it is higher that means the perturbation is in the correct direction; otherwise the direction should be reversed. Following this way, the maximum power point voltage is located and hence the maximum power can be extracted [71]. A generic flowchart of *P&O* MPPT algorithm is shown in Figure 4.7 below.

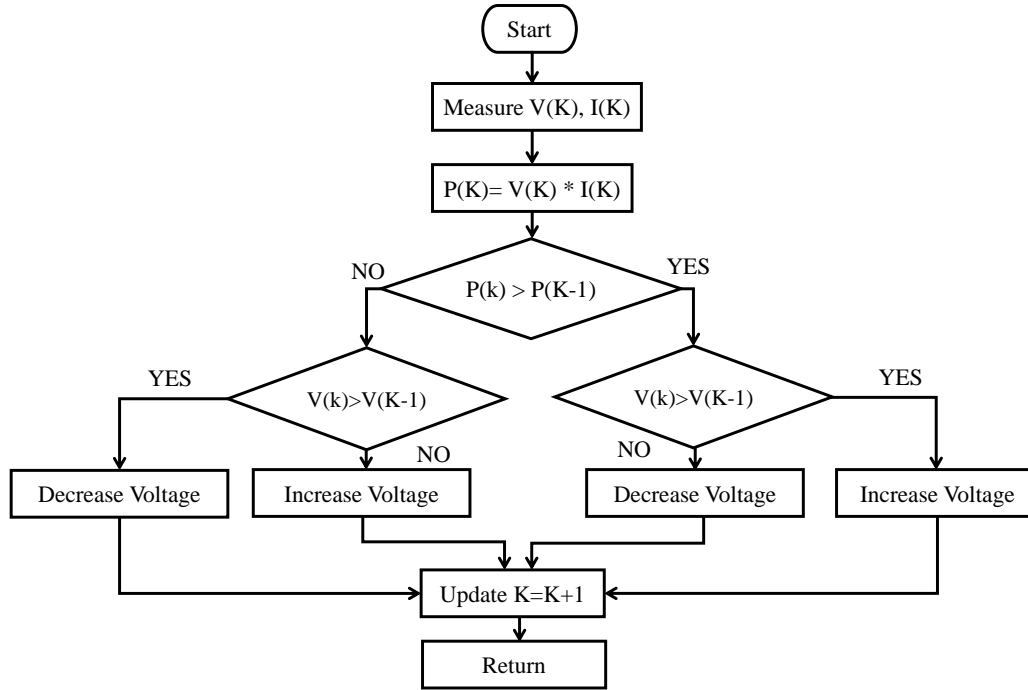


Figure 4.7 Flowchart of *P&O* MPPT algorithm

4.1.3 MMC Based Grid-Connected PV System Configurations

Modular multilevel converters are one of the newly used topologies for PV systems integration [4–9, 23, 42–45], they have gained huge interest from industry and researchers due to their salient features, such as modularity, scalability, lower switching frequency, low components ratings, and high efficiency. For PV applications, the PV system could be either connected to the DC-link of the MMC through as DC-DC converter; and this requires new MMC structure to control the DC voltage, which will be discussed in Chapter 5 in detail. The other configuration takes advantage of the system modularity and allows for distributed PV panels installation. In this thesis, a distributed PV system is proposed to solve the partial shading effects on system performance. The proposed topology and its control design will be discussed in detail in the following section.

4.2 HBMMC based Distributed Maximum Power Point Tracking

To address the centralized PV system partial shading challenges, this work proposes a novel integrated power electronics system that utilizes MMC to connect distributed PV systems using DMPPT across the MMC SMs, given the benefits of DMPPT in solving the partial shading performance issues. An average SM capacitor voltage control algorithm is proposed in this thesis to ensure all the captured solar energy is transferred to the AC grid. The model predictive control (MPC) strategy proposed in [15] is implemented to get the best switching sequences of SMs to control ac-side current, capacitor voltage, and circulating current simultaneously. The algorithms are tested against different case studies to demonstrate their performance.

4.2.1 Topology Design

The proposed three-phase MMC solution is shown in Figure 4.8. It consists of two arms at each phase, where each arm has n SMs. The SMs are HBSMs with two IGBT switches and a capacitor, each connected to one PV module through a DC optimizer. Each SM voltage is either zero or its capacitor voltage v_{ci} depending on the SM switches states. The MMC is connected to the three-phase AC system at the point of common coupling (A, B, and C) through a filter with resistance and inductance of R and L on each phase. Each arm has an inductor (l) placed for current control.

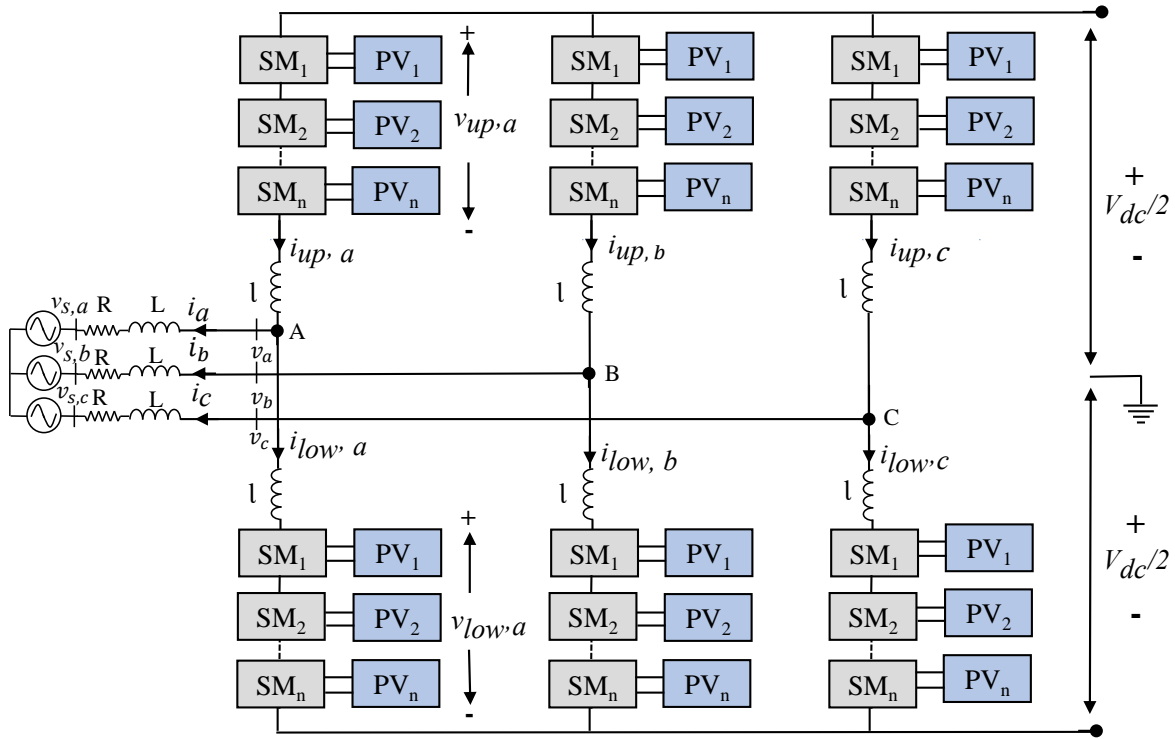


Figure 4.8 Topology of the proposed HBMMC-PV system

The proposed solution is scalable from residential systems size up to utility-scale systems size, by adjusting power and voltage ratings of MMC components or by increasing the number of SMs on each arm.

4.2.2 Distributed MPPT Control Design

4.2.2.1 Distributed PV Modules

The proposed MMC-PV topology removes the PV modules strings connected to the MMC DC side and connects each PV module to the SM DC-link through a DC-DC converter with MPPT

controller as shown in Figure 4.9. With this topology, in case of partial shading, the MPPT controller of each SM captures the maximum power of its PV module by regulating the voltage across the PV module on the MMP voltage (V_{mmp}) at any time. In this work perturb and observe ($P\&O$) method is implemented to control the SM capacitor voltage to (V_{mmp}). The voltage control signal at each time step is defined based on the effect of the previous adjustment on the PV power output as discussed in Section.4.1.2.

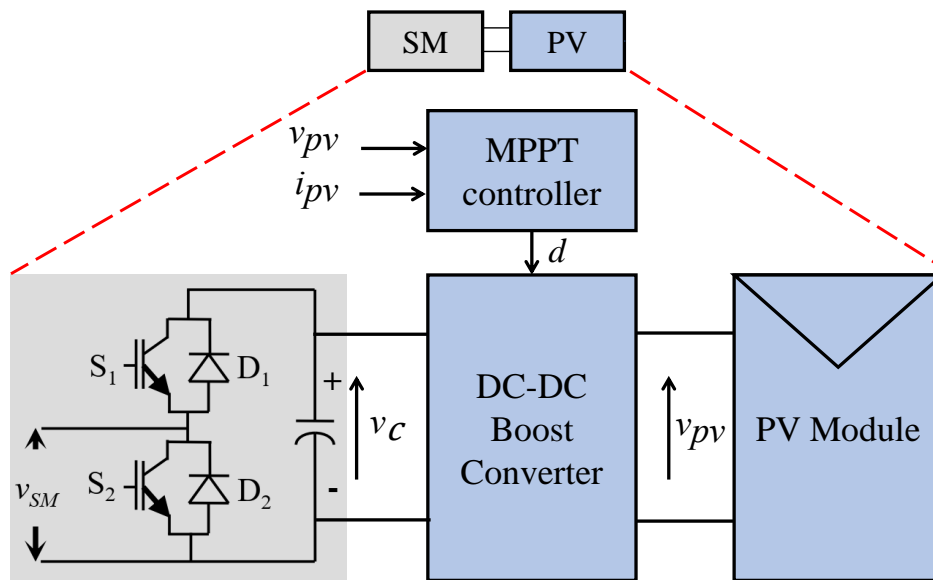


Figure 4.9 Half-bridge SM and PV module connection

4.2.2.2 HBMMC AC output Current Control

The reference AC waveforms i_{abc}^{ref} are controlled to regulate the average voltage of SM capacitors on their nominal values to ensure that no extra energy is stored in the SM capacitors. This control is shown in Figure 4.10 below, it takes the average of measured SM capacitor voltages, the reference value of the average of SM capacitor voltages and the grid reference current to get

the AC output current that should be sent to the grid. The instant total power of distributed PV modules is applied to minimize transients. The PI controller acts upon the average SM capacitor voltage deviation from its nominal value to generate a control signal in terms of a reference current on a direct axis i_d^{ref} . With an addition of a quadrature axis component of current i_q^{ref} , the generated dq -component of current Δi_{dq}^{ref} is added to the dq -components of actual output current (i_{dq}). The total output signal is finally converted into abc -frame and the AC reference current i_{abc}^{ref} is fed to the MMC switching algorithm.

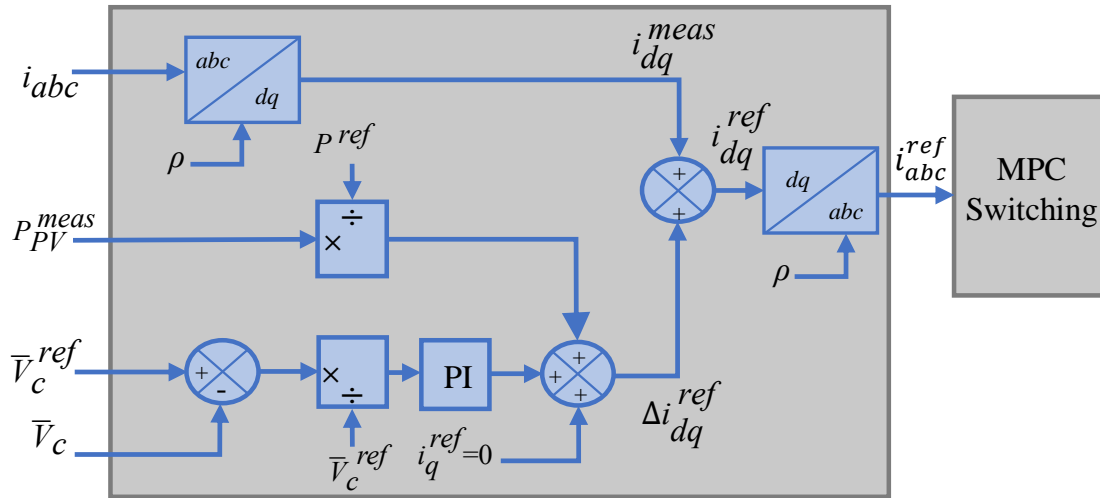


Figure 4.10 HBMDC AC output current control

4.3 Case Study

4.3.1 Simulation Setup

The proposed topology is simulated on MATLAB and tested to verify the performance of MMC and the control methods. Since each SM is connected to a PV array, the focus is to control the

SM capacitor voltage under partial shading conditions and guarantee the tracking of the maximum power. The system has 36 solar PV Panels individually controlled via a *P&O* DMPPT method, and their Parameters are listed in Table 4.1. The MMC parameters are given in Table 4.2. The PV array temperature input is assumed to be 25 C° all the time. To study the partial shading, the irradiance data was provided by the PV Power Research Plant of Tampere University [72]. The simulations were run for 3 seconds and the system was tested under severe partially cloudy conditions. Given that the MMC simulated has 6 SMs, the case study is designed such that no partial shading occurs on SMs 1-4 of all arms; thus, they are exposed to 100% of their associated irradiance. On the contrary, SMs 5-6 of all arms are shaded and receive 20% of their associated irradiance. The following discussions are focused on the performance of MMC to realize DMPPT.

Table 4.1 Solar PV Array Data

Parameter	value
Module	SunPower SPR-305E-WHT-D
Maximum Power	305.226 W
Cells per module	96
Open circuit voltage (V_{oc})	64.2 V
Short-circuit current (I_{sc})	5.96 A
Voltage at MPP (V_{MPP})	54.7 V
Current at MPP (I_{MPP})	5.58 A
Temperature coefficient of V_{oc}	-0.27269 %/ C°
Temperature coefficient of I_{sc}	0.061745 %/ C°

Table 4.2 HBMMC Parameters

Parameter	Value
Number of submodules per arm	6
Active power delivery	10.9 kW
Nominal DC voltage V_{DC}	600 V
Sampling period T_s	25 μ s
Output current reference I_{ref}	16 A
Submodule capacitor C_{sm}	5000 μ F
R	0.003 Ω
L	5 mH
l	5 mH

4.3.2 MMC Control Performance Under Partial Shading Condition

In this case, PV arrays on the MMC SMs receive fluctuating irradiance in normal operation. Figure 4.11 shows the irradiance and the output power of phase A upper arm SMs, It shows that the power output of PV modules changes with their own irradiance. The PV arrays on SM 5-6 receive extremely low irradiance (20%) due to partial shading. From Figure 4.11, the power output of the PV systems connected to these SMs is around 100 Watt since the irradiance never exceeds 250 $Watt/m^2$. Although, these PV modules are partially shaded, the PV modules connected to SMs 1-4 are not affected and work at their maximum power point. Therefore, the efficiency of the system is maximized by individually controlling the PV arrays.

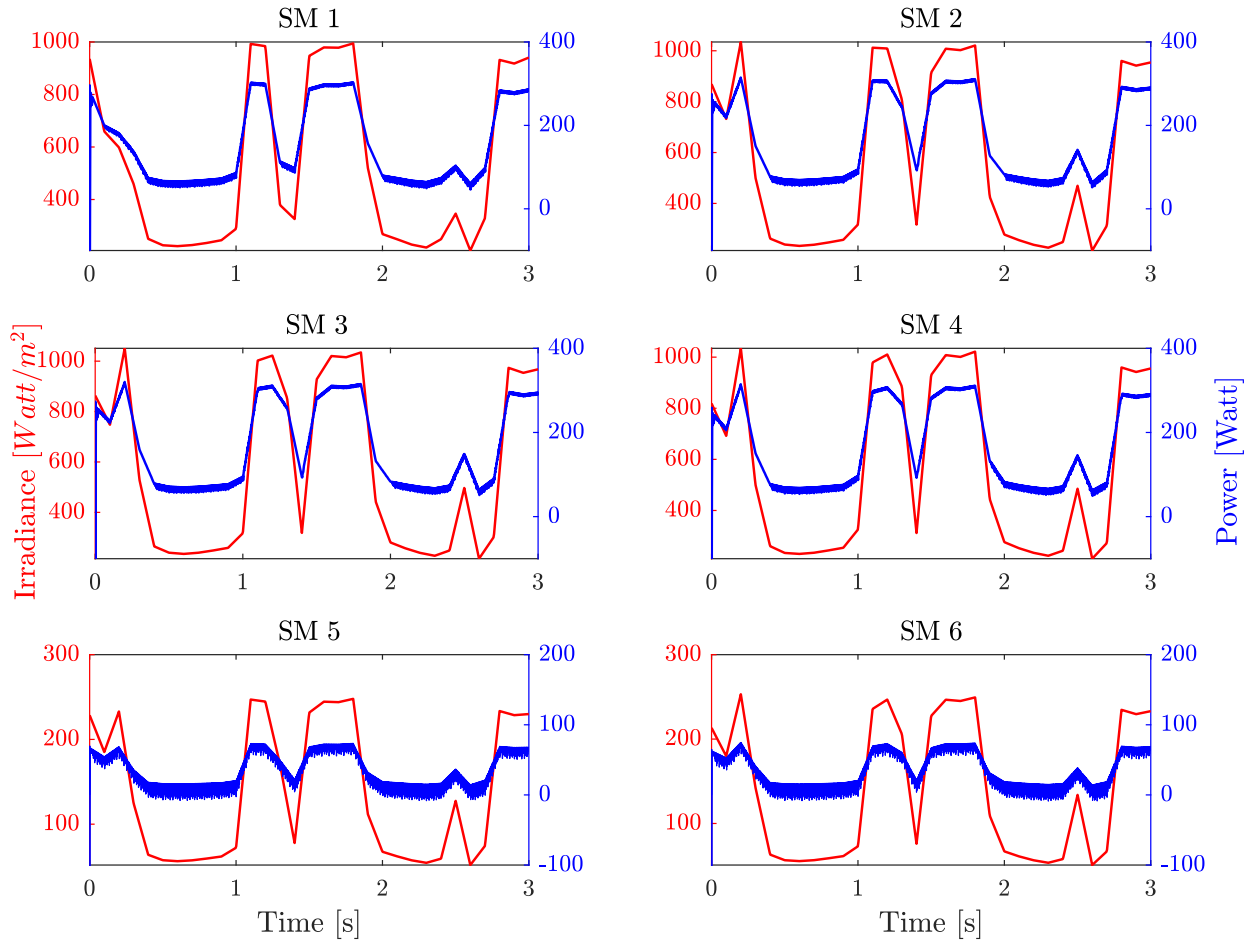


Figure 4.11 Phase A upper arm submodules irradiance and power. The figure is shown in double-axis format where irradiance and power are shown in different colors (red and blue) on the left and right axes, respectively

4.3.3 MMC Modulation Performance

Other than capturing the maximum power from individual PV modules, it is important to ensure that MMC operates as expected at all times. Parameters of interest are SM capacitor voltages, AC current waveform, and circulating current.

Figure 4.12 shows capacitor voltages of all SMs on phase A upper and lower arms. The results show that capacitor voltage waveforms of upper arm SMs match each other at any time

regardless of partial shading condition. The same behavior is observed for capacitor voltage waveforms of lower arm SMs. This proves perfect performance of the SM capacitor voltage balancing implemented in MPC-based switching algorithm. Moreover, the fact that the average SM capacitor voltage of MMC is controlled within a $\pm 3\%$ demonstrates that the AC output current control shown in Figure 4.10 successfully transfers the entire solar energy captured from PV modules to the AC power grid and no energy is accumulated on SMs of MMC.

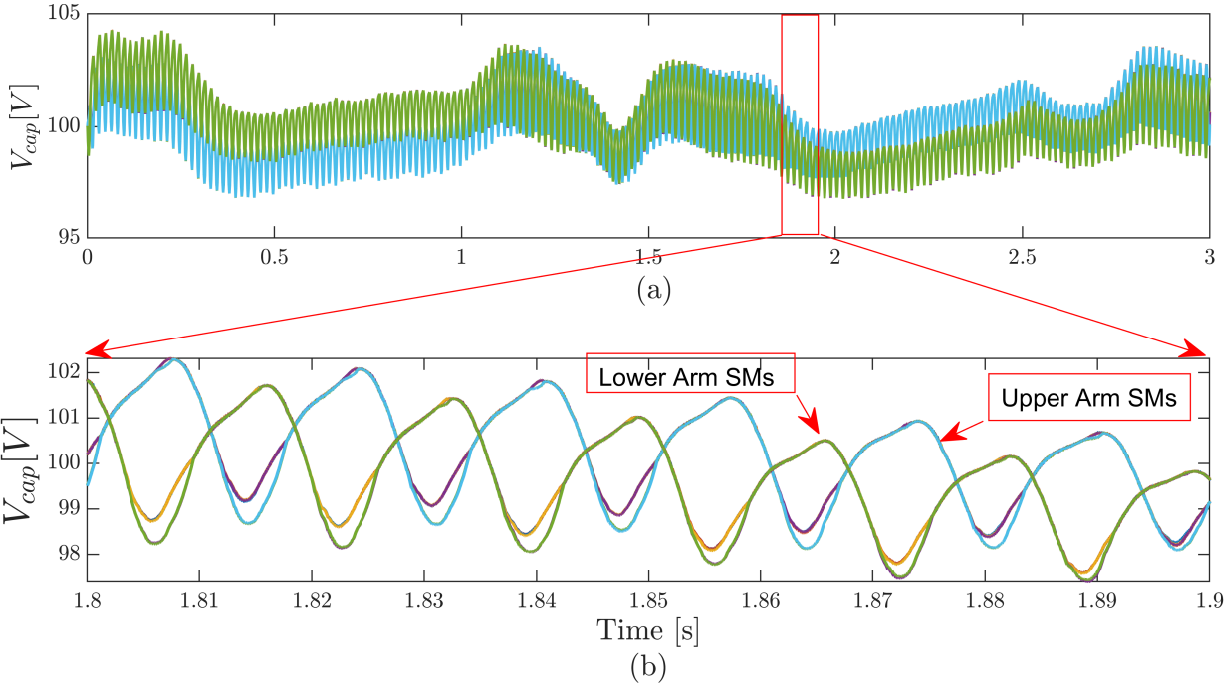


Figure 4.12 (a) Phase A upper and lower arms SMs voltage for the whole simulation time 3s, (b) a zoom on phase A upper and lower arms SMs voltage for 0.1s

The other objectives of the MPC-based switching algorithm are AC current waveform tracking and circulation current mitigation. Despite all the abnormal PV conditions simulated, Figure 4.13 illustrates that the AC output current of phase A is tracked perfectly during the whole simulation time. Circulating current of phase A is also minimized around zero throughout the simulations as depicted in Figure 4.14. Similar results are observed for other phases of MMC but not shown here to avoid the repetition of similar results.

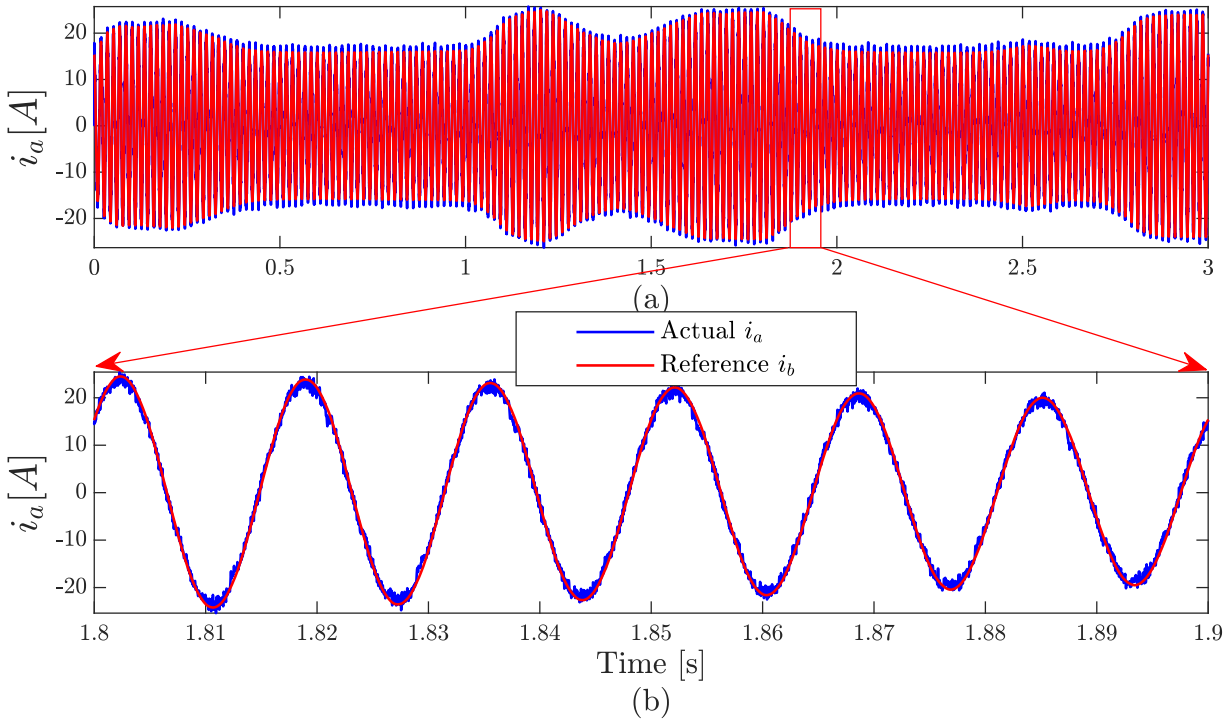


Figure 4.13 (a) Phase A AC output current tracking for the whole simulation time 3s, (b) a zoom on Phase A AC output current tracking for 0.1s showing the actual current i_a and the reference current i_b

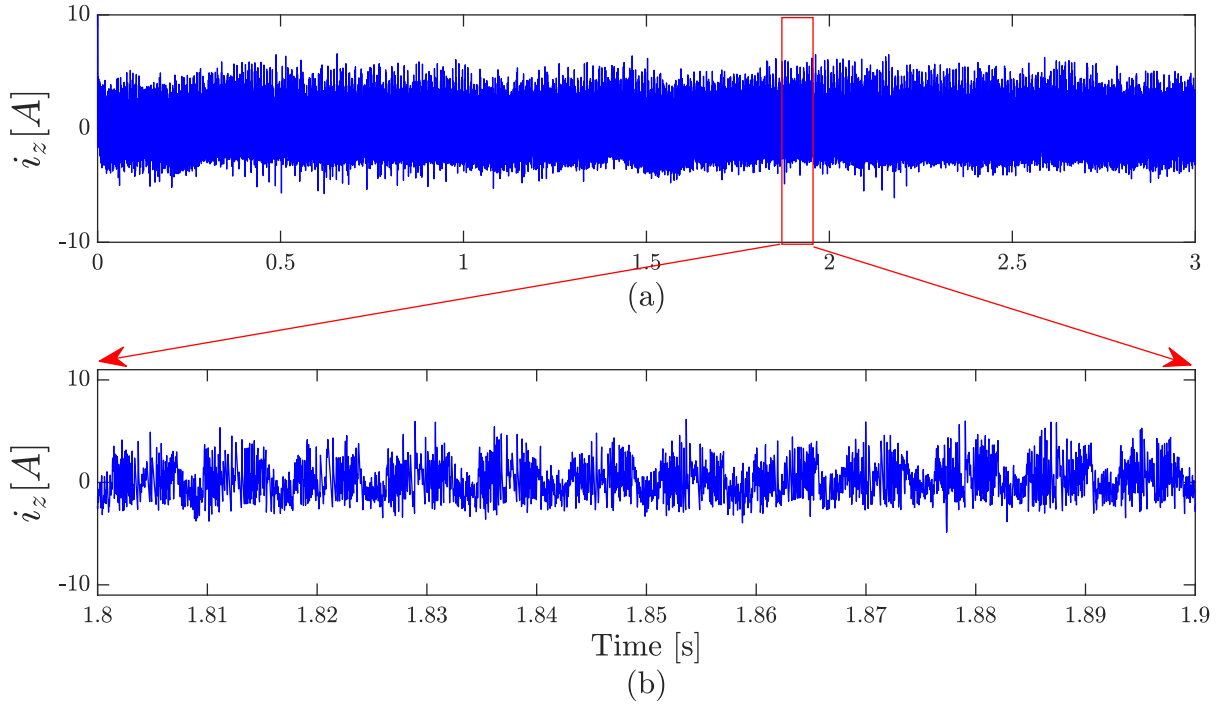


Figure 4.14 (a) Phase A circulating current for the whole simulation time $3s$, (b) a zoom on Phase A circulating current for $0.1s$

4.4 Model Predictive Control Computation Requirements

4.4.1 MPC Computation Background

The conventional MPC algorithm from [39] requires a considerable computation time since it compares all the feasible switching sequences for the MMC switches in one bridge for their anticipated performance one time-step ahead. While the algorithm computation at any time should not take more than one time-step. The algorithm needs to check the optimal switching state among all C_{2n}^n switching combinations, which will increase significantly as the number of SMs n at each arm increases. However, the utilized MPC algorithm in this work from [15], cuts down the number of combinations to 4 possible solutions and then selects the best solution. Even though the number of

combinations is decreased, the computational burden to solve the SM sorting and selection process is one of the main challenges of MPC switching. In case the computation process takes more than a one time step, the algorithm will apply the previous switching sequence to the SMs.

4.4.2 MPC Computation Expenses

To investigate the computational time elapsed to solve the sorting and selection operations of the MPC optimization problem, we dedicated a computer with good processor properties. The test was conducted in two different computers with different processor proprieties to observe the effect on the computation time.

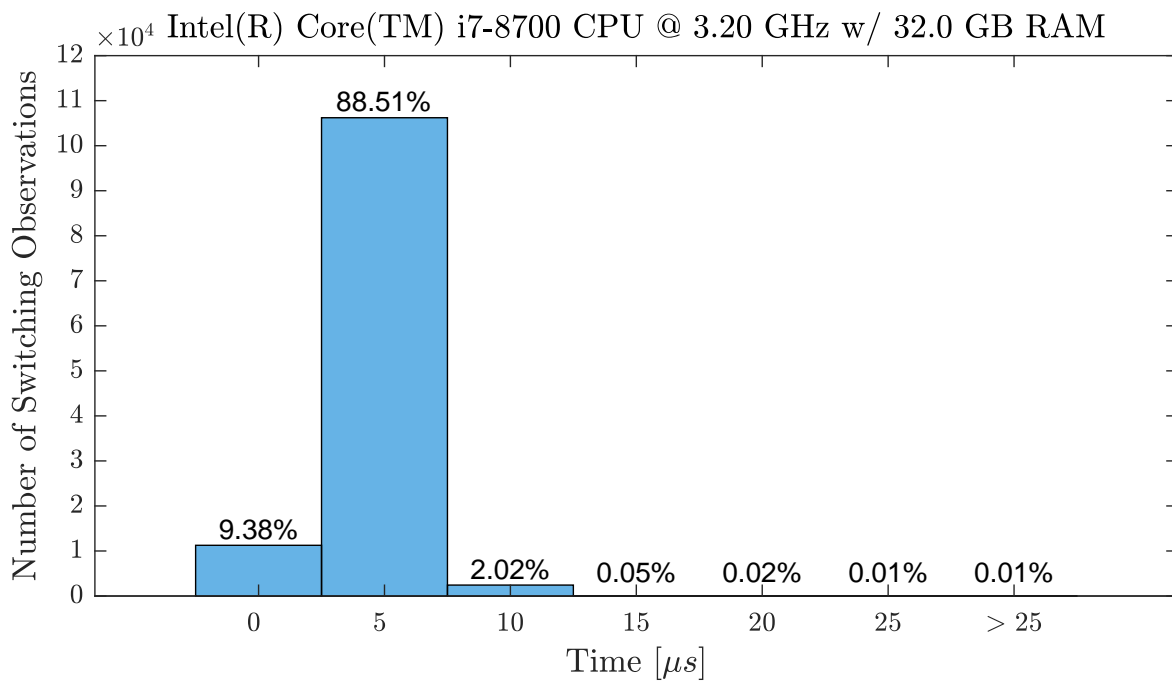


Figure 4.15 MPC computation time Statistics in Computer 1

The statistics of the first test on computer 1 are illustrated in Figure 4.15, it shows that 99.99% of the switching observations obtained in less $25\mu s$. This means the computation time took more than one time-step in just 0.01% of the time. Also, it is noticed that the majority of the switching observation took $5\mu s$ or less to get solved. While the statistics of the second test on computer 2 are shown in Figure 4.16. The results show that 99.99% of the switching observations obtained in less $25\mu s$. Also, it is shown that 99% of switching observation took $5\mu s$ or less to get solved. This proves the efficiency and reliability of the utilized MPC switching technique.

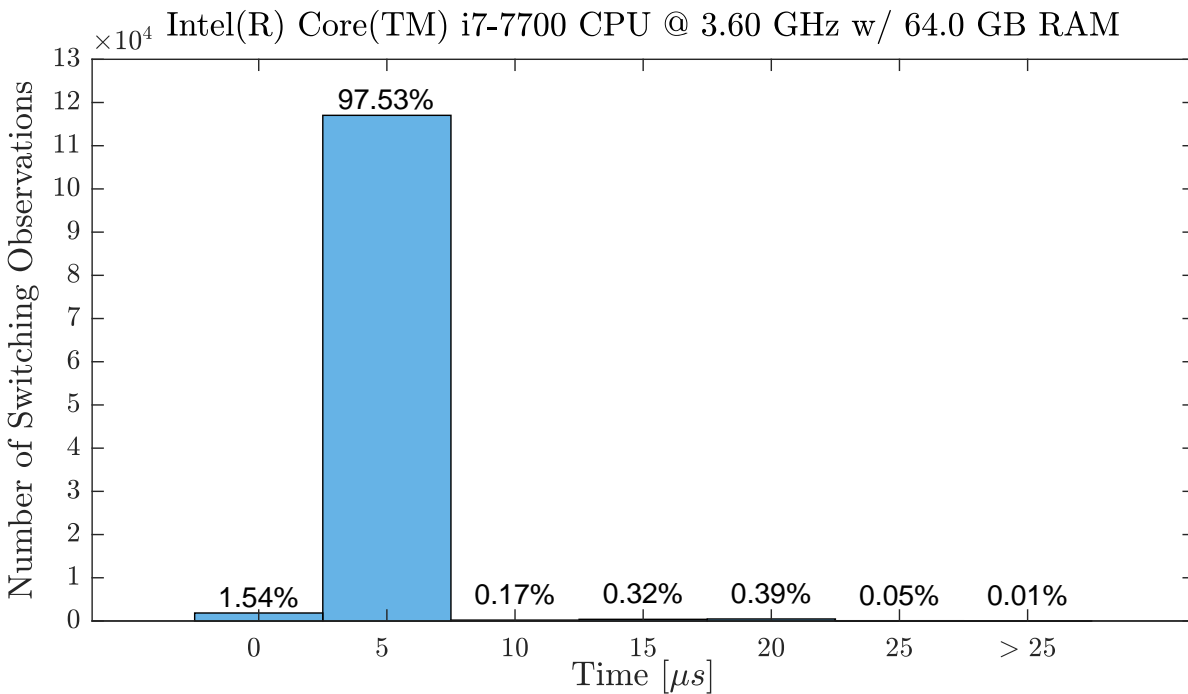


Figure 4.16 MPC computation time Statistics in Computer 2

CHAPTER 5
FBMMC FOR SOLAR PHOTOVOLTAIC-BATTERY ENERGY STORAGE SYSTEM
INTEGRATION

This chapter reviews the challenges of solar PV integration to the power grid and the role of battery energy storage system (BESS) in addressing these challenges; covers the application of BESS in support power grid ancillary services; presents the limitations of conventional HBMMC in renewable energy integration. In this chapter, a FBMMC-based solution is proposed to integrate distributed PV modules to the full-bridge SMs and interface a BESS to the MMC DC-link. The interfaced BESS is used to support the grid ancillary services. A 13-level FBMMC is tested to validate the performance of the proposed topology and its control systems.

5.1 MMC-Based PV-BESS systems

5.1.1 Background

Renewable energy resources integration to the power grid presents a challenge to power system stability and reliability due to its intermittent nature and fluctuated power output [73]. Among renewable energy resources, solar Photovoltaic energy penetration has increased rapidly during the past decade and the PV generation increased almost 50 times just between 2008 and 2018. All this poses concerns over a reliable and efficient operation of the power network. One of the promising solutions to tackle these concerns, is the integration of BESS to the power system network. This

solution is getting more attraction in the past few years since BESS costs are projected to decrease by 10-52% by 2025 [74]. Moreover, BESS has great features such as high energy density and fast response as they can go from charge to discharge mode in a range of a few milliseconds. Given all that, BESS is coupled to PV systems to address the intermittency challenges and support the power grid operation. This chapter proposes a FBMMC solution to integrate PV and BESS to the power grid using a single converter as described later.

5.1.2 Applications of BESS for Power Grid Support

There are several applications for BESS in power grid support whether in the generation, transmission, or distribution. These applications have been reviewed and analyzed in [75], some of them are summarized below:

- i. Spinning reserve: due to the fast response of BESS, it can be charged and hold just to be used in the events of generation failure and prevent power supply interruption.
- ii. Commodity storage: the BESS is charged during the off-peak time and then its used in economic dispatch during peak times. This includes peak shaving and load leveling.
- iii. Frequency control: The BESS is used to support the grid as a reserve generation that can be used in the events of frequency deviation.
- iv. Renewable energy management: in this application, BESS is charged by renewable energy resources and this energy is used during peak hours.
- v. Power quality and reliability: BESS is used to improve the power quality by utilizing it to avoid voltage flickers and power outages that lasts for a few cycles.

In this work, the BESS is used to support the grid in two applications, load following, and frequency control support as discussed later in section 5.2.4.4.

5.1.3 Advantages of FBMMC over HBMMC for DER Integration

Figure 5.1 from [58] depicts the operating regions of both HBMMC and FBMMC. Also, as explained in [58, 65] and as shown in the Figure 5.1(c), HBMMC requires constant V_{dc} ($= \frac{\pi}{\sqrt{6}} V_a$) voltage on the DC side to generate the sinusoidal AC-side RMS voltage of V_a . This inflexibility in the DC-link is the main reason for conventional MMC not being able to be applicable in the grid integration of DERs, which requires flexibility on the DC side.

However, with the FBMMC, as shown in Figure 5.1(d), FBMMC can provide the flexibility in the DC-link to generate the output AC side voltage with V_a even when there is DC-link voltage from $[-V_{dc}, +V_{dc}]$. Employing full-bridge SMs (FBSMs), the topology gives the control algorithms enough flexibility to set the DC-link voltage to any voltage value in $[-V_{dc}, V_{dc}]$ while maintaining the capability of being connected to the same AC grid. Therefore, FBMMC is well suited for the integration of PV and BESS to the AC power grids.

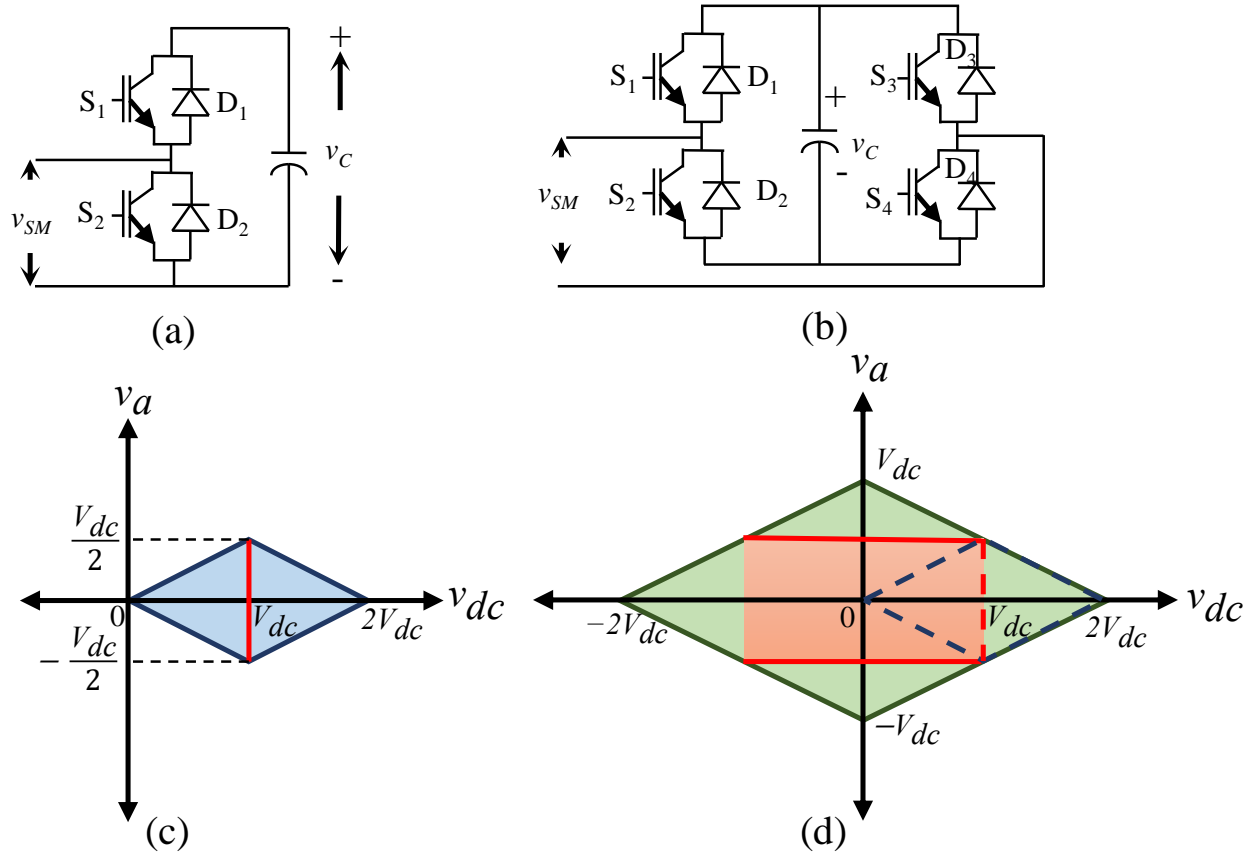


Figure 5.1 Configuration and operating region of (a)(c) HBSM (b)(d) FBSM

5.2 System Topology and Modulation Design

5.2.1 System Configuration

This work proposes a novel FBMMC-based solution to interconnect PV-BESS to the power grid with PV arrays interfaced with SMs and a BESS connected to DC-link. The System configuration of the proposed three-phase MMC PV-BESS is shown in Figure 5.2. It consists of three legs, represents the system three phases, each phase has 2 arms namely upper and lower arms, where each arm has n SMs that are connected in series an arm inductor (l), it helps for current control and DC side faults limiting. The SMs are FBSM, each consists of four IGBT switches and a capacitor

and connected to one PV module through a DC-DC converter. A high-voltage BESS is connected to the DC-link capacitor of the MMC. The MMC is connected at the point of common coupling (A, B, and C) with the AC grid system through a filter with resistance and inductance of R and L on each phase.

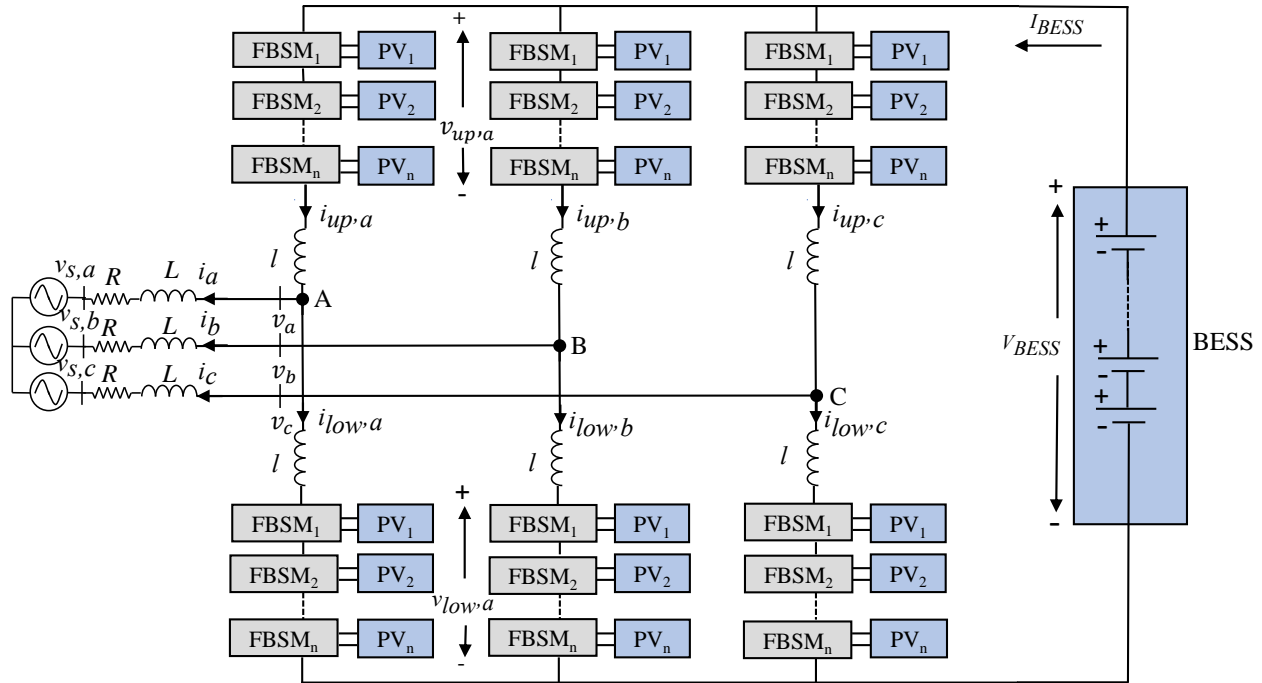


Figure 5.2 The FBMMC-based PV-BESS configuration

5.2.2 FBMMC Mathematical Model

Similar to the mathematical model proposed in [15] for HBMMCs, we develop a discrete-time model for the MMC system shown in Figure 5.2 in this section.

Figure 5.3 shows the proposed FBSM integrated with PV modules through a DC-DC converter with an MPPT controller. Similar topology—but with half-bridge SM (HBSM) instead of

FBSM—has been analyzed in chapter4. Unlike a HBSM the voltage across which is either zero or equal to its capacitor voltage ($+v_C$), there are three options of $\{0, +v_C, -v_C\}$ for voltage across an FBSM depending on the IGBT switching states.

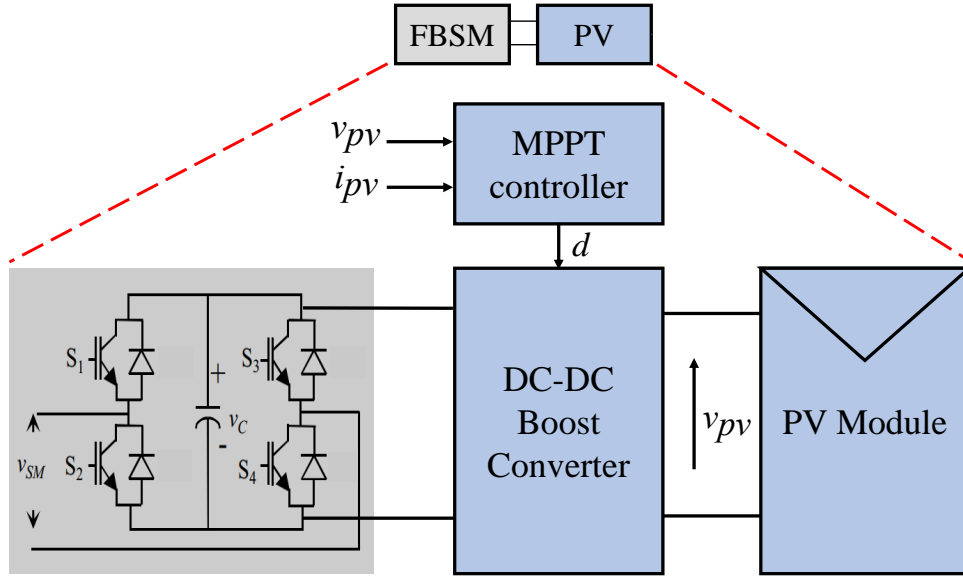


Figure 5.3 Full-bridge SM and PV module connection

The anticipated capacitor voltage of individual SMs on upper-level and lower-level arms is equivalent to:

$$v_{C_j}(t + T_s) = v_{C_j}(t) + \frac{T_s}{C} \left(u_j(t + T_s) i_{up}(t) + \frac{P_{PV_j}}{V_{C_j}(t)} \right) \quad (5.1)$$

for any $j \in [1, n]$, and

$$v_{C_j}(t + T_s) = v_{C_j}(t) + \frac{T_s}{C} \left(u_j(t + T_s) i_{low}(t) + \frac{P_{PV_j}}{V_{C_j}(t)} \right) \quad (5.2)$$

for any $j \in [n + 1, 2n]$, where $u_j(t + T_s) \in \{-1, 0, +1\}$ is the status of j -th SM.

Euler's approximation of the current derivative that represents the AC-side current next step value can be defined as:

$$i(t + T_s) = \frac{1}{K'} \left(\frac{v_{low}(t+T_s) - v_{up}(t+T_s)}{2} - v_s(t + T_s) + \frac{L'}{T_s} i(t) \right) \quad (5.3)$$

where the time step T_s is a small sampling time, $L' = L + l/2$ and $K' = R + L'/T_s$. The measured values at the current time are denoted by time indices (t) and the predicted values for the next time step are denoted by ($t + T_s$). The sampling frequency is assumed to be significantly higher compared to the grid frequency, the predicted value of grid voltage $v_s(t + T_s)$ can be replaced by its measured value $v_s(t)$. Thus, the predicted voltages across upper-level and lower-level arms for the next step are defined as

$$v_{up}(t + T_s) = \sum_{j=1}^n v_{Cj}(t + T_s) u_j(t + T_s) \quad (5.4)$$

$$v_{low}(t + T_s) = \sum_{j=n+1}^{2n} v_{Cj}(t + T_s) u_j(t + T_s) \quad (5.5)$$

and circulating current is equal to

$$i_z(t + T_s) = \frac{T_s}{2l} (V_{BESS} - v_{low}(t + T_s) - v_{up}(t + T_s)) + i_z(t) \quad (5.6)$$

where V_{BESS} is the instantaneous voltage across BESS to control BESS charging or discharging currents.

5.2.3 FBMMC Modulation Design

This section presents the overall switching control design of the proposed MMC system.

5.2.3.1 Model Predictive Control (MPC) Based Modulation

The model predictive control (MPC) strategy employed here is from [15, 40, 41, 76] to determine the best switching sequence to control MMC effectively. At each time-step, the proposed switching algorithm solves an optimization problem that targets the following three control objectives at the very next time-step.

- i. It balances and regulates the submodules capacitor voltages to their nominal value ($v_{C_j} = V_{dc}/n$ for any j).
- ii. It controls the ac-side current of all phases to their reference values ($i = i_{ref}$).
- iii. It suppresses the circulating currents ($i_z = 0$) between the converter phase legs.

As the optimization problem has to be solved in a matter of micro-seconds to be effective, it is very crucial to employ a very fast solution algorithm. In this thesis, we first reformulate the optimization problem based on capacitor voltages of individual FBSMs and set up a sorting+selection algorithm similar to the proposed solution in [15]. Assuming that the exact AC current tracking and exact circulating current suppression can be expressed as $i(t + T_s) = i_{ref}$ and $i_z(t + T_s) = 0$ respectively. The upper and lower level voltages of MMC expected values are calculated as:

$$v_{up}^* = \left(\frac{V_{BESS}}{2} + \frac{l}{T_s} i_z(t) \right) - \left(K' i_{ref} + v_s(t) - \frac{L'}{T_s} i(t) \right) \quad (5.7)$$

$$v_{low}^* = \left(\frac{V_{BESS}}{2} + \frac{l}{T_s} i_z(t) \right) + \left(K' i_{ref} + v_s(t) - \frac{L'}{T_s} i(t) \right) \quad (5.8)$$

Where the ideal value of corresponding variable for the next time step is denoted by $(\cdot)^*(t + T_s)$, let $\Delta i = i - i_{ref}(t + T_s)$, $\Delta v_{low} = v_{low}^* - v_{low}$, and $\Delta v_{up} = v_{up}^* - v_{up}$ denotes the deviation of the corresponding variables from their ideal values. Deviation of the AC current and the circulating current from their anticipated values are equal to:

$$\Delta i = \frac{1}{2K'} (\Delta v_{low}(t + T_s) - \Delta v_{up}(t + T_s)) \quad (5.9)$$

$$i_z(t + T_s) = \frac{T_s}{2l} (\Delta v_{low}(t + T_s) + \Delta v_{up}(t + T_s)) \quad (5.10)$$

A weighted sum method is applied to the optimization problem, where the AC current tracking and circulating current suppression objectives are combined with weights w and w_z respectively. The multi-objective optimization problem below describes the switching algorithm:

$$\min_U \sum_{j=1}^{2n} \left| v_{C_j}(t + T_s) - \frac{V_{dc}}{n} \right| \quad (5.11)$$

$$\min_U f = \left\{ \begin{array}{l} \frac{w}{2K'} |\Delta v_{low}(t + T_s) - \Delta v_{up}(t + T_s)| + \\ \frac{w_z T_s}{2l} |\Delta v_{low}(t + T_s) + \Delta v_{up}(t + T_s)| \end{array} \right\} \quad (5.12)$$

subject to: (5.3) – (5.6)

$$U = [u_1; \dots; u_{2n}]$$

$$u_j \in \{-1, 0, +1\} \forall_{j \in [1, 2n]}$$

Where (5.11) regulates SM capacitor voltages and (5.12) addresses the reference values of AC current tracking and circulating currents suppression.

5.2.3.2 SM Sorting

This sorting process here is similar to the one discussed before in chapter3. The objective function (5.11) is addressed in this step, where the SM are sorted according to their capacitor voltage such that the SMs contributing the most in voltage balancing are given the highest priority. The upper and lower arms SMs are first sorted based on their expected capacitor voltages. i_{up} direction these SM voltages increase or decrease, the SMs are sorted based on their capacitor voltages in the descending order if $i_{up} < 0$ or in the ascending order if $i_{up} \geq 0$. After sorting, define $V_{C_{up}}^{sort} = [V_{C_1}^{sort}, \dots, V_{C_n}^{sort}]$ and $V_{C_{low}}^{sort} = [V_{C_{n+1}}^{sort}, \dots, V_{C_{2n}}^{sort}]$ denote SM voltages on upper and lower arms respectively.

5.2.3.3 SM selection

The FBSM can select any of the three voltage values of $\{-v_c, 0, v_c\}$, which correspond to switching states of ($G_{SM} \in \{-1, 0, 1\}$), hence it could have four switching levels (State 1, State 2, State 3, and State 4), as summarized in Table 5.1.

Table 5.1 Switching states of a FBSM

State	G_{SM}	g_1	g_2	g_3	g_4	v_{SM}
1	1	1	0	0	1	v_C
2	0	1	0	1	0	0
3	0	0	1	0	1	0
4	-1	0	1	1	0	$-v_C$

According to the three-level voltage condition in FBSM which results in extended operating region, MPC algorithms for FBMMC require major modifications, briefly discussed below. For HBMMC, the number of switched-on SMs is calculated by v_{up}^* divided by a nominal SM capacitor voltage (v_C) and is unique.

In FBMMC, however, the upper and lower arm voltages v_{up} and v_{low} can be any voltage values in range $[-V_{dc}, +V_{dc}]$ in order to obtain the AC side voltage $v_a \in [-\frac{V_{dc}}{2}, +\frac{V_{dc}}{2}]$. Therefore, the values of both v_{up}^* and v_{low}^* should range in $[-V_{dc}, +V_{dc}]$. This results in more than one combination of $[N^{+1}, N^0, N^{-1}]$ (number of SMs with $G_{SM} = +1$, $G_{SM} = 0$, and $G_{SM} = -1$ respectively) to achieve v_{up}^* at the upper arm. For instance, if $v_{up}^* = +\overline{v_{up}}$, any combination of $[N^{+1}, N^0, N^{-1}]$ that ensures $N^{+1} - N^{-1} = \frac{v_{up}^*}{v_{up}}$ and $N^0 = n - N^{+1} - N^{-1}$ is a valid answer. The selection algorithm selects the solution with the maximum value of $N^{+1} + N^{-1}$ as the optimal answer to achieve the best SM capacitor voltage balancing, among all of the possible solutions.

5.2.4 Control Systems Design for PV-BESS Integration

5.2.4.1 MPPT for Distributed PV Modules

The proposed MMC-PV topology in Figure 5.3 connects each PV module to one FBSM through a DC-DC converter with an MPPT controller. With this topology, in case of partial shading, the MPPT controller of each SM captures the maximum power of its PV module by regulating the voltage across the PV module on the maximum power point voltage (V_{mpp}) at any time. The perturb and observe ($P\&O$) algorithm is also used here similarly to chapter 4.

5.2.4.2 FBMM AC output Current Control

To satisfy the second objective of MPC—to regulate SM capacitors voltage to their nominal values—the reference AC waveforms i_{abc}^{ref} must be controlled to ensure that no additional energy is accumulated in the SM capacitors. Figure 5.4 shows this control, which regulates the the average voltage of all SM capacitors \bar{V}_c on its reference value \bar{V}_c^{ref} via a PI controller. The discharging power of BESS and instant total power of PVs are applied to minimize transients. The control signal Δi_{dq}^{ref} is added to the d-q components of current measurement to achieve the i_{dq}^{ref} . Applying an inverse park transformation leads to the three-phase AC system reference current i_{abc}^{ref} to be fed into the FBMMC modulation algorithm.

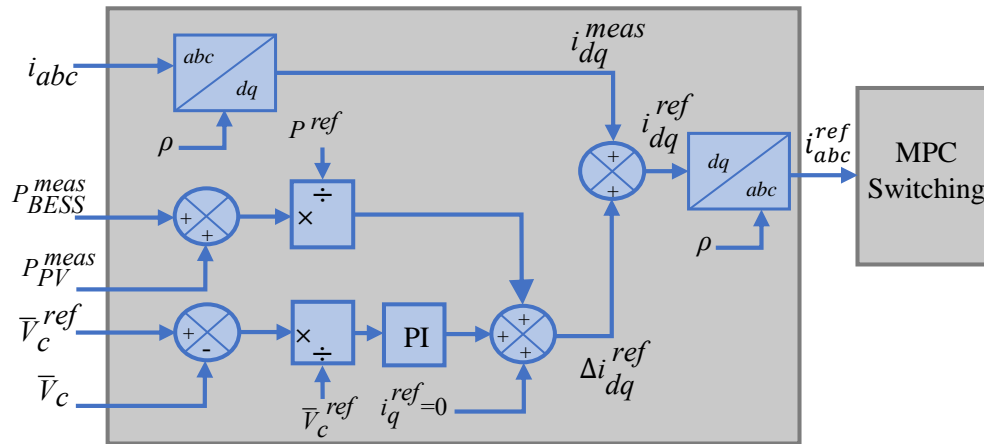


Figure 5.4 FBMMC AC output Current Control

5.2.4.3 Circulating Current Control

When the upper arm voltage v_{up} and the lower arm voltage v_{low} have opposite polarity, any circulating current (i_z) value will cause energy transfer between the arms and hence result in

a voltage difference between them. There are several proposed circulating current control designs that is used to balance the energy allocation between the upper and lower arms in a phase leg as reported in [65, 77]. The circulating current control design proposed in [65] is applied in this work. The operating region of v_{up} and v_{low} of the FBMBC is illustrated in Figure 5.6. When both v_{up} and v_{low} share the same polarity as indicated by the first and third quadrants in the operating region, any applied circulating current will result in voltage drop or rise on all capacitors on both arms. Hence i_z must be regulated to zero in these cases. On the other hand when v_{up} and v_{low} do not share the same polarity as indicated by operating in the second and fourth quadrants in the operating region applying a controlled non-zero circulating current can help in balancing the energy between arms and transfer energy from the arm with higher average capacitor voltage to the one with lower average capacitor voltage. Table 5.2 shows how the reference circulating current i_z^{ref} is expressed for different cases of $\bar{v}_{low} - \bar{v}_{up}$, v_{up}^* , and v_{low}^* . For instance, in the first case, when \bar{v}_{up} is higher than \bar{v}_{low} , while the upper arm voltage is positive and the lower arm voltage is negative. In this case, applying a negative circulating current transfers energy from the upper arm to the lower arm to converge average capacitor voltages of both arms.

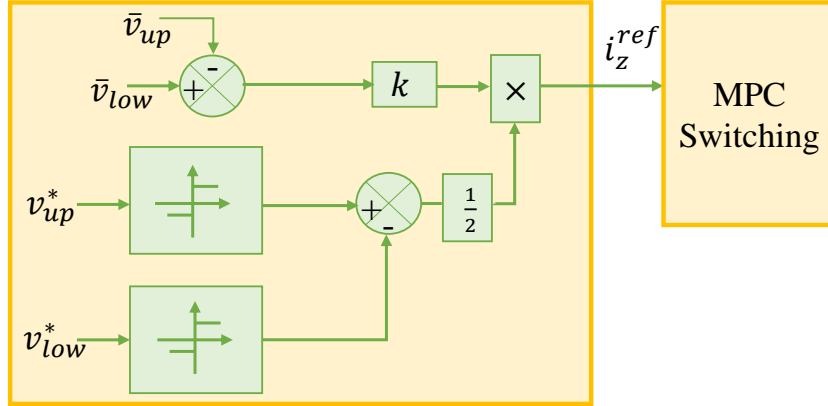


Figure 5.5 Circulating current control

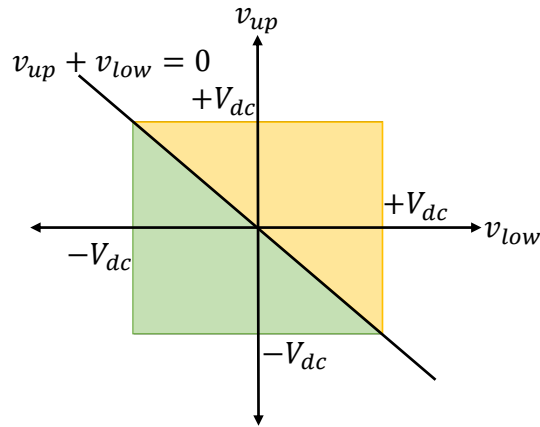


Figure 5.6 Upper arm v_{up} and lower arm v_{low} Operating region

The proposed values for i_z^{ref} in Table 5.2 can be expressed by:

$$i_z^{ref} = \kappa(\bar{v}_{low} - \bar{v}_{up}) \frac{sgn(v_{up}^*) - sgn(v_{low}^*)}{2} \quad (5.13)$$

Table 5.2 Different Cases of i_z^{ref} for all operating region

Case	v_{up}^*	v_{low}^*	$\overline{v_{up}} - \overline{v_{low}}$	i_z
1	+	-	+	$\kappa(\overline{v_{low}} - \overline{v_{up}})$
2	+	-	-	$\kappa(\overline{v_{low}} - \overline{v_{up}})$
3	-	+	+	$-\kappa(\overline{v_{low}} - \overline{v_{up}})$
4	-	+	-	$-\kappa(\overline{v_{low}} - \overline{v_{up}})$
5	+	+	\pm	0
6	-	-	\pm	0

which is used to modify (3.29) as:

$$i_z(t + T_s) = \frac{T_s}{2l} (\Delta v_{low}(t + T_s) + \Delta v_{up}(t + T_s)) = i_z^{ref}. \quad (5.14)$$

Defining the parameter $v_z^{ref} = i_z^{ref} \frac{2l}{T_s}$, the optimization problem of the MPC algorithm is updated to:

$$\min_U \sum_{j=1}^{2n} \left| v_{C_j}(t + T_s) - \frac{V_{dc}}{n} \right| \quad (5.15)$$

$$\min_U f = \left\{ \begin{array}{l} \frac{w}{2K'} |\Delta v_{low}(t + T_s) - \Delta v_{up}(t + T_s)| + \\ \frac{w_z T_s}{2l} |\Delta v_{low}(t + T_s) + \Delta v_{up}(t + T_s) - v_z^{ref}| \end{array} \right\} \quad (5.16)$$

subject to: (3.14) – (3.19)

$$U = [u_1, u_2, \dots, u_{2n}] : u_j \in \{0, 1, -1\} \quad \forall_{j \in [1, 2n]}. \quad (5.17)$$

5.2.4.4 BESS Control for Load Following and Frequency Control

Figure 5.7 shows the control system for the MMC which is responsible for controlling the output power of the MMC, the charging and discharging of the BESS based on the needs of the grid power demand and the grid frequency deviation. The power which MMC should exchange with the grid P_g^{ref} consists of two main parts: (i) the grid demand load following power P_d , (ii) the frequency control power P_f to support the grid frequency by providing some virtual inertia and damping. The MMC total power contribution P_g^{ref} can be described as:

$$P_g^{ref} = P_d + P_f \quad (5.18)$$

The MMC output power measurement P_g^{meas} should always follow the grid requested power P_g^{ref} . The error between these two values is applied to a PI controller to get the reference MMC output power P_g^* .

Virtual Inertia and Virtual Damping Control: the BESS is used to emulate inertia and damping by proportionally relating the BESS active power and the system frequency deviation to get frequency control power contribution P_f . The input to this control circuit is the grid frequency deviation in per-unit $\Delta\omega_g^{pu}$, which deviates from zero only when the system experiences a disturbance *e.g.* due to a load change or a fault. This frequency deviation measurement should be fast and accurate for efficient inertia emulation and fast response, and it is given by:

$$\Delta\omega_g^{pu} = \frac{\omega_g - \omega_g^{ref}}{\omega_g^{ref}} \quad (5.19)$$

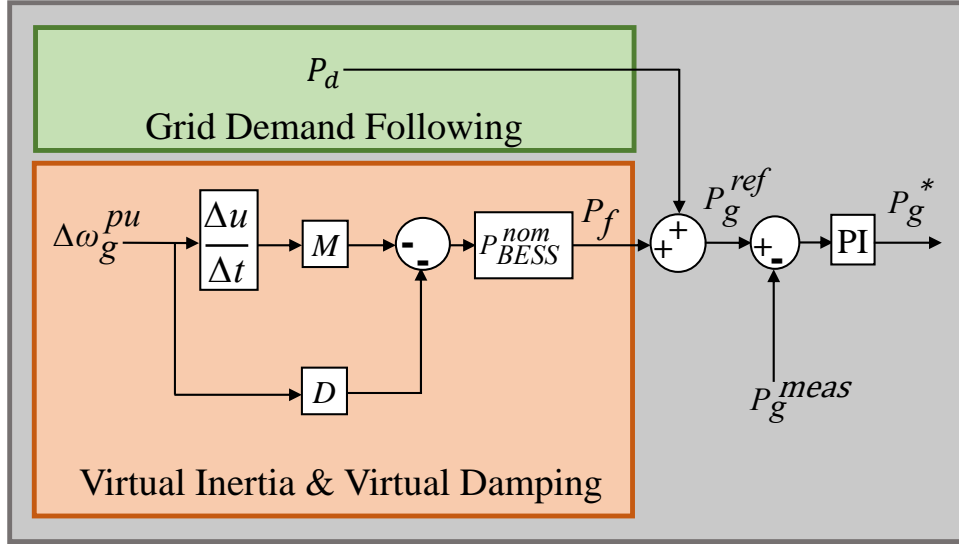


Figure 5.7 MMC Power Control for power grid support

where the measured grid frequency is denoted by ω_g , ω_g^{ref} denotes the reference grid frequency and the superscripts $(\cdot)^{pu}$ and $(\cdot)^{ref}$ stand for the per-unit and reference values respectively (note that $f_g^{pu} = f_g / f_g^{ref} = \omega_g / \omega_g^{ref} = \omega_g^{pu}$). The frequency control power contribution P_f is expressed as:

$$P_f = -M \left(\frac{d\Delta\omega_g^{pu}}{dt} \right) - D\Delta\omega_g^{pu} \quad (5.20)$$

where M is the virtual inertia coefficient, D is the virtual damping coefficient.

BESS Power Control: The BESS supplies the power mismatch between the grid support power P_g^* and the total output power of the distributed PV system P_{PV} . Hence, the distributed PV system output power P_{Pv} is subtracted from P_g^* to get the required power from the BESS P_{BESS}^{ref} ,

which is defined as:

$$P_{BESS}^{ref} = P_g^* - P_{PV} \quad (5.21)$$

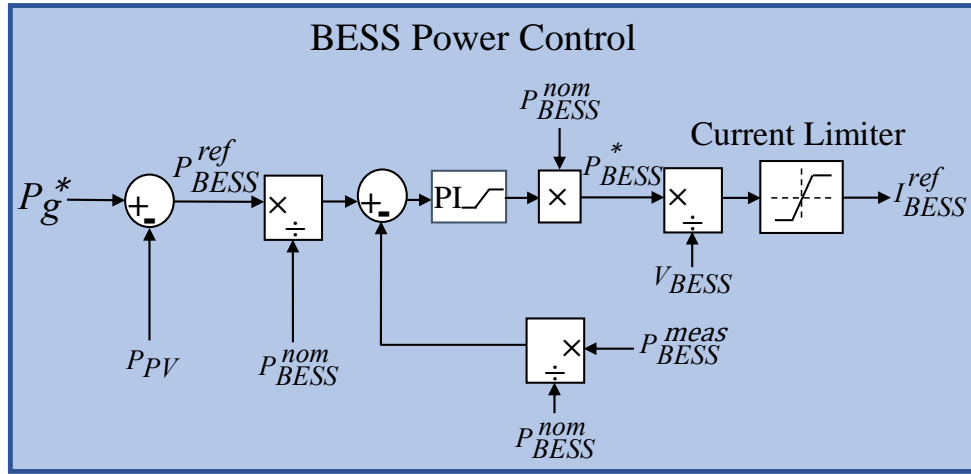


Figure 5.8 BESS Power Control for power grid support

Based on the real time BESS power measurement P_{BESS}^{meas} , the PI controller controls the BESS power and tries to make the mismatch equal to zero and get the required BESS power P_{BESS}^* . Since the BESS voltage V_{BESS} is relatively fixed, the power can be controlled by the current I_{BESS}^{ref} which is formulated as:

$$I_{BESS}^{ref} = \frac{P_{BESS}^*}{V_{BESS}} \quad (5.22)$$

5.2.4.5 BESS State of Charge Management

To stay within the BESS power rating limits the PI controller has an output saturation limits (1,-1 pu). Also, a current limiter is applied for BESS state of charge (SOC) control whose operation criteria is depicted in the flowchart shown in Figure 5.9. The BESS stops the charging or discharging operation when the SOC reaches some preset values as maximum and minimum thresholds.

When $SOC \geq 90\%$, the minimum BESS current I_{BESS}^{min} is set to zero to force BESS current to be positive (Discharging). The maximum BESS current I_{BESS}^{max} is set to the nominal BESS current I_{BESS}^{nom} since the discharge operation is not limited by the SOC. On the other hand, when the $SOC \leq 10\%$, the maximum BESS current I_{BESS}^{max} is set to zero to force the BESS current just to be negative (Charging). The minimum BESS current I_{BESS}^{min} is set to negative of the nominal BESS current $-I_{BESS}^{nom}$ to enable any charging operation within the normal limits.

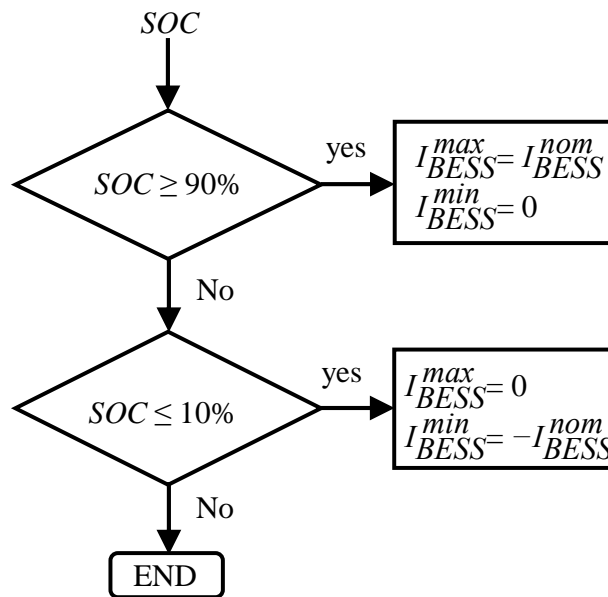


Figure 5.9 BESS SOC Control Flowchart

5.2.4.6 BESS current control

To control the BESS charging/discharging current, the BESS power control block sends the BESS reference current I_{BESS}^{ref} signal, as shown in Figure 5.10. To regulate the measured BESS current I_{BESS} to its reference I_{BESS}^{ref} , the error ΔI_{BESS} between them is obtained and regulated via a PI controller. Since I_{BESS} can be controlled by adjusting the DC-link voltage, the measured DC-link voltage V_{dc} is regulated to the output of the first PI controller to obtain the reference DC-link voltage V_{dc}^{ref} which is then fed to the MMC switching algorithm.

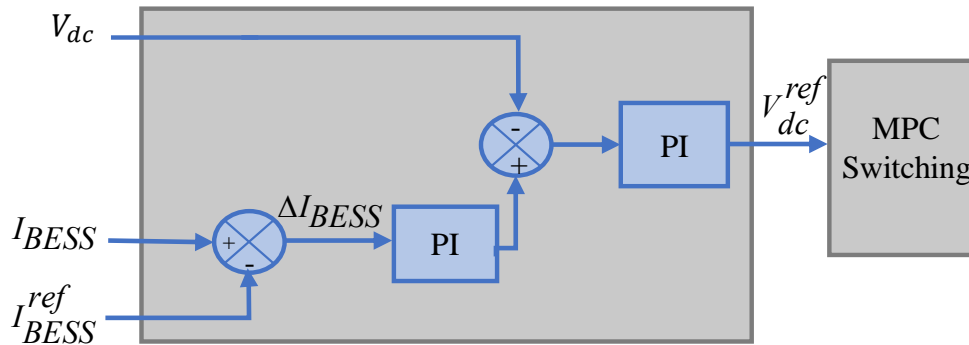


Figure 5.10 BESS current control

5.3 Case Study

5.3.1 Simulation Setup

The proposed three-phase MMC PV-BESS system is simulated in MATLAB/Simulink software environment. The system is tested to evaluate its performance and demonstrate the effectiveness of the proposed control methods. The MMC PV-BESS has 6 SMs per arm, where each FBSM is connected to a PV Module with the same specification to the PV module that used in chapter 4,

Table 4.1. The system has a total of 36 solar PV Panels individually controlled through a *P&O* DMPPT method with overall STC power rating of the distributed PV system is 10.98 kW. The BESS is connected to the DC-link of the MMC and it has a capacity of 270 Ah, the rest of its parameters are shown in Table 5.3 and MMC parameters are given in Table 5.4.

The distributed PV system is tested under partial shading conditions in a similar setup to section 4.3 to demonstrate the system capability to track the maximum power the whole time. In this setup, all SMs receive time-varying irradiance. We assumed that SMs 1-4 of all arms receive the same irradiance, and SMs 5-6 of all arms receive 20% of this irradiance. The system is tested for two case studies. In the first case, we demonstrate the PV-BESS system ability to follow the grid demand and control. In the second case, we evaluate the system performance in inertia and damping emulation to provide frequency support to the grid while following the grid power demand.

Table 5.3 BESS Parameters

Parameter	Value
Storage energy capacity	270 Ah
Rated energy capacity	108 kWh
Nominal discharge Power	46.95 kW
Nominal BESS voltage	400 V
Nominal discharge current I_b^{nom}	117.4 A
Minimum State of charge SOC_{min}	10 %
Maximum State of charge SOC_{max}	90 %

Table 5.4 FBMMC Parameters

Parameter	Value
Number of submodules per arm	6
Active power delivery	57.9 kW
Nominal DC voltage V_{DC}	600 V
Sampling period T_s	25 μ s
Submodule capacitor C_{sm}	20 mF
R	0.003 Ω
L	0.5 mH
l	0.5 mH

5.3.2 Case 1: PV-BESS for Grid Demand Load Following Support

5.3.2.1 FBMMC Power Control

In this case study, the proposed FBMMC is tested for supporting the grid demand load following and to validate that the MMC output power will always follow that demand load. The distributed PV system receives a fluctuating irradiance with severe partial shading based on the data from the case study in Chapter 4. Where it is also validated, that the maximum PV power is extracted since each PV module is individually controlled. The overall PV output power is shown in Figure 5.11, where it fluctuates between 1.5 – 8kW.

For $t \in [0s, 0.5s]$, the grid demand load is 5kW, when the PV output power is higher than this load, the extra power is stored in the BESS as depicted by the negative power. However, when the load is higher than the PV output power, the needed power is supplied by discharging the BESS as indicated by the positive BESS power. For the whole simulation time, the BESS reference power is updated based on this power mismatch.

As shown in Figure 5.11, the MMC output power to the grid is following the grid demand load. All the control systems are enabled after 1 cycle, hence the MMC power starts to build up after a short period. There's a slight overshoot in the MMC output power when the grid load changes, but the control system tracks the reference power the whole time.

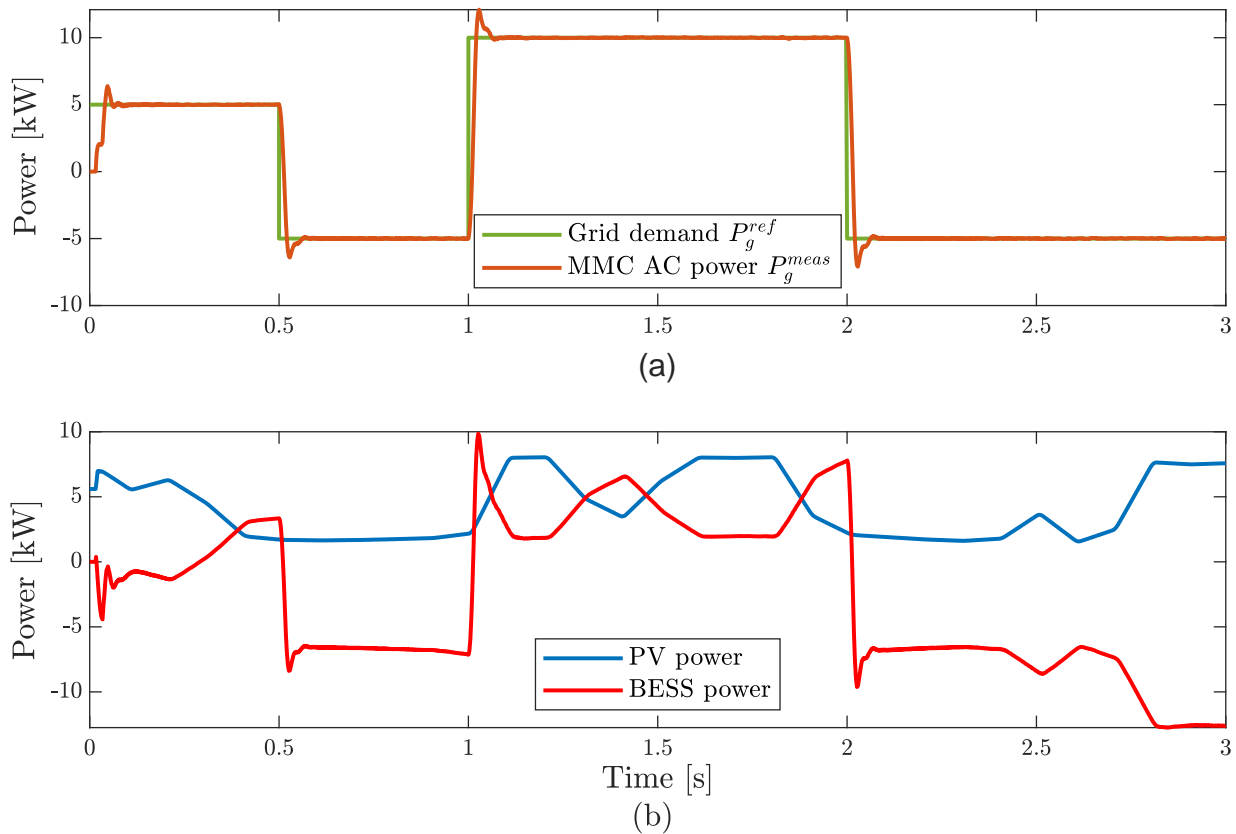


Figure 5.11 (a) Grid power demand and the MMC output power to the grid and (b) the distributed PV system output power and the BESS power for grid demand following support

Figure 5.12 shows the BESS operation parameters when it is used to support the grid demand load following. The BESS started with initial SOC of 50%, this SOC is changing proportionally with charging/discharging operation. It decreases when the BESS current is positive (discharging

operation), and the SOC increases when the BESS current is negative (charging operation). However, there is a slight change in the BESS SOC because the used BESS has a size of $270Ah$, with a rated energy capacity of $108kWh$ as indicated in Table 5.3. This BESS size is very large compared to the consumed power during this short simulation time, with a minimal effect on the SOC. The BESS voltage is fluctuating around $431V$ to allow the charging or discharging operation based on the BESS reference power.

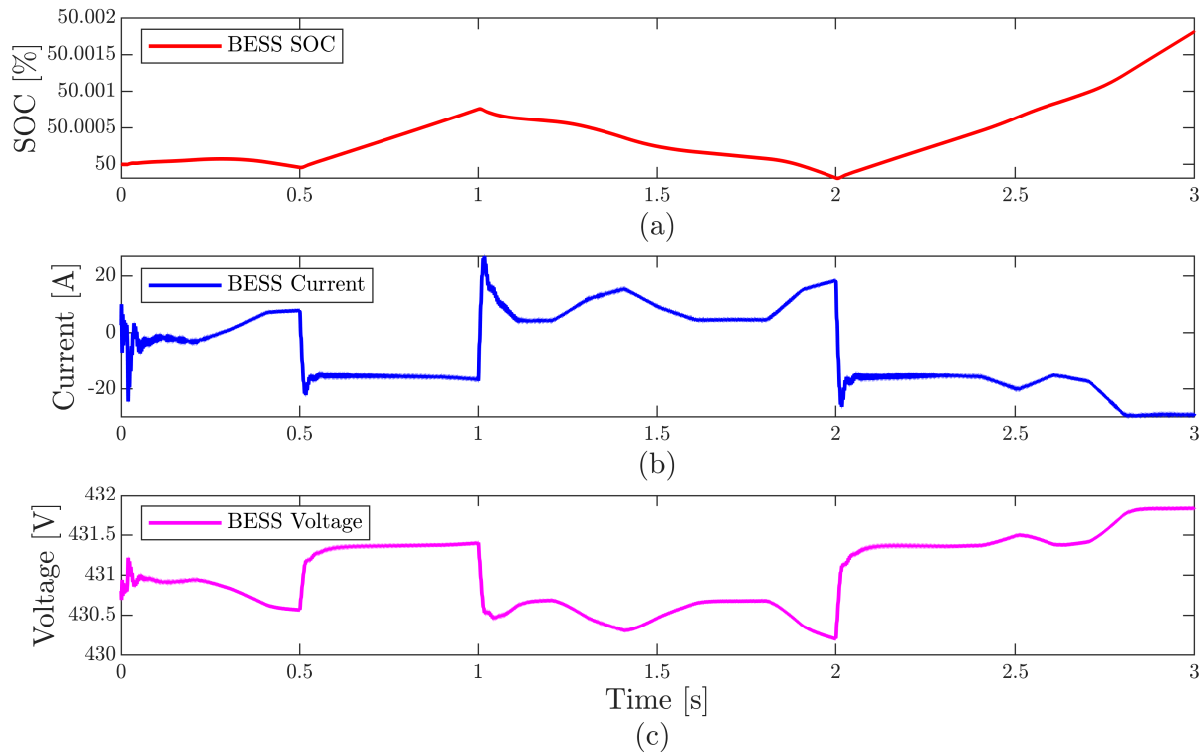


Figure 5.12 BESS Parameters when it is used for grid demand following support, (a) BESS state of charge (SOC), (b) BESS charging/discharging current and (c) the instantaneous voltage across the BESS

5.3.2.2 MMC Performance With Circulating Current Control

Figure 5.13 shows that phase A upper and lower arms SMs capacitor voltages with the circulating current applied. They are regulated to their reference value within less than $\pm 3\%$ regardless of the fluctuated PV power output, variable grid demand or the BESS charging or discharging operation. This proves that the entire captured power from the PV modules and the BESS is transferred to the grid and the SMs of MMC are not storing any energy. Also, the capacitor voltages of all SMs of the upper-arm travel together with minimal deviations from each other. The same is true for those of the lower-arm, too, which demonstrate the effectiveness of the proposed MPC switching algorithm in capacitor voltage balancing.

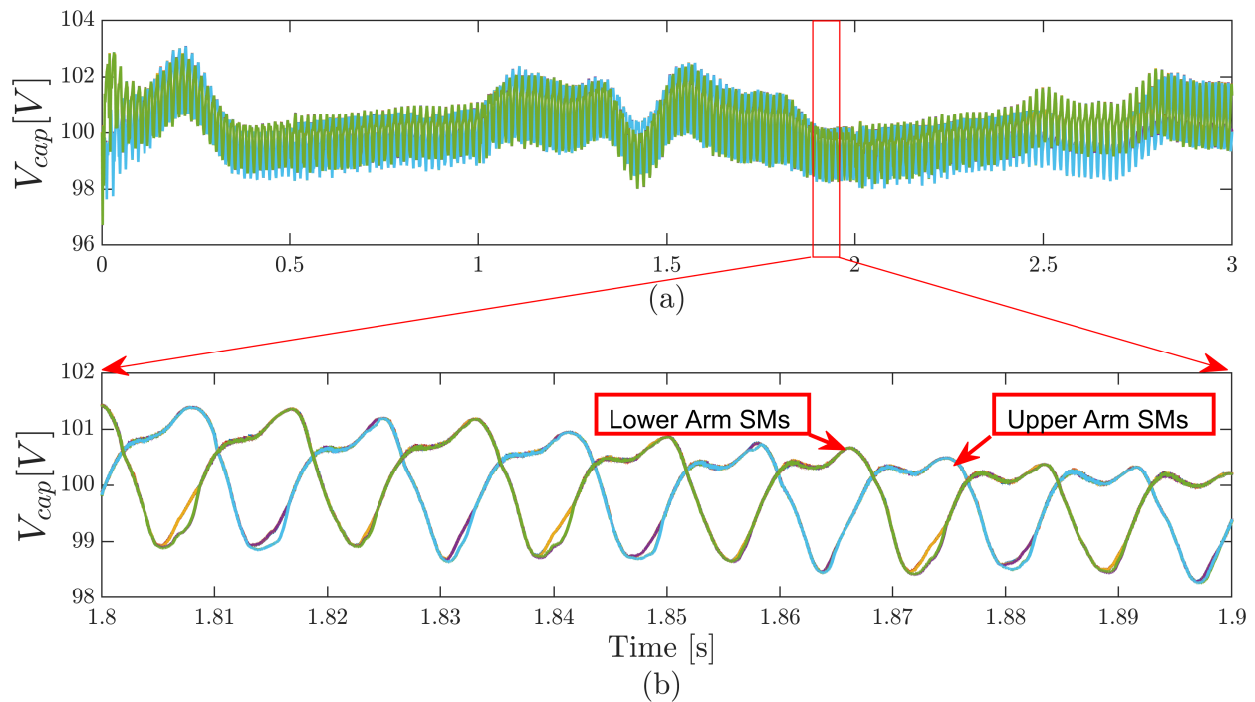


Figure 5.13 (a) Phase A upper and lower arms SMs voltage with i_z control and (b) a zoom on phase A upper and lower arms SMs voltage for $0.1s$

Figure 5.14 depicts the AC output current of phase A, as shown this current is balanced and tracked its reference during the whole simulation time, with a very low total harmonic distortion even under all operation conditions.

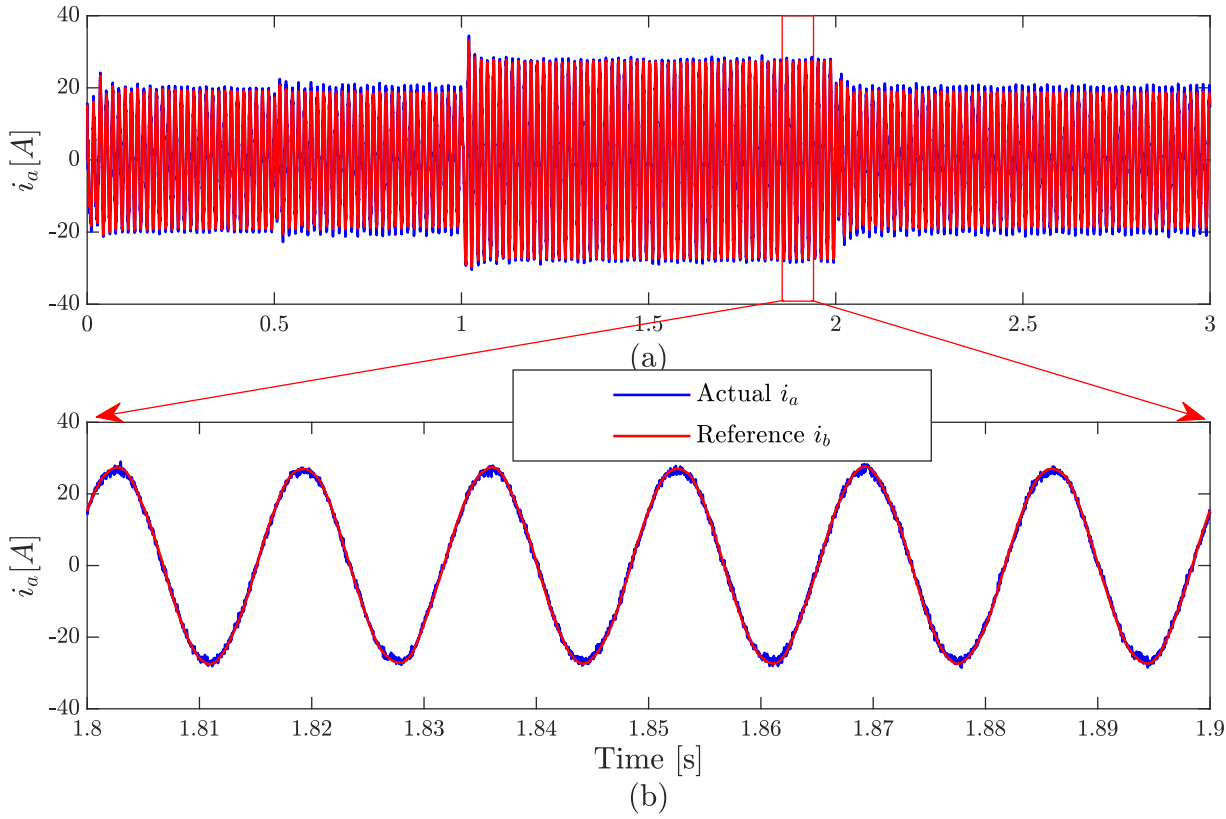


Figure 5.14 (a) Phase A AC output current tracking for the whole simulation time 3s and (b) a zoom on Phase A AC output current tracking for 0.1s showing the actual current i_a and the reference current i_b

Figure 5.15 illustrates the circulating current of phase A which is not forced to be zero all the time. Its controlled to balance the energy within the arms to make SM capacitor voltages of the upper- and lower-arms converge.

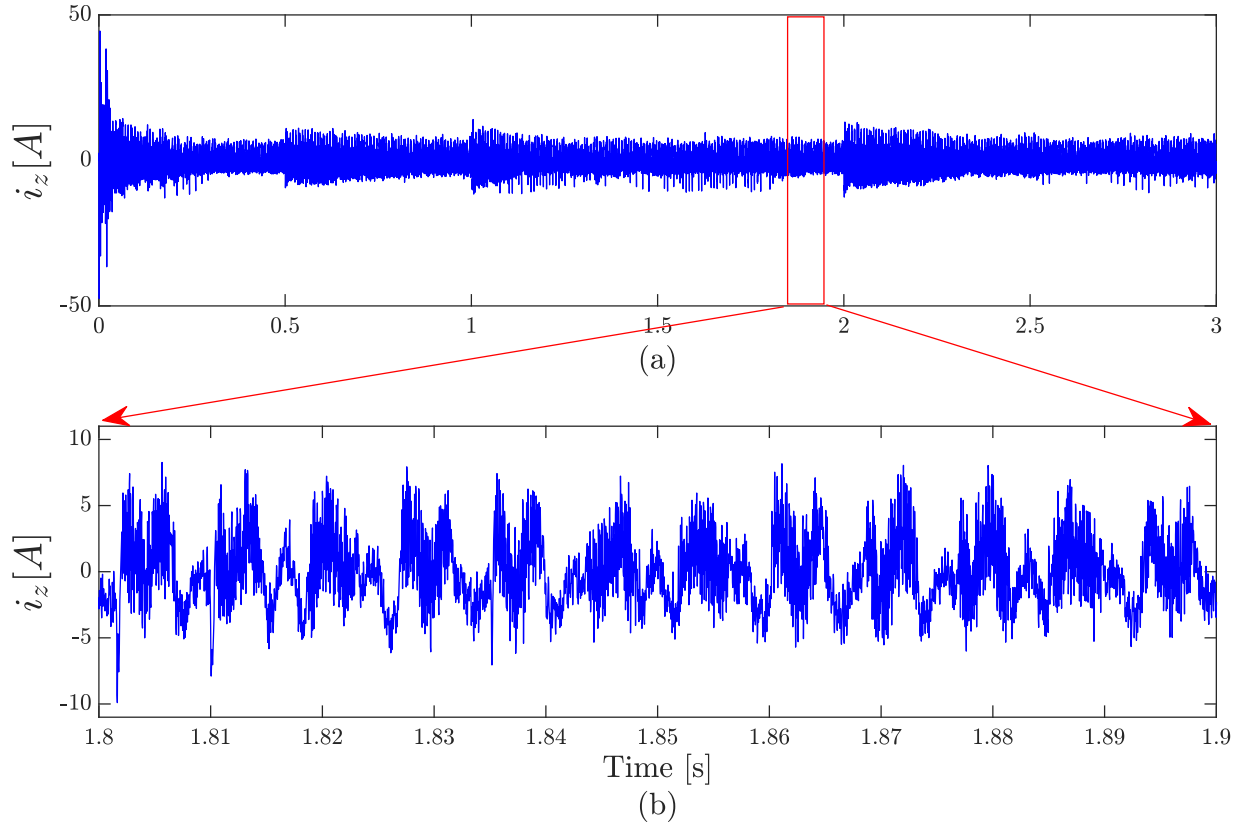


Figure 5.15 (a) Phase A circulating Current for the whole simulation time 3s and (b) a zoom on Phase A circulating Current for 0.1s

5.3.2.3 MMC Performance Without Circulating Current Control

In this case the the circulating current is forced to be zero, which led divergence in the SM capacitor voltages of upper and lower arms, as shown in Figure 5.16. The upper and lower arms voltages are not travelling together and diverge since no there is no control over energy allocation between these arms.

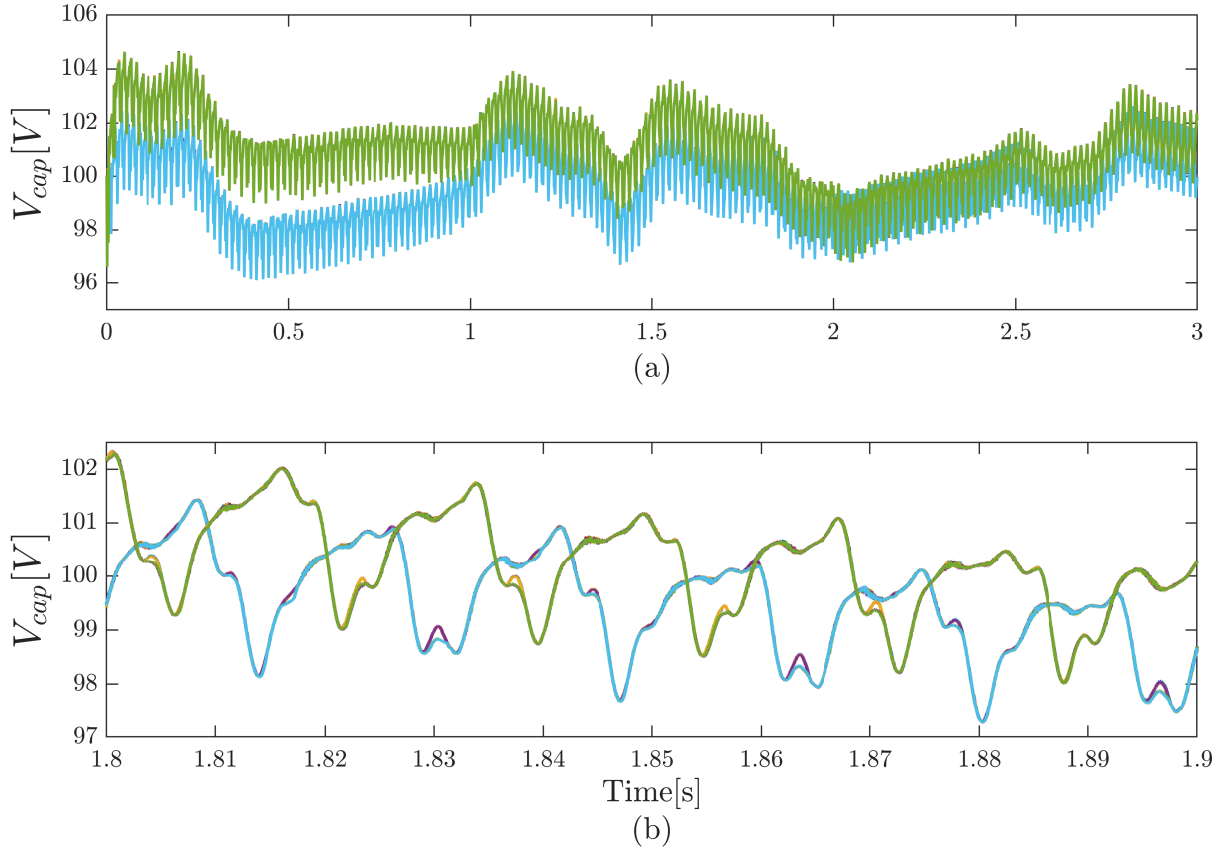


Figure 5.16 (a) Phase A upper and lower arms SMs voltage without i_z control and (b) a zoom on phase A upper and lower arms SMs voltage for 0.1s

5.3.2.4 BESS SOC Control

The flowchart in Figure 5.9, shows that the BESS charging/discharging operation is limited within a 10 – 90% SOC range. To test the control system when the SOC reaches the higher limit of 90%, the BESS initial SOC is set to 89.9996% near the upper limit. Figure 5.17 depicts the BESS operation parameters for grid demand load following support. Since the initial SOC is close to the upper SOC operation limit, any charging operation is controlled to zero when the SOC reaches 90%. Those limited operation areas are indicated by the dashed red rectangles at $t \in [0.8s, 1.4s]$

and $t \in [2.35s, 3s]$ as indicated the BESS power is zero in these areas. While on the other hand for $t \in [0s, 0.8s]$ and $t \in [0s, 0.8s]$, the BESS has a normal charging/discharging operation depending on the grid reference power.

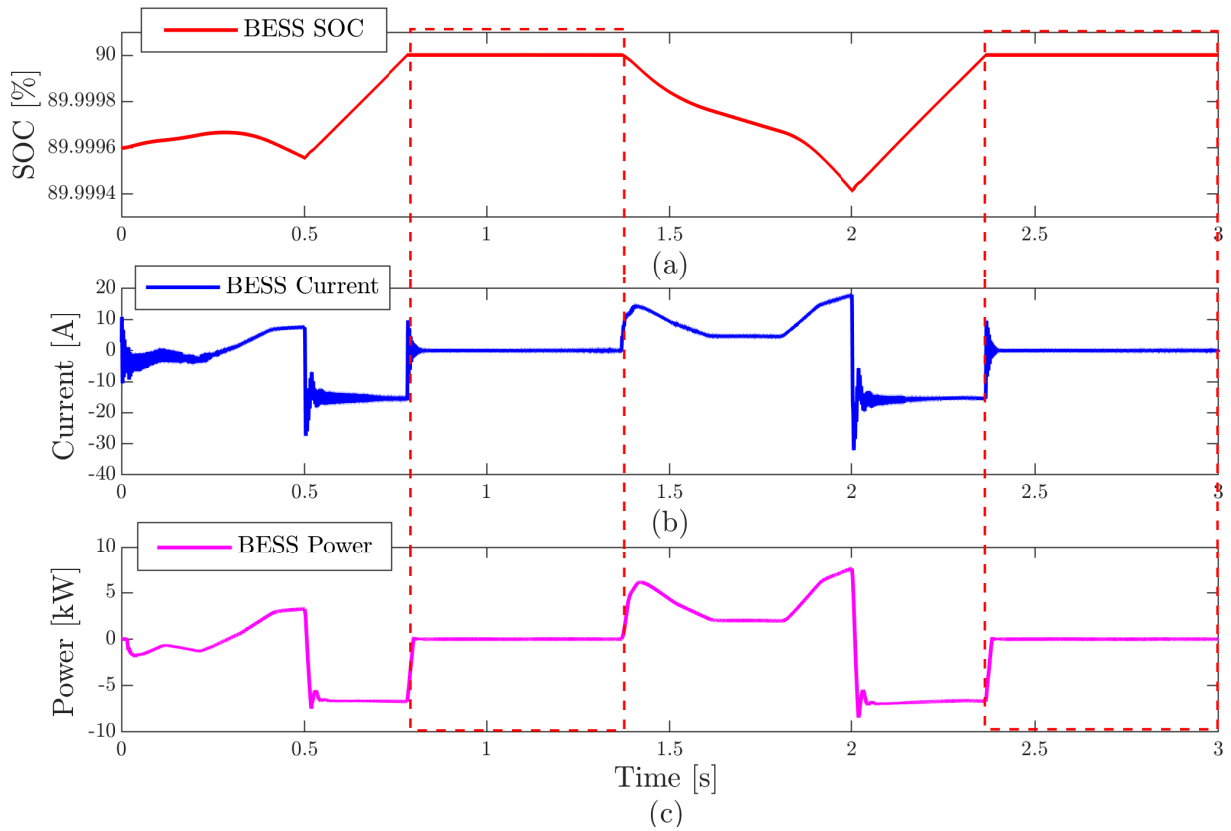


Figure 5.17 BESS parameters when it is SOC reached 90%, (a) BESS state of charge (SOC), (b) BESS charging/discharging current and (c) the BESS charging/discharging power

On the contrary, Figure 5.18 shows the BESS operation parameters when the BESS initial SOC is close to the lower SOC operation limit. To test this control system the BESS initial SOC is set to 10%. Hence, any discharging operation is controlled to stop when the SOC reaches 10%. At $t \in [0.45s, 0.55s]$ and $t \in [1.8s, 2.1s]$, the BESS current is controlled to zero to prevent discharging

operation. These limited operation areas are shown by the two dashed rectangles. while during other times of the simulation the BESS has a normal charging/discharging operation.

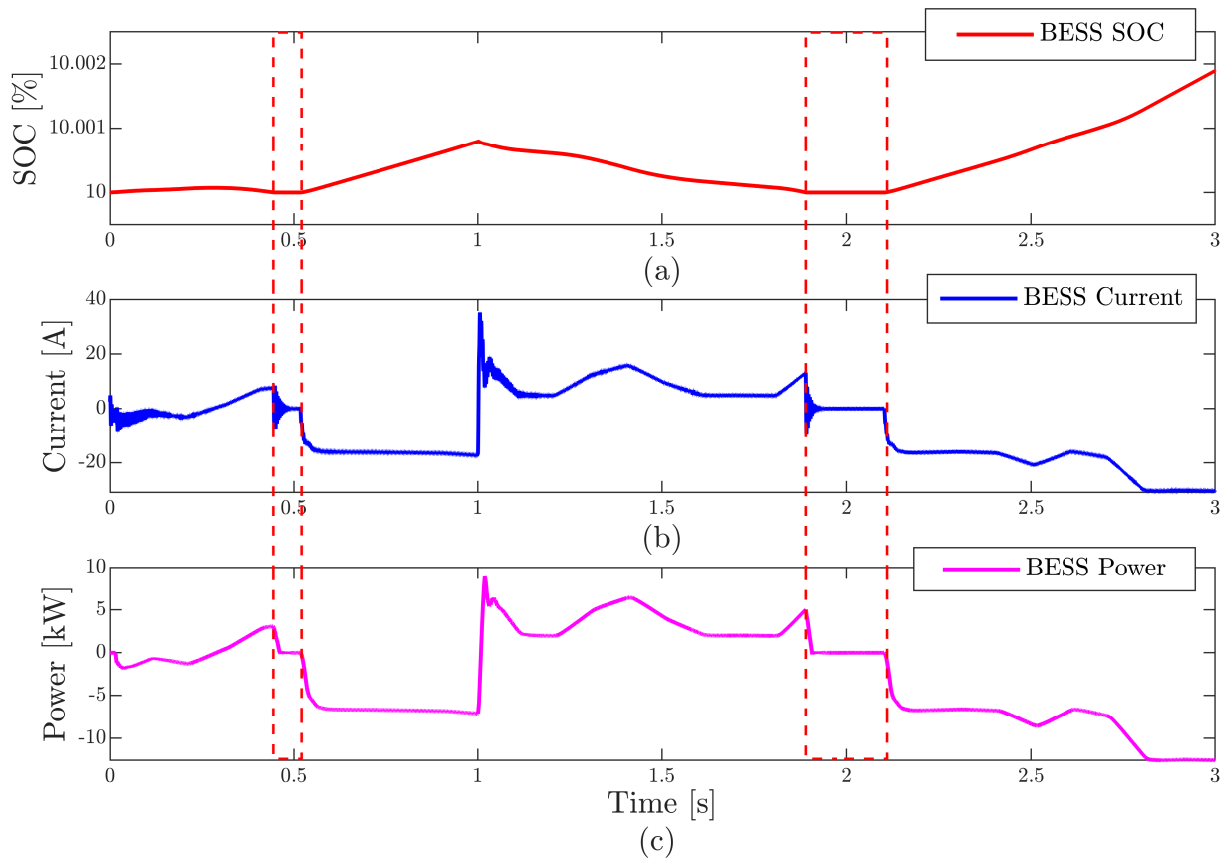


Figure 5.18 BESS parameters when it is SOC reached 10%, (a) BESS state of charge (SOC), (b) BESS charging/discharging current and (c) the BESS charging/discharging power

5.3.3 Case 2: PV-BESS for Load Following and Frequency support

The BESS control is designed to perform frequency control through virtual inertia and virtual damping is illustrated in Figure 5.8. It is assumed that the PV-BESS provides some frequency support in response to the frequency deviation at the terminal of the FBMMC, but its individual

contribution is not enough to significantly change the system frequency. In this case study, the virtual inertia coefficient M is equal to $1/2\pi s$ and the virtual damping coefficient D is equal to $1pu$. Figure 5.19 illustrates the input frequency deviation Δf_g^{pu} . Its obtained from a virtual synchronous generator system with a 60 Hz reference frequency f_g^{ref} and then a 40% step-up load change is applied at $1.2s$.

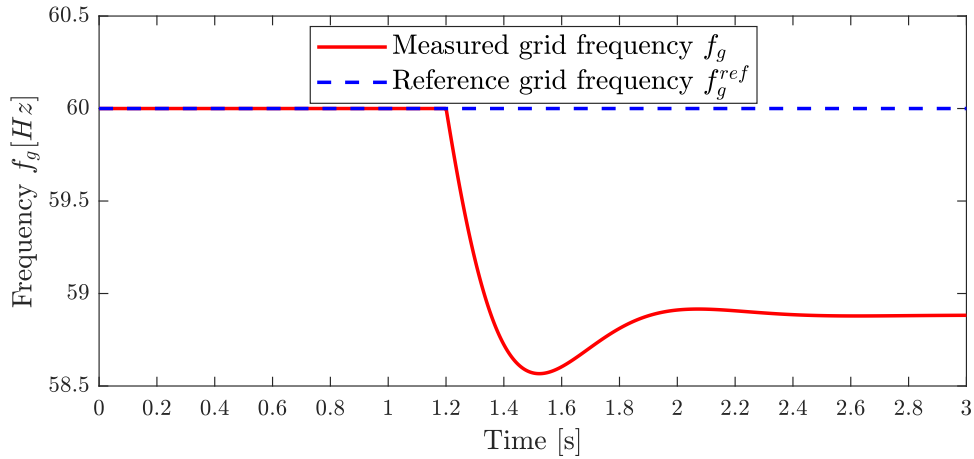


Figure 5.19 Grid frequency under a 40% step-up load change and reference frequency

5.3.3.1 FBMMC Power Control

Figure 5.20 demonstrates the performance of the system with a grid demand load similar to Case 1. The MMC output power P_g tracks its reference P_{in} and varies in proportion to the grid demand and grid frequency deviation. For $t \in [0s, 1.2s]$ the BESS has an output power similar to case 1. However, when the frequency deviation happens at $1.2s$, the frequency control system is activated with a power contribution of P_f . This can be seen from the spike in the BESS power at

$t = 1.2s$, which represents the frequency control power contribution and the grid demand following power contribution at that time.

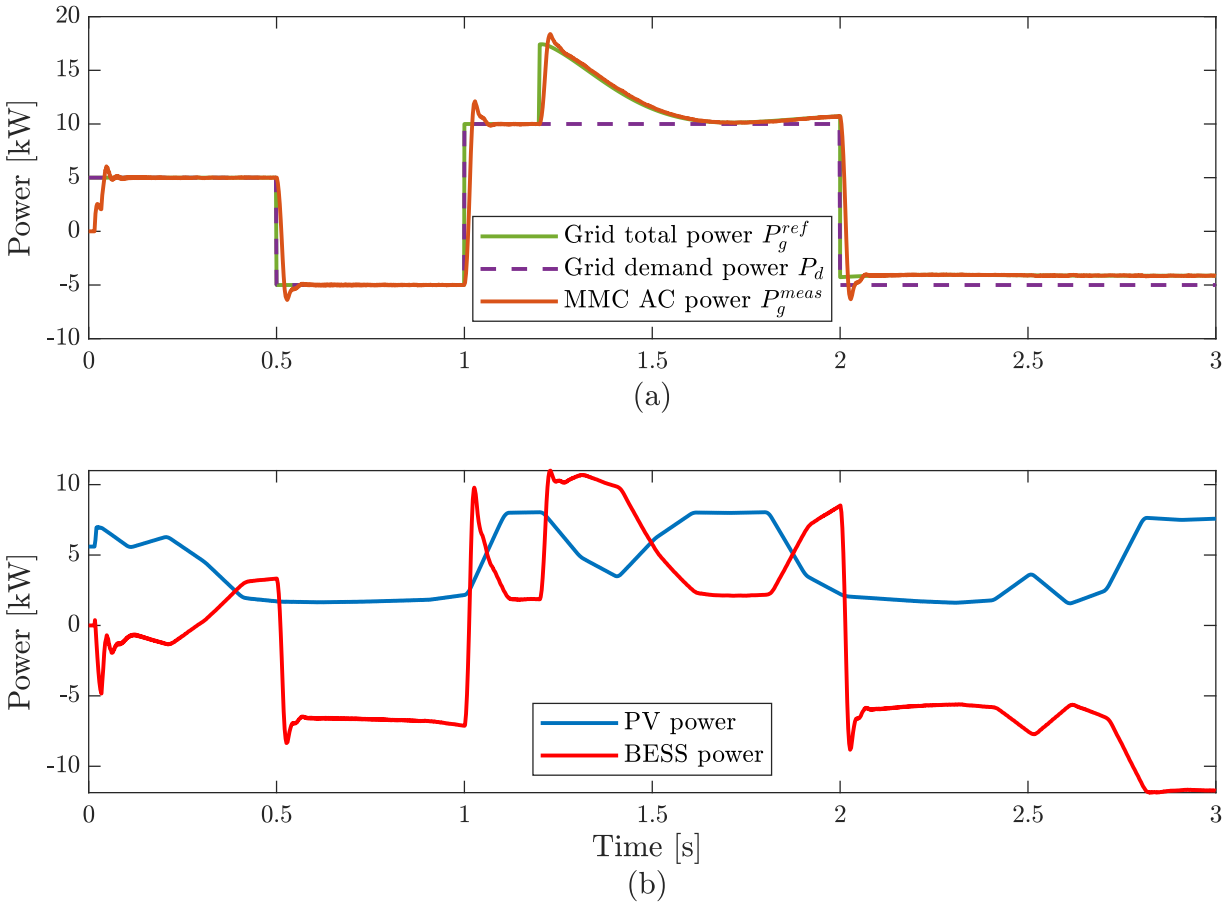


Figure 5.20 (a) Grid total power demand, grid power for demand following (case1) and the MMC output power to the grid and (b) the distributed PV system output power and the BESS power for grid demand following support

The BESS frequency control contribution, as inertia power and damping power, can be seen in Figure 5.21. The BESS power contribution for grid demand following P_d is illustrated with the blue curve, which is identical to the BESS output power of case 1. The frequency control power

contribution P_f is shown with the orange curve. It is zero until $1.2s$ but after that there a power discharge to the grid. This proves the control system effectiveness as it varies with system frequency. Their summation, which is the BESS power charging/discharging from the grid is illustrated with the yellow curve, where the maximum power discharge of $10.55kW$ happened at $1.32s$.

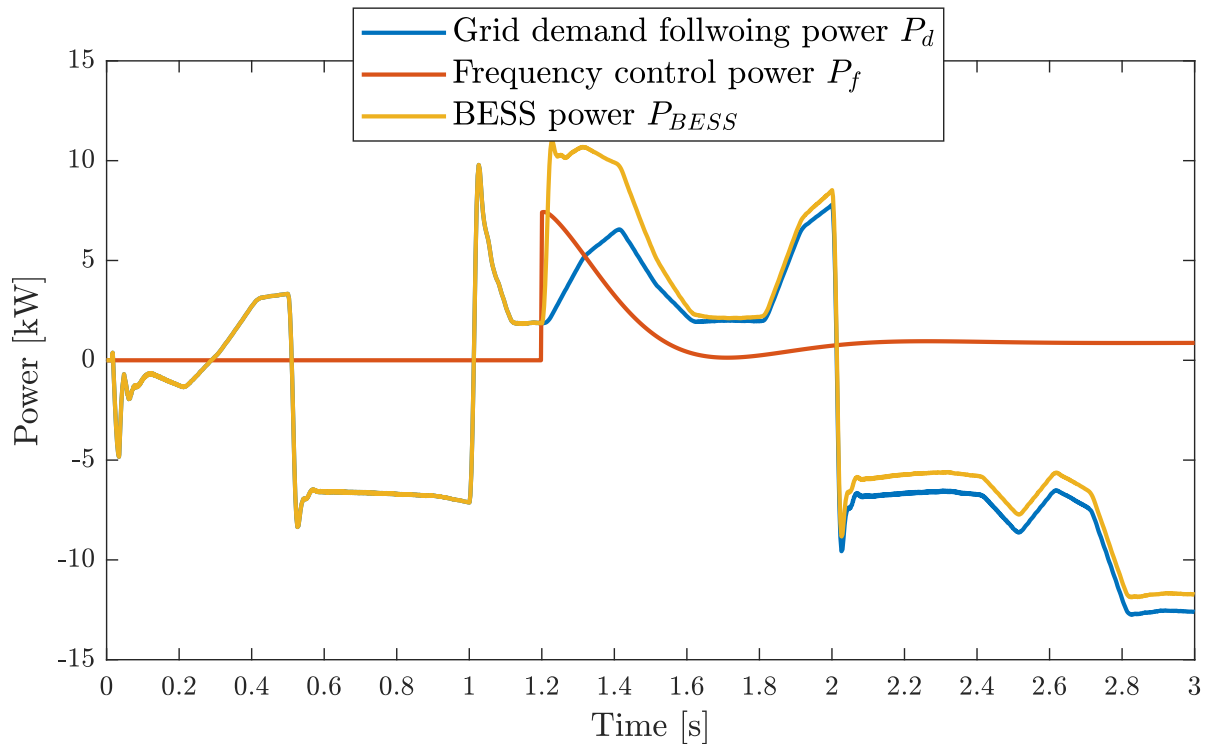


Figure 5.21 BESS power contribution to grid demand following and frequency control

Figure 5.22 compares the BESS parameters in case 1 and case 2. The BESS SOC is identical for both cases until $1.2s$. When the frequency deviation happens, the SOC for case 2 gets lower since more BESS power is discharged to support the frequency control. The BESS current is also identical for both case 1 and case 2 until $1.2s$. However, the BESS current has a spike for the curve

the represent the system when it is performing frequency control. This high current discharge is the frequency control power discharged to the grid.

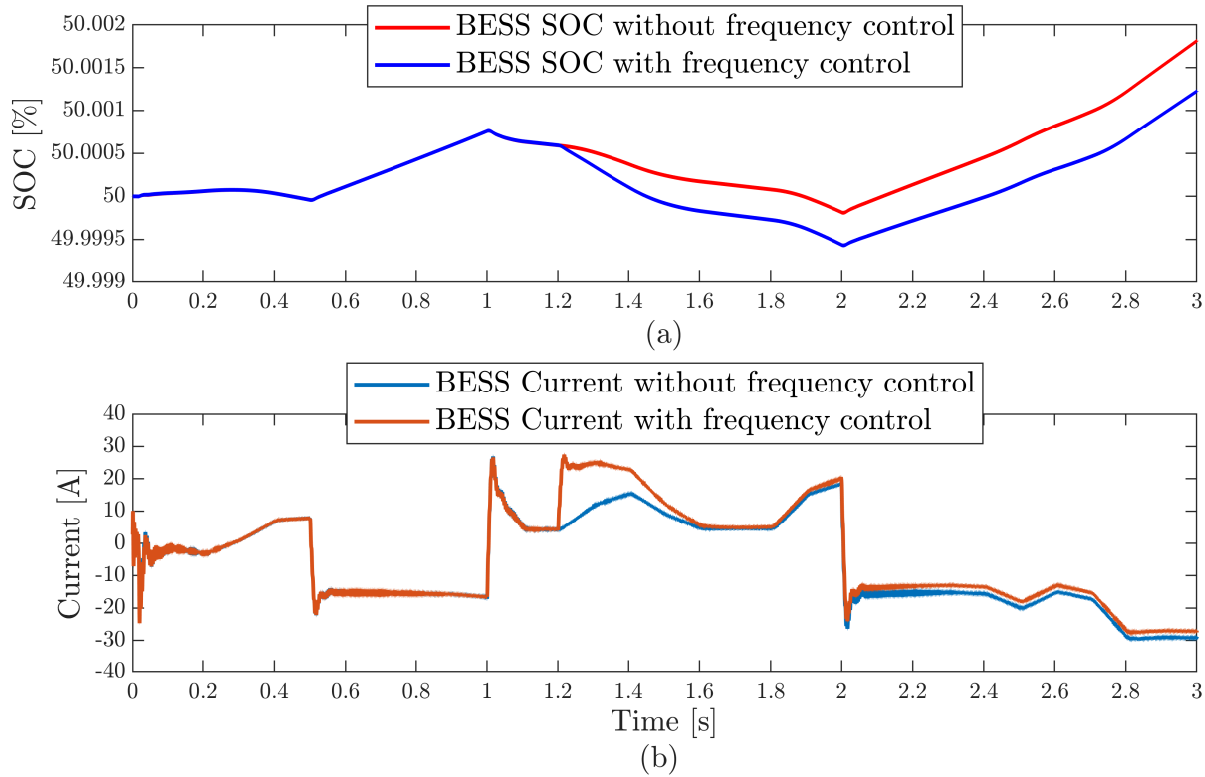


Figure 5.22 BESS Parameters when it is used for grid demand following and frequency control support, (a) BESS state of charge (SOC) with and without frequency support and (b) BESS charging/discharging current with and without frequency support

5.3.3.2 MMC Performance With Circulating Current Control

In this case study, the system experienced a fluctuated PV output power, variable grid demand, and frequency deviation during the simulation time. Despite all these changes, the MPC

control objectives are fulfilled. As shown in Figure 5.23 phase A upper and lower arms capacitor voltages are travelling together and regulated within less than $\pm 3\%$ of their nominal voltage. Figure 5.24 shows the AC output current of phase A, it is balanced, and tracking its reference the whole simulation time. Phase A circulating current is minimized as illustrated in Figure 5.25.

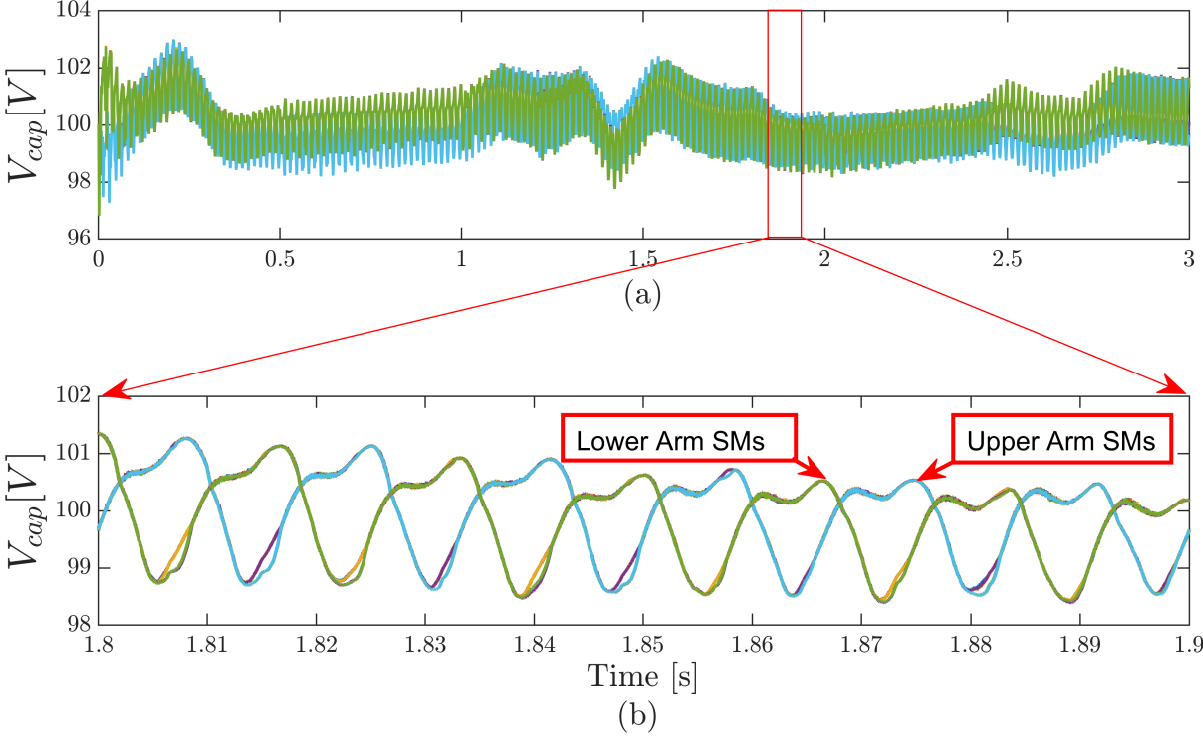


Figure 5.23 (a) Phase A upper and lower arms SMs voltage for the whole simulation time 3s and (b) a zoom on phase A upper and lower arms SMs voltage for 0.1s

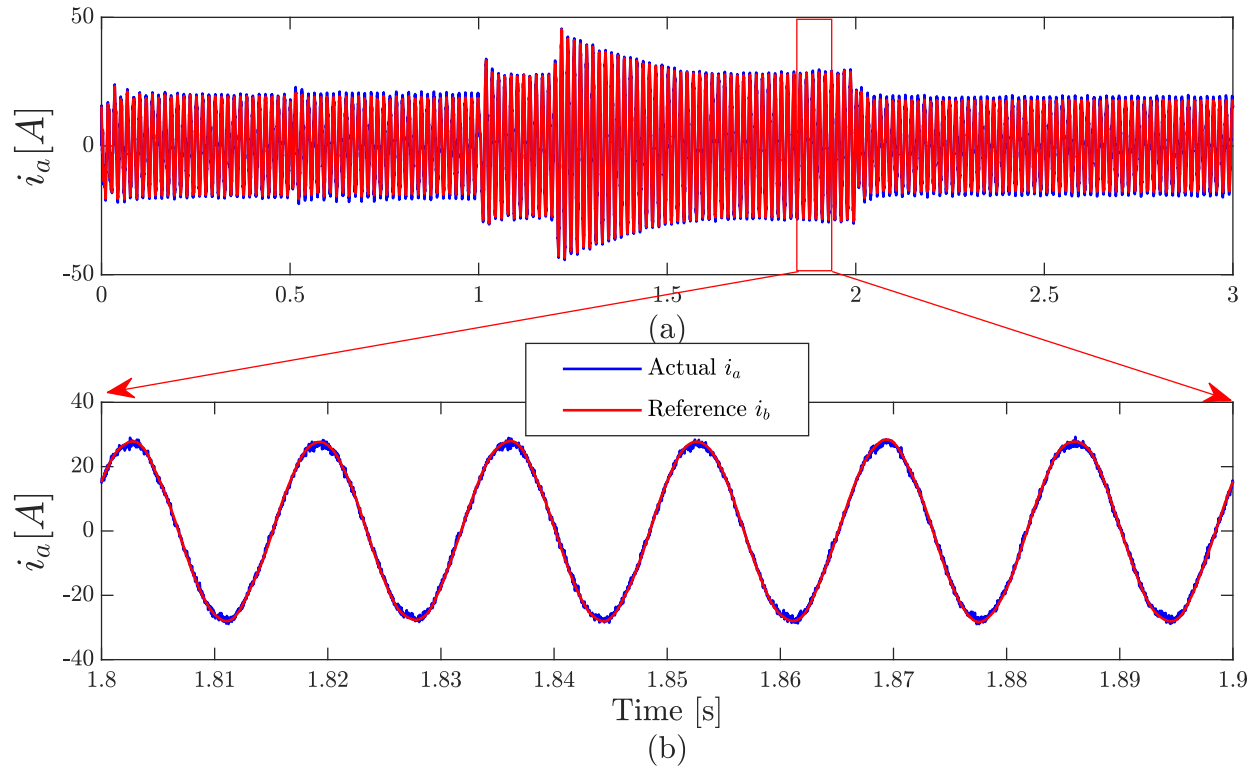


Figure 5.24 (a) Phase A AC output current tracking for the whole simulation time 3s and (b) a zoom on Phase A AC output current tracking for 0.1s showing the actual current i_a and the reference current i_b

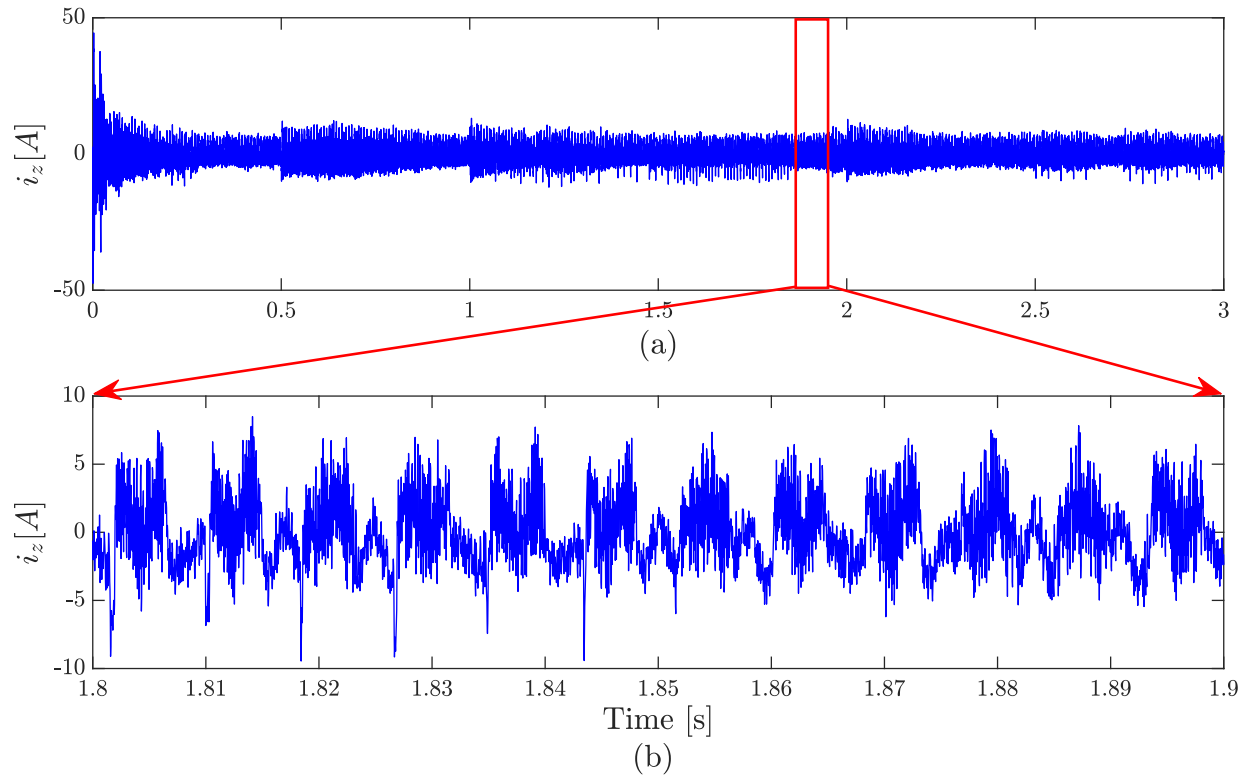


Figure 5.25 (a) Phase A circulating current for the whole simulation time 3s and (b) a zoom on Phase A circulating Current for 0.1s

CHAPTER 6

CONCLUSIONS AND FUTURE WORKS

6.1 Conclusions

Modular multilevel converters (MMC) are expected to play a significant role in the future of medium and high voltage networks applications. This thesis investigates the application of modular multilevel converters for solar photovoltaic (PV) and battery energy storage systems (BESS) integration to the power grid. This work can be concluded in two parts as follow.

First, this thesis proposes an MMC-based solution to interconnect PV systems through distributed maximum power point tracking (DMPPT). The proposed solution includes single PV modules connected to the HBSMs of the MMC through DC-DC converters to realize independent MPPT. A novel average SM capacitor voltage control algorithm is proposed to control power exchange between MMC and the AC power grid. A model predictive control (MPC) based switching algorithm is employed to obtain the best switching sequences of SMs. The results demonstrate that at any shading conditions, the proposed solution leads to capturing the maximum solar energy and achieves SM capacitor voltage balancing, AC current tracking, and circulating current suppression. Moreover, this work investigates the computation expenses of model predictive control (MPC) switching and the time elapsed to perform the SM sorting and SM selection process. The computation burden was evaluated in two computers with different processor properties and the results prove the effectiveness and robustness of the utilized advanced MPC switching.

Second, this thesis proposes a novel power electronics solution based on FBMMC to integrate BESS to PV systems. In this solution, the FBSMs are interfaced with single PV modules through a DC-DC converter to enable distributed MPPT. Effective switching of FBSM increases the range of voltage operation and control flexibility over the MMC DC-link, where the BESS is connected directly without the need for extra power electronics level to control it. The BESS is used to support the power grid, by following the grid demand load power. Moreover, this BESS is used to support the grid ancillary services and contribute to system stability by supporting load following and frequency control in the event of a disturbance. The simulation results verify the effectiveness of the proposed topology and its control systems.

6.2 Future Works

The future work recommendations of this thesis can be summarized in the following points.

First, the proposed FBMMC topology can be investigated for simultaneous connection of multiple distributed energy resources (DER) to the power grid through one MMC. For instance, each SM can be connected to a PV module and EV charger at the same time, while a BESS is connected to the DC-link of the MMC.

Second, the maximum level of controllability in the proposed FBMMC solution is not always required for grid connection of all types of DER, and an optimal combination of HBSM and FBSM could be used to minimize the design costs, volume and switching losses without any compromise in the MMC performance.

Third, to verify the effectiveness of the proposed topologies and their control design, hardware-in-the-loop (HIL) tests and a hardware prototype design are needed for real-world tests.

REFERENCES

- [1] P. Beiter, M. Elchinger, and T. Tian, “2016 renewable energy data book,” tech. rep., National Renewable Energy Lab.(NREL), Golden, CO (United States), 2017.
- [2] R. Secretariat, “Renewables 2017 global status report. ren21,” tech. rep., Paris, Tech. Rep, 2017.
- [3] G. Wang, M. Ciobotaru, and V. G. Agelidis, “Power smoothing of large solar pv plant using hybrid energy storage,” *IEEE Transactions on Sustainable Energy*, vol. 5, no. 3, pp. 834–842, 2014.
- [4] S. Rivera, B. Wu, R. Lizana, S. Kouro, M. Perez, and J. Rodriguez, “Modular multilevel converter for large-scale multistring photovoltaic energy conversion system,” in *2013 IEEE Energy Conversion Congress and Exposition*, pp. 1941–1946, IEEE, 2013.
- [5] F. Rong, X. Gong, and S. Huang, “A novel grid-connected pv system based on mmc to get the maximum power under partial shading conditions,” *IEEE Transactions on Power Electronics*, vol. 32, no. 6, pp. 4320–4333, 2016.
- [6] J. Khazaei, G. Pavlak, B. Lee, and M. Elsenbaty, “A novel application of modular multilevel converters for partially shaded pv systems,” in *2019 IEEE Texas Power and Energy Conference (TPEC)*, pp. 1–6, IEEE, 2019.
- [7] H. Nademi, A. Elahidoost, and L. E. Norum, “Comparative analysis of different mppt schemes for photovoltaic integration of modular multilevel converter,” in *2016 IEEE 17th Workshop on Control and Modeling for Power Electronics (COMPEL)*, pp. 1–5, IEEE, 2016.
- [8] J. Mei, B. Xiao, K. Shen, L. M. Tolbert, and J. Y. Zheng, “Modular multilevel inverter with new modulation method and its application to photovoltaic grid-connected generator,” *IEEE Transactions on Power Electronics*, vol. 28, no. 11, pp. 5063–5073, 2013.
- [9] S. Rajasekar and R. Gupta, “Solar photovoltaic power conversion using modular multilevel converter,” in *2012 Students Conference on Engineering and Systems*, pp. 1–6, IEEE, 2012.
- [10] A. B. Acharya, M. Ricco, D. Sera, R. Teodorescu, and L. E. Norum, “Performance analysis of medium-voltage grid integration of pv plant using modular multilevel converter,” *IEEE Transactions on Energy Conversion*, vol. 34, no. 4, pp. 1731–1740, 2019.

- [11] C. Deline, B. Marion, J. Granata, and S. Gonzalez, “Performance and economic analysis of distributed power electronics in photovoltaic systems,” tech. rep., National Renewable Energy Lab.(NREL), Golden, CO (United States), 2011.
- [12] Y. Moumouni, Y. Baghzouz, and R. F. Boehm, “Power “smoothing” of a commercial-size photovoltaic system by an energy storage system,” in *2014 16th International Conference on Harmonics and Quality of Power (ICHQP)*, pp. 640–644, IEEE, 2014.
- [13] G. Ari and Y. Baghzouz, “Impact of high pv penetration on voltage regulation in electrical distribution systems,” in *2011 International Conference on Clean Electrical Power (ICCEP)*, pp. 744–748, IEEE, 2011.
- [14] V. R. Disfani, P. Ubiratan, and J. Kleissl, “Model predictive on-load tap changer control for high penetrations of pv using high resolution resources assessment with sky imager,” in *2016 IEEE Power and Energy Society General Meeting (PESGM)*, pp. 1–5, IEEE, 2016.
- [15] V. R. Disfani, L. Fan, Z. Miao, and Y. Ma, “Fast model predictive control algorithms for fast-switching modular multilevel converters,” *Electric Power Systems Research*, vol. 129, pp. 105–113, 2015.
- [16] S. S. Williamson, A. K. Rathore, and F. Musavi, “Industrial electronics for electric transportation: Current state-of-the-art and future challenges,” *IEEE Transactions on Industrial Electronics*, vol. 62, no. 5, pp. 3021–3032, 2015.
- [17] H. Abu-Rub, M. Malinowski, and K. Al-Haddad, *Power electronics for renewable energy systems, transportation and industrial applications*. John Wiley & Sons, 2014.
- [18] B. Bilgin, P. Magne, P. Malysz, Y. Yang, V. Pantelic, M. Preindl, A. Korobkine, W. Jiang, M. Lawford, and A. Emadi, “Making the case for electrified transportation,” *IEEE Transactions on Transportation Electrification*, vol. 1, no. 1, pp. 4–17, 2015.
- [19] R. Krishnan, *Electric motor drives: modeling, analysis and control*. Prentice Hall, 2001.
- [20] K. Sharifabadi, L. Harnefors, H.-P. Nee, S. Norrga, and R. Teodorescu, *Design, control, and application of modular multilevel converters for HVDC transmission systems*. John Wiley & Sons, 2016.
- [21] K. Friedrich, “Modern hvdc plus application of vsc in modular multilevel converter topology,” in *2010 IEEE International Symposium on Industrial Electronics*, pp. 3807–3810, IEEE, 2010.
- [22] M. Saeedifard and R. Iravani, “Dynamic performance of a modular multilevel back-to-back hvdc system,” *IEEE Transactions on power delivery*, vol. 25, no. 4, pp. 2903–2912, 2010.
- [23] I. Abdalla, J. Corda, and L. Zhang, “Multilevel dc-link inverter and control algorithm to overcome the pv partial shading,” *IEEE Transactions on Power Electronics*, vol. 28, no. 1, pp. 14–18, 2012.

- [24] T. Soong and P. W. Lehn, "Evaluation of emerging modular multilevel converters for bess applications," *IEEE Transactions on Power Delivery*, vol. 29, no. 5, pp. 2086–2094, 2014.
- [25] M. Vasiladiotis and A. Rufer, "Analysis and control of modular multilevel converters with integrated battery energy storage," *IEEE Transactions on Power Electronics*, vol. 30, no. 1, pp. 163–175, 2014.
- [26] Q. Song, W. Liu, X. Li, H. Rao, S. Xu, and L. Li, "A steady-state analysis method for a modular multilevel converter," *IEEE Transactions on Power electronics*, vol. 28, no. 8, pp. 3702–3713, 2012.
- [27] M. Alsadah and F. Mancilla-David, "Modeling and control of grid-connected photovoltaic power plants utilizing a simplified model of the modular multilevel converter," in *2014 North American Power Symposium (NAPS)*, pp. 1–6, IEEE, 2014.
- [28] M. Glinka and R. Marquardt, "A new ac/ac-multilevel converter family applied to a single-phase converter," in *The Fifth International Conference on Power Electronics and Drive Systems, 2003. PEDS 2003.*, vol. 1, pp. 16–23, IEEE, 2003.
- [29] M. Malinowski, K. Gopakumar, J. Rodriguez, and M. A. Perez, "A survey on cascaded multilevel inverters," *IEEE Transactions on industrial electronics*, vol. 57, no. 7, pp. 2197–2206, 2009.
- [30] A. Alesina and M. Venturini, "Solid-state power conversion: A fourier analysis approach to generalized transformer synthesis," *IEEE transactions on circuits and systems*, vol. 28, no. 4, pp. 319–330, 1981.
- [31] A. Nabae, I. Takahashi, and H. Akagi, "A new neutral-point-clamped pwm inverter," *IEEE Transactions on industry applications*, no. 5, pp. 518–523, 1981.
- [32] T. Meynard and H. Foch, "Multi-level conversion: high voltage choppers and voltage-source inverters," in *PESC'92 Record. 23rd Annual IEEE Power Electronics Specialists Conference*, pp. 397–403, IEEE, 1992.
- [33] T. A. Meynard, H. Foch, P. Thomas, J. Courault, R. Jakob, and M. Nahrstaedt, "Multicell converters: basic concepts and industry applications," *IEEE transactions on industrial electronics*, vol. 49, no. 5, pp. 955–964, 2002.
- [34] P. Barbosa, P. Steimer, J. Steinke, M. Winkelkemper, and N. Celanovic, "Active-neutral-point-clamped (anpc) multilevel converter technology," in *2005 European Conference on Power Electronics and Applications*, pp. 10–pp, IEEE, 2005.
- [35] P. W. Hammond, "A new approach to enhance power quality for medium voltage ac drives," *IEEE Transactions on Industry Applications*, vol. 33, no. 1, pp. 202–208, 1997.

- [36] A. Lesnicar and R. Marquardt, "An innovative modular multilevel converter topology suitable for a wide power range," in *2003 IEEE Bologna Power Tech Conference Proceedings*, vol. 3, pp. 6–pp, IEEE, 2003.
- [37] S. Debnath, J. Qin, B. Bahrani, M. Saeedifard, and P. Barbosa, "Operation, control, and applications of the modular multilevel converter: A review," *IEEE transactions on power electronics*, vol. 30, no. 1, pp. 37–53, 2014.
- [38] R. Marquardt, "Modular multilevel converters: State of the art and future progress," *IEEE Power Electronics Magazine*, vol. 5, no. 4, pp. 24–31, 2018.
- [39] J. Qin and M. Saeedifard, "Predictive control of a modular multilevel converter for a back-to-back hvdc system," *IEEE Transactions on Power delivery*, vol. 27, no. 3, pp. 1538–1547, 2012.
- [40] S. Khanal and V. Disfani, "A novel optimal modulation strategy for modular multilevel converter based hvdc systems," in *2019 International Conference on Renewable Energy and Power Engineering (REPE)*, pp. 10–14, IEEE, 2019.
- [41] S. Khanal and V. Disfani, "Reduced switching-frequency modulation design for model predictive control based modular multilevel converters," in *2019 International Conference on Renewable Energy and Power Engineering (REPE)*, pp. 1–5, IEEE, 2019.
- [42] J. Echeverria, S. Kouro, M. Perez, and H. Abu-Rub, "Multi-modular cascaded dc-dc converter for hvdc grid connection of large-scale photovoltaic power systems," in *IECON 2013-39th Annual Conference of the IEEE Industrial Electronics Society*, pp. 6999–7005, IEEE, 2013.
- [43] B. N. Alajmi, K. H. Ahmed, G. P. Adam, S. J. Finney, and B. W. Williams, "Modular multilevel inverter with maximum power point tracking for grid connected photovoltaic application," in *2011 IEEE International Symposium on Industrial Electronics*, pp. 2057–2062, IEEE, 2011.
- [44] G. Ramya and R. Ramaprabha, "Design methodology of p-res controllers with harmonic compensation technique for modular multilevel converter fed from partially shaded pv array," in *2015 IEEE 11th International Conference on Power Electronics and Drive Systems*, pp. 330–335, IEEE, 2015.
- [45] G. Ramya and R. Ramaprabha, "Switching loss and thd analysis of modular multilevel converter with different switching frequency," in *2015 IEEE 11th International Conference on Power Electronics and Drive Systems*, pp. 336–340, IEEE, 2015.
- [46] L. Baruschka and A. Mertens, "Comparison of cascaded h-bridge and modular multilevel converters for bess application," in *2011 IEEE Energy Conversion Congress and Exposition*, pp. 909–916, IEEE, 2011.

- [47] N. Mukherjee and D. Strickland, "Analysis and comparative study of different converter modes in modular second-life hybrid battery energy storage systems," *IEEE Journal of Emerging and Selected Topics in Power Electronics*, vol. 4, no. 2, pp. 547–563, 2015.
- [48] N. Kawakami, S. Ota, H. Kon, S. Konno, H. Akagi, H. Kobayashi, and N. Okada, "Development of a 500-kw modular multilevel cascade converter for battery energy storage systems," *IEEE Transactions on Industry Applications*, vol. 50, no. 6, pp. 3902–3910, 2014.
- [49] A. Hillers and J. Biela, "Optimal design of the modular multilevel converter for an energy storage system based on split batteries," in *2013 15th European Conference on Power Electronics and Applications (EPE)*, pp. 1–11, IEEE, 2013.
- [50] W. Zeng, R. Li, and X. Cai, "A new hybrid modular multilevel converter with integrated energy storage," *IEEE Access*, vol. 7, pp. 172981–172993, 2019.
- [51] H. Kim, B. Parkhideh, T. D. Bongers, and H. Gao, "Reconfigurable solar converter: A single-stage power conversion pv-battery system," *IEEE transactions on power electronics*, vol. 28, no. 8, pp. 3788–3797, 2012.
- [52] H. Bayat and A. Yazdani, "A hybrid mmc-based photovoltaic and battery energy storage system," *IEEE Power and Energy Technology Systems Journal*, vol. 6, no. 1, pp. 32–40, 2019.
- [53] U. Sohail, H. Nademi, and L. E. Norum, "A reliable modular based pv-battery hybrid system with peak shaving capability," in *2018 IEEE 19th Workshop on Control and Modeling for Power Electronics (COMPEL)*, pp. 1–6, IEEE, 2018.
- [54] L. Zhang, Z. Zhang, J. Qin, D. Shi, and Z. Wang, "Design and performance evaluation of the modular multilevel converter (mmc)-based grid-tied pv-battery conversion system," in *2018 IEEE Energy Conversion Congress and Exposition (ECCE)*, pp. 2649–2654, IEEE, 2018.
- [55] G. Adam, S. Finney, and B. Williams, "Enhanced control strategy of full-bridge modular multilevel converter," in *2015 International Conference on Renewable Energy Research and Applications (ICRERA)*, pp. 1432–1436, 2015.
- [56] G. P. Adam, S. Finney, B. Williams, I. E. Davidson, and A. Y. M. Abbas, "Full-bridge modular multilevel converter (fb-mmc) with extended control range," in *AFRICON 2015*, pp. 1–5, IEEE, 2015.
- [57] G. P. Adam and I. E. Davidson, "Robust and generic control of full-bridge modular multilevel converter high-voltage dc transmission systems," *IEEE Transactions on Power Delivery*, vol. 30, no. 6, pp. 2468–2476, 2015.
- [58] S. Khanal and V. Disfani, "Modular multilevel converter design for grid integration of solar photovoltaic systems," in *2020 IEEE Power Energy Society General Meeting (PESGM)*, pp. 1–5, 2020.

- [59] K. Wang, Y. Li, and Z. Zheng, "Voltage balancing control and experiments of a novel modular multilevel converter," in *2010 IEEE Energy Conversion Congress and Exposition*, pp. 3691–3696, IEEE, 2010.
- [60] U. N. Gnanarathna, A. M. Gole, and R. P. Jayasinghe, "Efficient modeling of modular multi-level hvdc converters (mmc) on electromagnetic transient simulation programs," *IEEE Transactions on power delivery*, vol. 26, no. 1, pp. 316–324, 2010.
- [61] S. Kouro, M. Malinowski, K. Gopakumar, J. Pou, L. G. Franquelo, B. Wu, J. Rodriguez, M. A. Pérez, and J. I. Leon, "Recent advances and industrial applications of multilevel converters," *IEEE Transactions on industrial electronics*, vol. 57, no. 8, pp. 2553–2580, 2010.
- [62] M. Glinka and R. Marquardt, "A new ac/ac multilevel converter family," *IEEE Transactions on Industrial Electronics*, vol. 52, no. 3, pp. 662–669, 2005.
- [63] J. Rodriguez and P. Cortes, *Predictive control of power converters and electrical drives*, vol. 40. John Wiley & Sons, 2012.
- [64] J. Rodriguez, J. Pontt, C. A. Silva, P. Correa, P. Lezana, P. Cortés, and U. Ammann, "Predictive current control of a voltage source inverter," *IEEE transactions on industrial electronics*, vol. 54, no. 1, pp. 495–503, 2007.
- [65] S. Khanal, "Optimal modulation and topology design of modular multilevel converter for grid integration of solar photovoltaic systems," Master's thesis, University of Tennessee at Chattanooga, 2019.
- [66] F. Mohamed, S. Wasti, S. Afshar, P. Macedo, and V. Disfani, "Mmc-based distributed maximum power point tracking for photovoltaic systems," in *2020 IEEE Power & Energy Society General Meeting (PESGM)*, pp. 1–5, IEEE, 2020.
- [67] F. Mohamed, S. Wasti, S. Afshar, P. Macedo, and V. Disfani, "Mmc-based distributed maximum power point tracking for photovoltaic systems," *arXiv preprint arXiv:2002.12919*, 2020.
- [68] S. B. Kjaer, J. K. Pedersen, and F. Blaabjerg, "A review of single-phase grid-connected inverters for photovoltaic modules," *IEEE transactions on industry applications*, vol. 41, no. 5, pp. 1292–1306, 2005.
- [69] A. K. Abdelsalam, A. M. Massoud, S. Ahmed, and P. N. Enjeti, "High-performance adaptive perturb and observe mppt technique for photovoltaic-based microgrids," *IEEE Transactions on Power Electronics*, vol. 26, no. 4, pp. 1010–1021, 2011.
- [70] M. A. G. De Brito, L. Galotto, L. P. Sampaio, G. d. A. e Melo, and C. A. Canesin, "Evaluation of the main mppt techniques for photovoltaic applications," *IEEE transactions on industrial electronics*, vol. 60, no. 3, pp. 1156–1167, 2012.

- [71] B. Subudhi and R. Pradhan, “A comparative study on maximum power point tracking techniques for photovoltaic power systems,” *IEEE transactions on Sustainable Energy*, vol. 4, no. 1, pp. 89–98, 2012.
- [72] J. Ahola, *DEE Photovoltaic Power Plant Weather Station Data*, 2018 (accessed Nov 3, 2019).
- [73] K. Divya and J. Østergaard, “Battery energy storage technology for power systems—an overview,” *Electric power systems research*, vol. 79, no. 4, pp. 511–520, 2009.
- [74] W. J. Cole and A. Frazier, “Cost projections for utility-scale battery storage,” tech. rep., National Renewable Energy Lab.(NREL), Golden, CO (United States), 2019.
- [75] C. D. Parker, “Lead–acid battery energy-storage systems for electricity supply networks,” *Journal of Power Sources*, vol. 100, no. 1-2, pp. 18–28, 2001.
- [76] Y. Ma, Z. Miao, V. R. Disfani, and L. Fan, “A one-step model predictive control for modular multilevel converters,” in *2014 IEEE PES General Meeting| Conference & Exposition*, pp. 1–5, IEEE, 2014.
- [77] A. Antonopoulos, L. Angquist, and H.-P. Nee, “On dynamics and voltage control of the modular multilevel converter,” in *2009 13th European Conference on Power Electronics and Applications*, pp. 1–10, IEEE, 2009.

APPENDIX A

PV Module Characteristic

Table A.1 shows the module data and the model parameters and of the PV module used in this thesis. All the parameters are given in standard testing condition (STC).

Table A.1 Solar PV module data and parameters

Parameter	value
Module	SunPower SPR-305E-WHT-D
Maximum Power	305.226 W
Cells per module	96
Open circuit voltage (V_{oc})	64.2 V
Short-circuit current (I_{sc})	5.96 A
Voltage at maximum power point (V_{MPP})	54.7 V
Current at maximum power point (I_{MPP})	5.58 A
Temperature coefficient of V_{oc}	-0.27269 %/C°
Temperature coefficient of I_{sc}	0.061745 %/C°
Light-generated I_L	6.0092 A
Diode Saturation current I_0	$6.3014e^{-12}$ A
Diode ideality factor	0.94504
Shunt resistance R_{sh}	269.5934 ohms
Series resistance R_s	0.37152 ohms

The I-V characteristics curve of the PV module is illustrated in Figure A.1(a), it shows the I-V characteristics at 25C° for different irradiance levels. While Figure A.1(b) shows the P-V characteristics curve of the PV module where the maximum power and maximum power point voltage are depicted for different irradiance levels

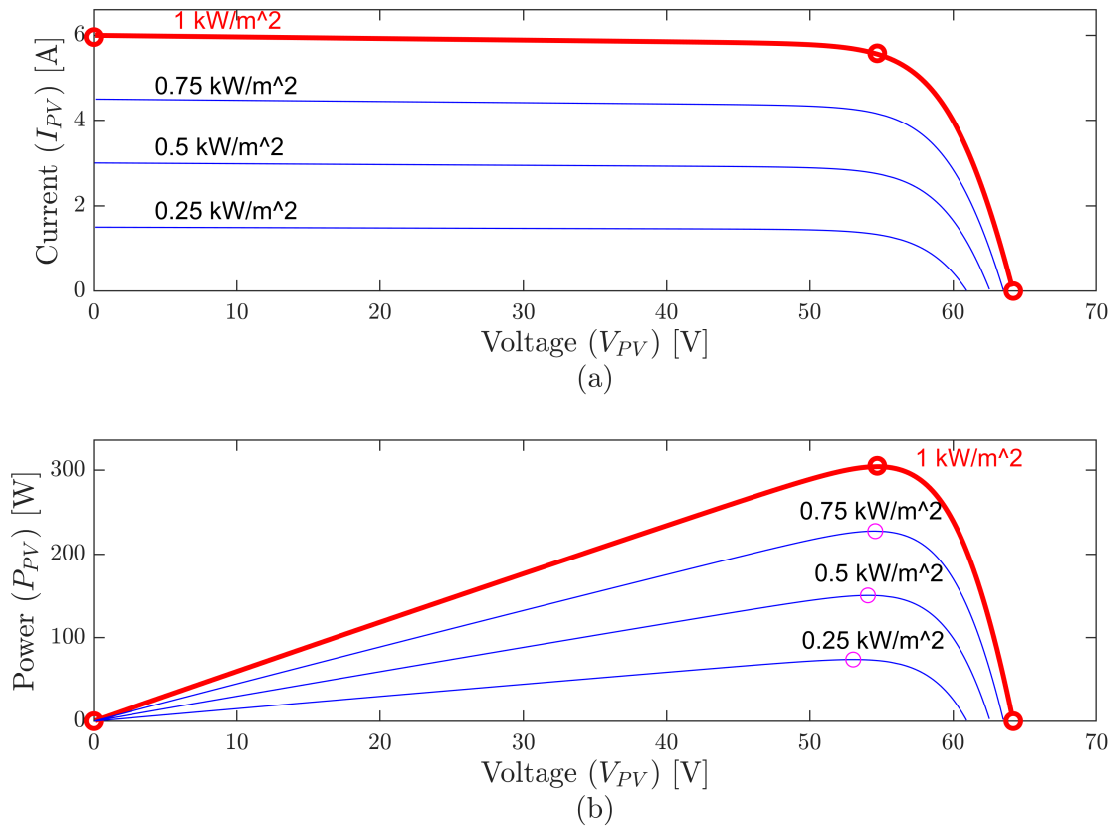


Figure A.1 (a) The I-V characteristics of SunPower SPR-305E-WHT-D PV module and (b) The P-V characteristics of SunPower SPR-305E-WHT-D PV module

APPENDIX B

BESS Model Characteristic

Table B.1 shows the Battery energy storage system (BESS) model parameters used in this thesis. The used BESS type is Lithium-Ion battery model.

Table B.1 BESS model Parameters

Parameter	Value
Type	Lithium-Ion
Cell rated capacity	5.4 Ah
Number of cells in series	50
Storage energy capacity	270 Ah
Rated energy capacity	108 kWh
Battery response time	0.1 s
Nominal BESS voltage	400 V
Cut-off voltage	300 V
Fully charged voltage	465.5949 V
Nominal discharge current	117.4 A
Nominal discharge Power	46.95 kW
Capacity at nominal voltage	244.1739 Ah
Internal resistance	0.014815 ohms

Figure B.1(a) shows the nominal current discharge Characteristic curve at 0.43478C which is 117.3913A. It shows both the nominal area and the exponential area. The BESS consists of 50 of Lithium-Ion battery cells connected in series to reach a nominal voltage rating of 400 V. Figure A.1(b) shows the current discharge curve at the rated voltage with different discharge current levels.

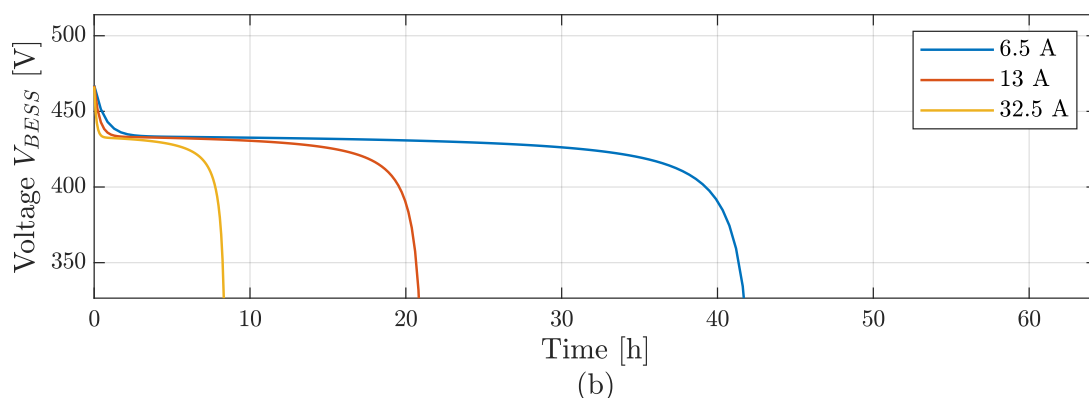
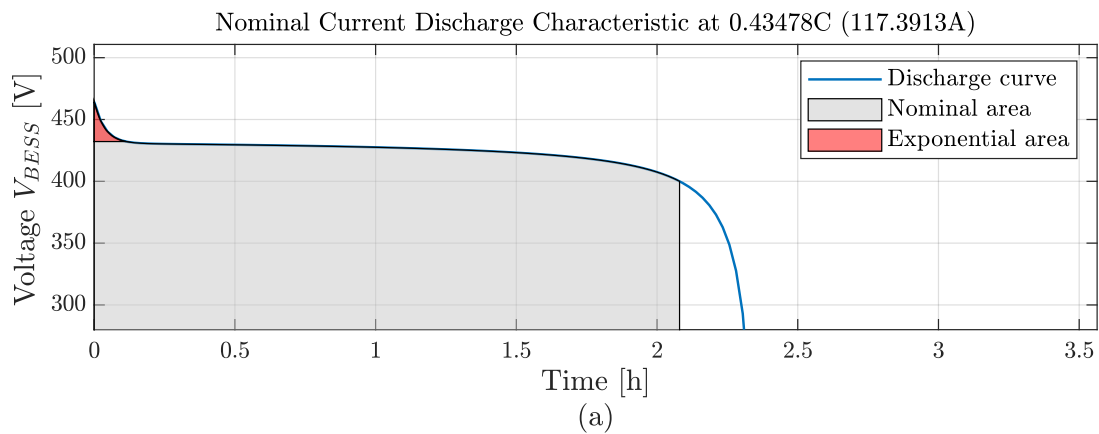


Figure B.1 (a) Nominal current discharge Characteristic curve of Lithium-Ion BESS and (b) Current discharge curve at the rated voltage with different discharge current levels

VITA

Farog Mohamed was born in Khartoum, Sudan in 1994. He earned his Bachelor of Science in Electrical and Electronics Engineering with First Class from the University of Khartoum in Khartoum, Sudan in 2016. After graduation, he worked as an electrical engineer at Salma Smart Solutions then he joined the Sudanese Electricity Distribution Company (SEDC) as a research and development engineer. In August 2018, he was awarded a graduate assistantship to pursue his master's degree in Electrical Engineering from the University of Tennessee at Chattanooga. He worked as a power electrical engineer intern at John Deere, Moline, IL during summer 2019. His research interests include power system analysis, operation, optimization and protection as well as power electronics converters for distributed energy resources integration to the smart grid. Currently, Farog is working at the ConnectSmart research group at the University of Tennessee at Chattanooga, as a research assistant. He can be reached at farogismohd@gmail.com.